UNIVERSITY OF BELGRADE

FACULTY OF ELECTRICAL ENGINEERING

Ali Ramadan Ahmed Khalf

INFLUENCE OF SURFACE PROCESSES ON THE CURRENT–VOLTAGE CHARACTERISTIC OF ORGANIC SOLAR CELLS

Doctoral Dissertation

Belgrade, 2021

УНИВЕРЗИТЕТ У БЕОГРАДУ

ЕЛЕКТРОТЕХНИЧКИ ФАКУЛТЕТ

Али Рамадан Ахмед Калф

Утицај површинских процеса на струјно-напонску карактеристику органских соларних ћелија

докторска дисертација

Београд, 2021

Предлог састава Комисије за преглед и оцену докторске дисертације (предлаже Ментор):

1. Др Јована Гојановић, доцент,
(ментор)

2. Др Петар Матавуљ, редовни професор,
(члан комисије са изабраног модула кандидата - препорука, није обавезно)

3. Др Милица Гвозденовић, редовни професор, Технолошко-металуршки факултет, Београд
(члан комисије који није у радном односу на ЕТФ-у)

4. Др Наташа Ћировић, ванредни професор,
(члан комисије са изабраног модула кандидата - препорука, није обавезно)

Title of doctoral dissertation: Influence of surface processes on the current–voltage characteristic of organic solar cells

Abstract:

Organic solar cells (OSCs) are emerging low-cost, easy production photovoltaics. Their efficiency is strongly affected by the interface physics that needs to be researched.

In this thesis, the interface physics of metal/inorganic semiconductor and metal/organic semiconductor contacts is considered. The basic structures and operation principles of OSCs are reviewed and a detailed description of the drift-diffusion model (DDM) used for modeling the OSCs is included. An extensive and detailed literature review of different physical effects that can cause the S-kink appearance in the current density-voltage (J-V) characteristics of OSCs is presented. The original research results on ITO/(poly(3,4–ethilenedioxythiophene):poly (styrenesulfonate))PEDOT:PSS/(poly(3–hexylthiophene))P3HT:(1–(3–methoxycarbonyl)propyl–1–phenyl–[6,6]–methanofullerene) PCBM/Al and ITO/PEDOT:PSS/P3HT:(indene–C60 bisadduct) ICBA/Al solar cells are presented and discussed. The influence of the surface processes on the shape of OSCs' J-V characteristics has been investigated by DDM. The surface recombination and thermal injection of charge carriers on the anode and cathode are taken into account through boundary conditions. It is deduced that there are two different types of S-shape deviations in OSCs' J-V characteristics, one arises from the reduced surface recombination velocities (SRVs), and the other is attributed to the large (>0.2eV) injection barrier height for electrons. The measured J-V characteristics of ITO/PEDOT:PSS/P3HT:PCBM/Al and ITO/PEDOT:PSS/P3HT:ICBA/Al solar cells are reproduced well by the DDM. It is anticipated that the S-shaped J-V curves of ITO/PEDOT:PSS/P3HT:ICBA/Al solar cells originate from the large electron barrier height on the cathode, rather than by the reduction of the SRVs.

Keywords: organic solar cells, drift-diffusion model, surface recombination, S-shaped J-V characteristics, injection barrier height for charge carriers

Scientific area: optoelectronics

Narrow scientific area: organic optoelectronics

Наслов докторске дисертације: утицај површинских процеса на струјно-напонску карактеристику органских соларних ћелија.

Апстракт:

Органске соларне ћелије су јефтине фотоволтаичне направе лаке производње. Њихова ефикасност јако зависи од контактне физике на електродним спојевима коју треба истражити.

У овој тези, у уводном делу, разматрана је физика на споју метала и неорганског полупроводника, као и на споју метала и органског полупроводника. Представљене су основне структуре и описан је принцип рада органских соларних ћелија (ОСЋ), а дрифт-дифузиони модел (ДДМ) који се користи за моделовање ОСЋ је детаљно размотрен. Саставни део дисертације је и опсежан преглед литературе на тему различитих физичких ефеката који могу проузроковати појаву S-девијације струјно-напонске (I-V) карактеристике ОСЋ. Спроведено је оригнално истраживање на ITO/(poly(3,4–ethilenedioxythiophene):poly (styrenesulfonate))PEDOT:PSS/(poly(3–hexylthiophene))P3HT:(1–(3–methoxycarbonyl)propyl–1–phenyl–[6,6]–methanofullerene) PCBM/Al and ITO/PEDOT:PSS/P3HT:(indene–C60 bisadduct) ICBA/Al соларним ћелијама и добијени резултати су представљени и продискутовани. Утицај површинских процеса на облик I-V карактеристике ОСЋ је испитан помоћу ДДМ. Површинска рекомбинација и термичка инјекција носилаца наелектрисања на аноди и катоди узете су у обзир кроз граничне услове. Закључено је да постоје две различите врсте S-девијације I-V криве ОСЋ. Прва врста потиче од редукованих брзина површинске рекомбинације (БПР) док се друга врста може приписати великој висини инјекционе баријере (>0,2eV) за електроне. Измерене I-V карактеристике ITO/PEDOT:PSS/P3HT:PCBM/Al и ITO/PEDOT:PSS/P3HT:ICBA/Al соларних ћелија су добро репродуковане помоћу ДДМ. Утврђено је да S-девијација I-V кривих ITO/PEDOT:PSS/P3HT:ICBA/Al соларних ћелија потиче од велике висине инјекционе баријере за електроне на катоди, а не од редукованих БПР.

Кључне речи: органске соларне ћелије, модел дрифт-дифузије, површинска рекомбинација, S-девијације струјно-напонске карактеристику, висина баријере за убризгавање носача.

Научно област: оптоелектроника.

Уже научно област: органска оптоелектроника.

First and foremost,

I am extremely grateful to my supervisors,
Dr. Jovana Gojanović (assistant professor) for
her continuous support, invaluable suggestions,
and patience during all the period of my study
especially during preparing my Ph.D. thesis.

I would like to express my full thanks to
Dr. Petar Matavulj (full professor) for his multiple
and constant help and extremely important
comments and suggestions during my study.

I would also like to extend my sincere thanks
to Dr. Nataša Ćirović (associate professor) for her
continuous and unlimited support to me in solving the
mathematical problems that I faced during my study.

My appreciation also goes out to the
ministry of higher education, the State of Libya
for their trust by presenting the financial
support of my Ph.D. scholarship.

Finally, I would like to express my gratitude
to my parents, my wife Asma, and my children
Gayda, Saraa, Manaf, and Ahmed. Without their
tremendous understanding and encouragement
in the past few years, it would be impossible
for me to complete my study.

Chapter 1

Introduction

1 Introduction

Electricity is a core resource for the development of human civilization, and it is possible to link the living standard and the electricity consumption of a society. Currently, most of the world's supply of electricity is generated from fossil fuels such as coal, oil, and natural gas. These traditional energy sources face a number of challenges, including rising prices and growing environmental concerns over the climate change risks associated with power generation using fossil fuels. Due to these challenges, governments, businesses, and consumers are increasingly supporting the development of alternative energy sources and new technologies for electricity generation. Fortunately, advances in science and technology have given us several alternative means of renewable energy production such as solar, wind, geothermal, and biomass. In the future, there will be a necessity for large-scale alternative methods of producing enormous amounts of energy needed to sustain and improve the world living standards. Currently, the average annual world's power consumption is about 13 TW. As the population increases, the future society will require increased electrical energy this figure is likely to rise to 30 TW by the year 2050. If all this energy is produced by burning fossil fuels, the level of carbon dioxide in the atmosphere will be more than twice by the current level, and greenhouse gas emissions in the next few decades will dramatically increase global warming. Hence, one of the most critical challenges for researchers is finding a way to meet the world's power requirements without rising emission of carbon dioxide into the atmosphere.

The Sun is the most important source of energy on Earth. Solar radiation is known as the electromagnetic radiation emitted by the Sun. The distribution of solar radiation (solar spectrum) as a function of the wavelength is roughly equivalent to that of the black body at a temperature of 5778 K. The emitted radiant energy from the Sun, nearly 46% lies in the infrared (IR) region (>0.7 μm), around 47% in the visible region (0.4–0.7 μm), and approximately 7% in the ultraviolet (UV) region (< 0.4 μm) [1], as shown in Fig. 1.1.

The amount of energy from sunlight that is falling on the Earth's surface in one hour is larger than the worldwide energy consumption in the entire year [2]. For this reason, researchers in the last few decades have focused on discovering more efficient and low-cost solar cells so that the world becomes fossil fuels independent. Photovoltaic (PV) technology has a number of significant advantages. Solar power is a renewable resource that is available anywhere over the world. The solar PV technologies are small and highly modular and can be used almost anywhere, unlike a lot of other electricity generation technologies. Unlike the traditional power generation using coal, oil, nuclear, and gas, solar PV has relatively low operating and maintenance (O&M) costs. PV is truly a sustainable, safe, and environmentally friendly way of producing energy.

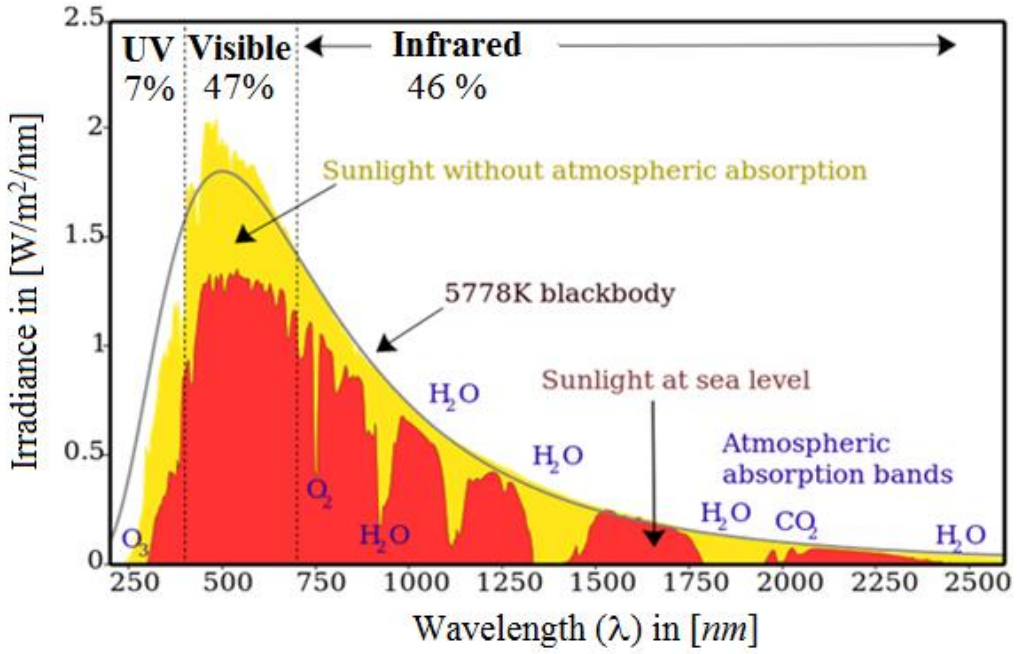

Fig. 1.1 *Solar spectrum distribution as a function of the wavelength.*

Solar power has emerged as one of the fastest-growing renewable energy sources. For solar PVs, 2017 was a milestone year, where the world added more energy from solar power than any other type of power generation technology. Further solar PVs are installed more than the fossil fuel and the nuclear power net capacity additions combined. The total global capacity of solar PVs is exceeding 400GW in 2017, as shown in the Fig. 1.2.

The different developed PV cells can be classified into four categories:

- *First-generation*: based on both technologies of monocrystalline and polycrystalline silicon, also, on gallium arsenide (GaAs);
- *Second generation*: involves solar cells based on amorphous silicon and thin films of microcrystalline silicon, cadmium telluride/cadmium sulphide (CdTe/CdS) and solar cells based on copper indium gallium selenide (CIGS);
- *Third generation*: includes technologies based on modern materials, comprising nanocrystalline films, quantum dots, a tandem of inorganic semiconductor (IS) based on III – V materials, such as GaAs / Gallium Indium Phosphide (GaInP), organic solar cells, dye-sensitized solar cells;
- *Fourth-generation*: Also called "inorganic-in-organics," it merges the low price/flexibility of polymers with the stability of inorganic nano-structures such as metal nano-particles and metal oxides or organic nano-materials such as nanotubes of carbon, graphene, and its derivatives [3].

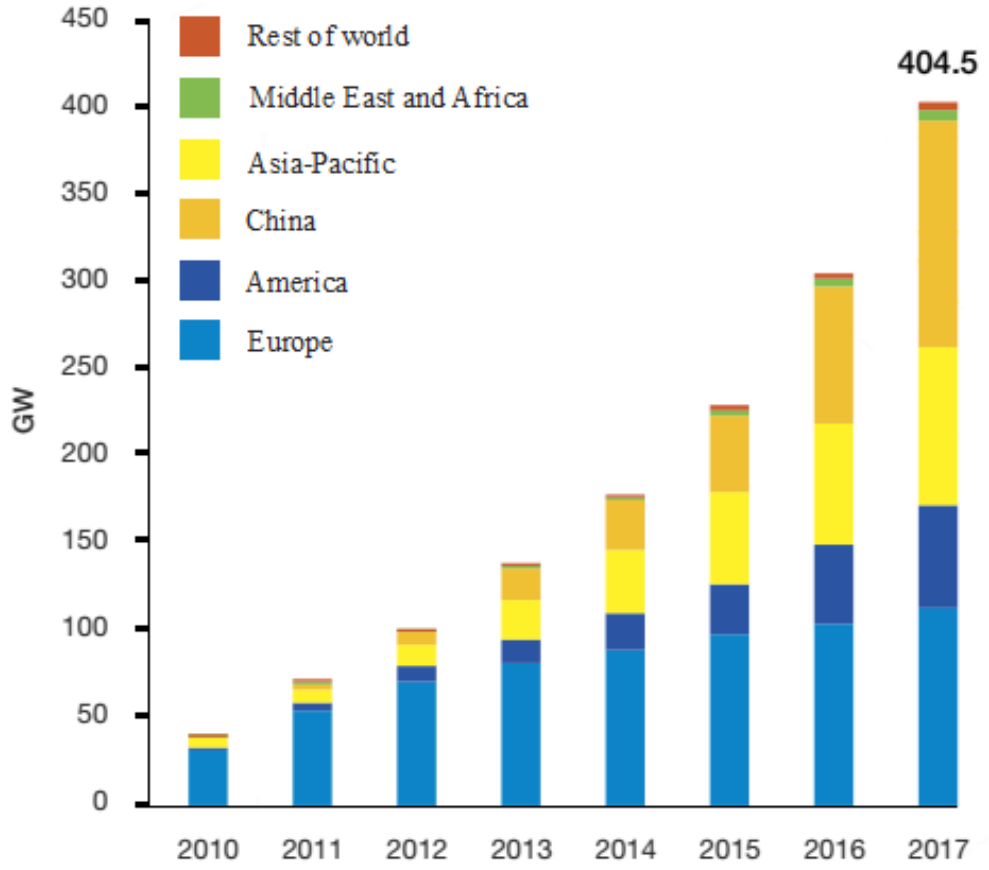

Fig. 1.2 *Evolution of global total solar PV installed capacity* 2010-2017 [4].

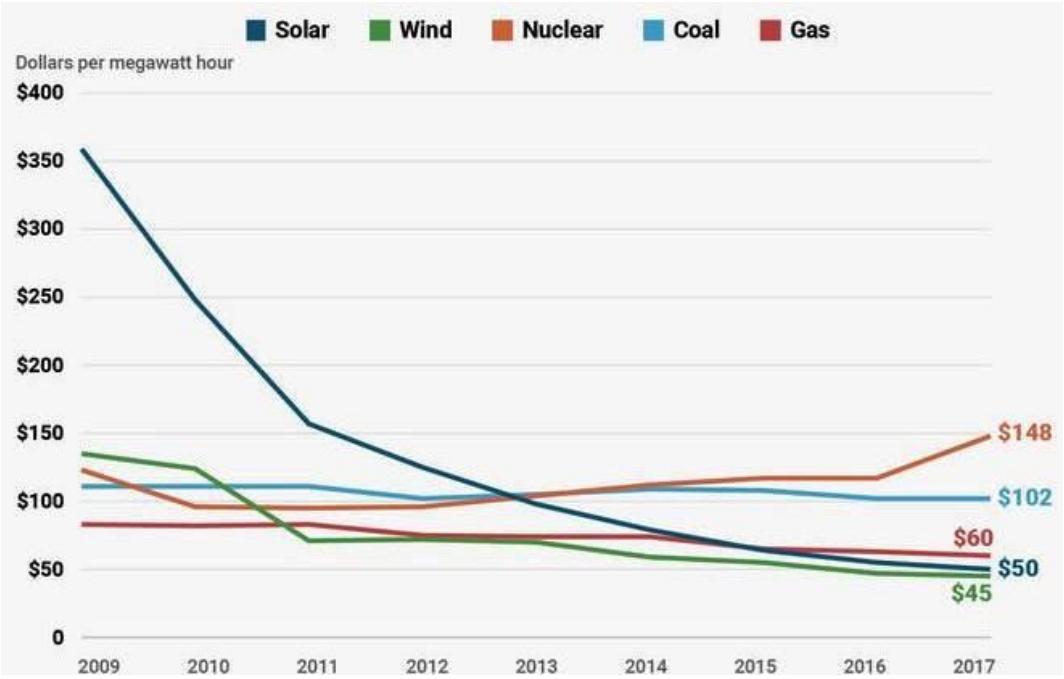

Fig. 1.3 *The average cost of energy in North America* [5].

Today solar cells produce only a very small fraction of power because more than 95% of the solar cells currently in use are made of high expensive crystalline silicon. Consequently, a lot of investigations are focused on the development technology of organic semiconductors (OS). Solar cells based on organic materials are particularly attractive and promising because they offer great technological potential to be a renewable source of electrical energy. The potential of organic photovoltaics (OPVs) resides in its low cost, not only because of the low price of the raw materials but due to the printing techniques applied for their fabrication. OPVs gained significant attention due to their promising qualities such as solution processability, tunable electronic characteristics, manufacturing at low temperatures, light-weight, and flexible materials. Whilst most of the other solar cell technologies have higher efficiencies, OPVs remain advantageous due to the low-cost material, and no environmental impact. The power conversion efficiency (*PCE*) of the organic solar cells (OSCs) devices has improved tremendously in the last decade. Nowadays, the highest *PCE* of OSCs is approaching 17.6% for single-junction [6] and exceeds 18.5% for tandem OSCs [7]. In less than two decades, organic solar cells have improved from laboratory-scale, low-efficiency devices to the first commercial products.

Among the obstacles to overcome within this technology the most important ones are the improvement of efficiency and lifetime. The limited stability (causing a short lifetime) of devices is one of the major challenges faced in the field of OPVs. Although the recent results in accelerated degradation tests have been achieved impressive stability, OSCs do not yet exceed more than a few thousand hours of lifetimes [8], limiting their scope to small-scale products rather than large-scale applications. In OSCs, there are many sources of degradation caused mostly by water and oxygen entering the cell or by reactions at the electrodes.

Most progress in the OSCs' technology is achieved by experimental investigation and primarily by improving the properties of active layers [9], [10], [11] as well as electrode interfacial layers used in OSCs [12]. As for theoretical research, the physics of organic materials is well explained, and appropriate models are established [13]. Interface physics on organic/organic and organic/metal junctions has also been studied [14]. However, inside the OSCs, it is still not clear what physical processes are governing the device performance and under which conditions. Recently, it has been shown that contact phenomena have a pronounced influence on the operation of OSCs [15], [16], [17], [18], [19], [20], [21], [22]. The future progress in OSCs' efficiency lies in the area of fundamental research, namely, determining and describing the physics underlying the OSCs' operation with great attention dedicated to contact processes. To exploit the overall potentials of organic materials it is needed to penetrate deeply into their physics.

The thesis is organized as follows. The first chapter is an introduction. In the second chapter, the physics of metal/inorganic and metal/organic semiconductor interfaces is described. Also, the surface recombination effects at the interfaces are considered. In the chapter three the OSCs' basic structures, working principles, and an overview of development and efficiency improvement are presented. The drift-diffusion model of OSCs is also given in this chapter. Chapter four reviews the experimental results and theoretical background and modeling of OSCs' S-shaped current density-voltage (J-V) characteristics. In the chapter five the surface recombination and majority carrier injection barrier height impacts on J-V curve of OSCs are analysed and discussed . The last chapter is conclusion.

Chapter 2

The Physics of Metal/Semiconductor Interfaces

2 The physics of metal/semiconductor interfaces

The interfaces are formed between metals and semiconductor solids are of utmost importance in solid-state electronic and photonic device technology. A modern microchip can consist of a million elements, but it is not useful at all unless it is possible to transmit the treated electrical signals inside it to the outside world easily. Significant efforts have been made by researchers to understand and perfect the electrical transmitting through metal/semiconductor interfaces over the past five decades. However, the physics of such contacts are not yet fully understood.

2.1 Metal/inorganic semiconductor interface

Two types of metal/inorganic semiconductor (metal/IS) junctions are commonly used in the fabrication of semiconductor devices and integrated circuits, dependent on the work function of metal (φ_M) and work function of semiconductor (φ_{sc}). The first type is formed when $\varphi_M > \varphi_{sc}$, and it is called Schottky junction. Whereas if $\varphi_M < \varphi_{sc}$, the second type is formed, and it is called ohmic junction. Good ohmic contacts are extremely important for achieving high-performance semiconductor devices. The formation of good ohmic contacts between metal and semiconductor are necessary in order to effectively extract electric current and power from a semiconductor device. In general, the ohmic contact is referred to as non-rectifying contact in which the J–V relationship under both the forward- and reverse-bias conditions is linear and symmetrical. However, in reality, a contact is considered ohmic if the voltage drop across the metal/IS interface is small compared to the voltage drop across the bulk semiconductor. The Schottky contact is a rectifying contact that can be used in a large variety of device applications. In addition, Schottky contacts can also be used to explore the physical and electrical properties of semiconductor materials and surfaces [23], [24].

Initially, in the case of connecting metal with a high work function to the *n*-type semiconductor with a lower work function ($\varphi_M > \varphi_{sc}$), the electrons are transported from the semiconductor to the metal until the equilibrium condition is established. The net leakage of electrons originates negative charge in the metal and positive charge in the semiconductor, which creates a depletion region at the semiconductor surface. Thus, the contact potential is formed to prevent further motion of the electrons from semiconductor to metal, and the potential barrier is growing for electrons to pass in opposite direction from the metal to the semiconductor, this formed contact manifests a rectifying behaviour (Schottky contact).

The equilibrium energy band structure of metal/*n*-type IS interface for $\varphi_M > \varphi_{sc}$ is illustrated in Fig. 2.1.1, (a) before contact, and (b) after contact. On the contrary, in the case of connecting the same materials for $\varphi_M < \varphi_{sc}$, an ohmic contact will be formed as showing in the Figs. (c) before contact and (d) after contact.

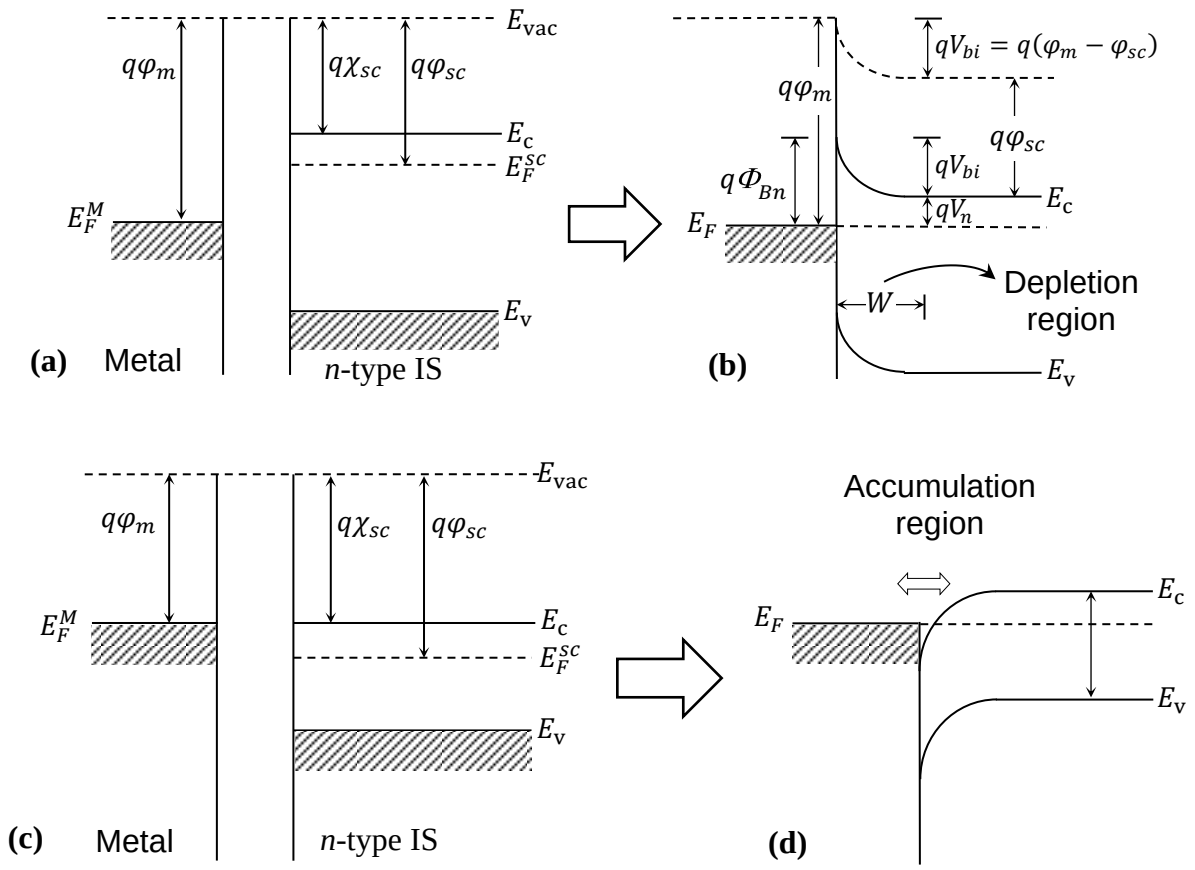

Fig. 2.1.1. *Energy band diagrams of Metal/n-type IS interface forming Schottky contact* $\varphi_M > \varphi_{sc}$, (a) *before contact*, (b) *after contact, and ohmic contact* $\varphi_M < \varphi_{sc}$, at (c) *before contact*, (d) *after contact*.

The opposite behaviour of the metal/*p*-type IS interface for $\varphi_M > \varphi_{sc}$ is shown in Fig. 2.1.2, (a) before contact, (b) after contact, while for $\varphi_M < \varphi_{sc}$, in (c) before contact, and (d) after contact.

The electron at the Femi level in the metal faces a potential barrier towards the semiconductor of Φ_{Bn}. Whereas an electron sited deeply in the semiconductor at $E = E_c$ faces a potential barrier towards the metal of V_{bi}. The barrier height of an ideal metal/*n*-type IS Schottky contact (Φ_{Bn}) is given by:

$$q\Phi_{Bn} = qV_{bi} + (E_C - E_F), \tag{2.1.1}$$

where, $qV_{bi} = q(\varphi_m - \varphi_{SC})$, and $E_C - E_F = q(\varphi_{SC} - \chi_{SC})$,

$$\Phi_{Bn} = \varphi_m - \chi_{SC}, \tag{2.1.2}$$

where q is the elementary charge, V_{bi} is the built-in voltage, E_c is the conduction band, E_F is the Fermi level, φ_m is the metal-work function, χ_{sc} is the electron affinity of semiconductor.

Similarly, from Fig. 2.1.2 (d), the barrier height for an ideal metal/*p*-type IS Schottky contact could be expressed as:

$$\Phi_{Bp} = \frac{E_g}{q}\left(\varphi_m - \chi_{SC}\right) = \frac{E_g}{q} - \Phi_{Bn}\,. \tag{2.1.3}$$

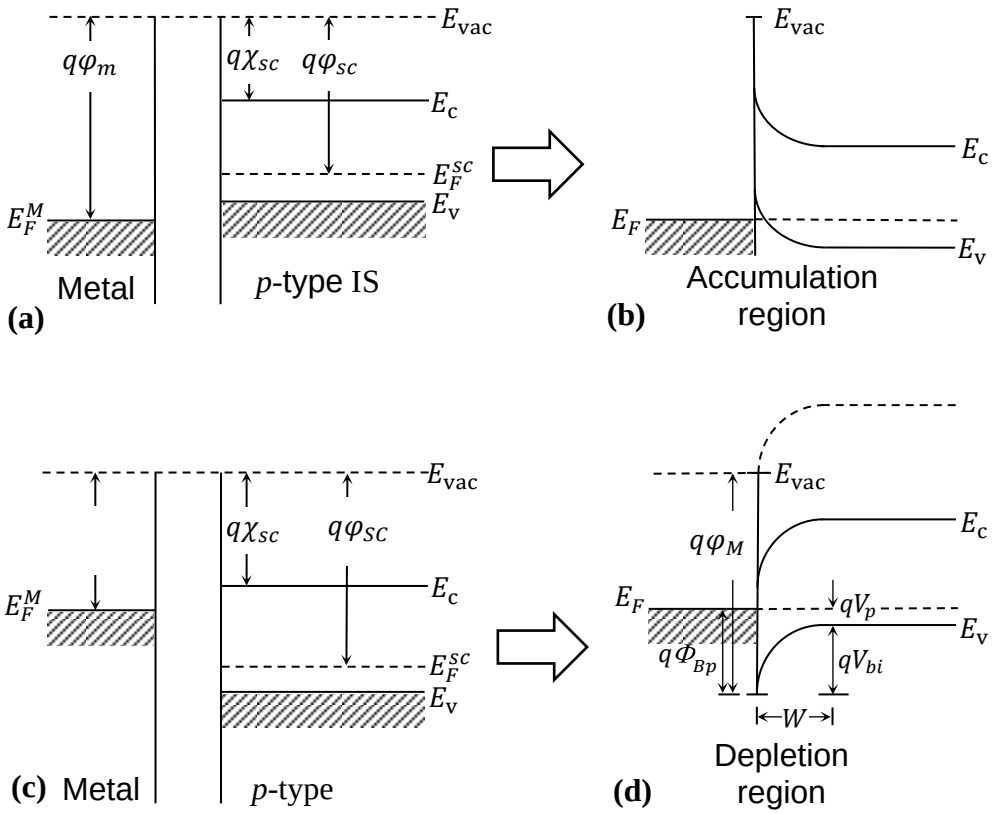

Fig. 2.1.2 *Energy band diagrams of Metal/p-type IS interface forming ohmic contact* $\varphi_M > \varphi_{sc}$, (a) *before contact*, (b) *after contact, and Schottky contact* $\varphi_M < \varphi_{sc}$, at (c) *before contact*, (d) *after contact*.

Equation 2.1.2 shows that for a given metal/IS contact, the energy gap E_g of the semiconductor is equal to the sum of barrier height for a metal on *n*-type and *p*-type IS contacts $q\left(\Phi_{Bn} + \Phi_{Bp}\right) = E_g$. The contact potential or the diffusion potential, known as the built-in potential V_{bi} is defined by:

$$V_{bi} = \varphi_m - \varphi_{SC} = \Phi_{Bn} - V_n\,, \tag{2.1.4}$$

where, V_n is the Fermi (or chemical) potential of an *n*-type IS and defined as:

$$V_n = \left(E_C - E_F\right)/q = \left(k_B T/q\right)\ln\left(N_C/N_D\right), \tag{2.1.5}$$

with N_c is the effective density of states for electrons, and N_D is the donor density (or positively charged donor ions), k_B is Boltzmann constant, and T is the absolute temperature.

Equation 2.1.4 shows that the built-in potential V_{bi} for an ideal metal/*n*-type Schottky barrier diode is equal to the difference between the metal work function and the semiconductor work function, or the difference between the Schottky barrier height and the Fermi potential of an *n*-type IS. It should be noted that in reality, the measured barrier heights for most of the metal/IS contacts do not always follow the simple predictions given by the equations 2.1.1 and 2.1.3, because of not regarding the thin insulating layer of oxide on the semiconductor surface see Fig. 2.1.3, interface states and the image force lowering effect. In fact, for most compound semiconductors, because of high surface state density and Fermi-level pinning at the interface states, the barrier height formed is found to be independent of the metals used [23], [24].

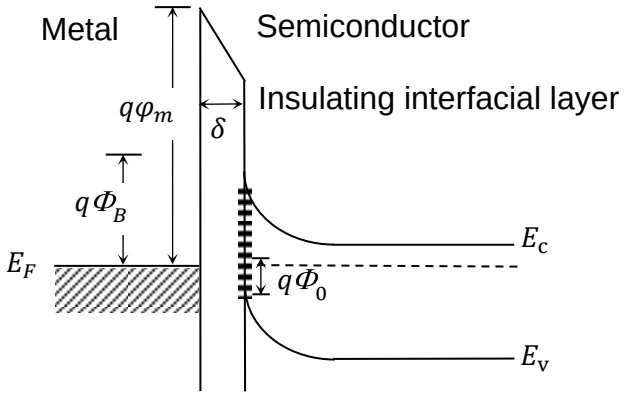

Fig. 2.1.3 *The energy band diagram of a metal/IS contact with surface states and an interfacial oxide layer of thickness* δ.

2.1.1 The current components in a Schottky contact

The energy band diagrams and current components for an ideal metal/*n*-type IS Schottky barrier diode under conditions of zero-bias, forward-bias, and reverse-bias are shown in the Fig. 2.1.4. The J_{SM} denotes the current flow from semiconductor to metal, J_{MS} is the current density from metal to semiconductor, and J_0 is the saturation current density [24].

Under zero bias the electrons are moving from the semiconductor side to the metal side due to their greater energy until the equilibrium condition is established and their potential barrier is specified as V_{bi}, while for electrons that are moving in the opposite direction the potential barrier is defined as Φ_{Bn}. If a forward-bias voltage V_a is applied to the Schottky diode, then the potential barrier on the semiconductor side of the diode is reduced to $V_{bi} - V_a$, as shown in the Fig. 2.1.4(b).

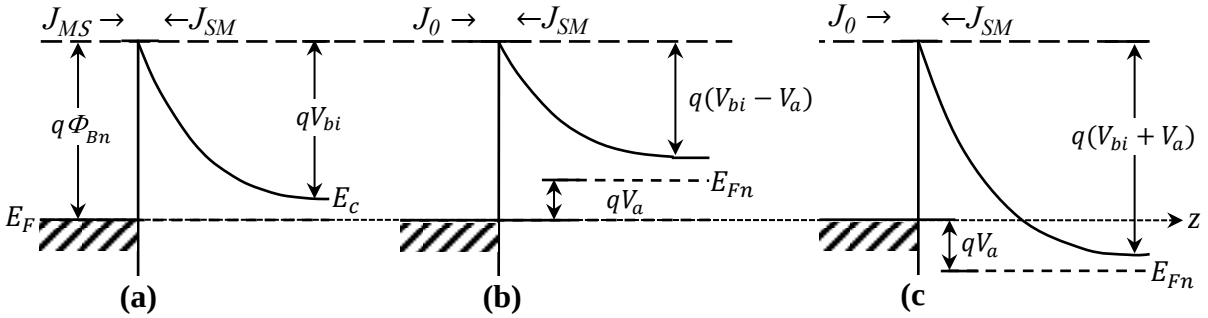

Fig. 2.1.4 *Energy band diagrams and current components for a Schottky barrier diode under* (a) *zero bias*, (b) *forward bias, and* (c) *reverse bias.*

It is observed that the barrier height Φ_{Bn} remains unaffected relatively by the applied bias voltage or the doping density of the semiconductor. Therefore, under forward-bias conditions, the current flow from the semiconductor to the metal increases significantly, while the current flow from the metal to the semiconductor maintains the same. The net current flow is dominated by the electron current from the semiconductor as shown in Fig. 2.1.4.(b).

The potential barrier on the semiconductor side increases to $V_{bi} - V_a$, under reverse-bias conditions, and the current flow from the semiconductor to the metal becomes insignificant small compared to the current flow from the metal to the semiconductor. Therefore, the thermionic emission from the metal to the semiconductor dominates as shown in Fig. 2.1.4(c). The carrier transport and current flow in a Schottky barrier diode can be analysed using the thermionic emission model.

2.1.2 The thermionic emission model

Usually, the thermionic emission refers to the emission of electrons from the surface of a hot metal (cathode), and all the emitted electrons are collected at the anode of a vacuum diode. When all the emitted electrons are extracted to the external circuit, the emitted current density is called the saturation current density J_s, and the equation that relates J_s to the cathode temperature and the work function of a metal [23], [24] is given by:

$$J_s = A_0 T^2 \exp\left(\frac{-q\varphi_m}{k_B T}\right), \tag{2.1.6}$$

where, $A_0 = 4\pi q m_0 k_B^2 / h^3$ is the Richardson constant, m_0 is the free electron mass, and h Planck constant.

The thermionic emission model for electron emission from a hot metal surface into free space can be modified for a metal-semiconductor system. The current flow from semiconductor to metal in a Schottky diode under a forward-bias condition is determined by:

$$J_{SM} = J_0 \exp\left(\frac{qV_a}{k_B T}\right), \tag{2.1.7}$$

where, J_0 is the saturation current density, and given by:

$$J_0 = A^* T^2 \exp\left(\frac{-q\Phi_{Bn}}{k_B T}\right), \tag{2.1.8}$$

with $A^* = 4\pi q m_n^* k_B^2 / h^3$ is the effective Richardson constant, and m_n^* is the electron effective mass.

The current flows in the opposite direction from metal to semiconductor J_{MS} is:

$$J_{MS} = -J_{SM} = -J_0, \tag{2.1.9}$$

hence, the total current J flows under forward-bias conditions is equal to the sum of 2.1.7 and 2.1.9, which equals

$$J = J_{SM} + J_{MS} = J_0\left(\exp\left(\frac{qV_a}{k_B T}\right) - 1\right), \tag{2.1.10}$$

the relation 2.1.10 is known as the Schottky diode equation, which estimates the current density through an exponential form dependent on both applied bias voltage and temperature. To determine the electron concentration at the vicinity of metal/IS interface, Boltzmann expression is used:

$$n(z) = N_C \exp\left(\frac{E_F - E_C(z)}{k_B T}\right), \tag{2.1.11}$$

where:

$$\delta E_C = E_C(z) - E_C(\infty), \tag{2.1.12}$$

which refers to the change of the conduction band bottom energy compared to its value very far from the junction $(z \to \infty)$. Now $n(z)$ can transform into:

$$n(z) = N_C \exp\left(\frac{\left(E_F - E_C(\infty)\right) - \delta E_C(z)}{k_B T}\right), \tag{2.1.13}$$

$$n(z) = N_C \exp\left(\frac{E_F - E_C(\infty)}{k_B T}\right)\exp\left(\frac{-\delta E_C(z)}{k_B T}\right), \tag{2.1.14}$$

$$n(0) = N_D \exp\left(\frac{-q(V_{bi} - V_a)}{k_B T}\right). \tag{2.1.15}$$

2.2 Metal/organic semiconductor interface

2.2.1 Organic semiconductors

OS are organic materials possessing semiconductor characteristics. OS molecules are bonded to each other by weak intermolecular (or inter-chain) bonds (van der Waal's force), while, atoms of OS are bonded by conjugated p-bonds. Electronic structure and optical properties are defined predominantly by a single molecule. Jablonski diagram of an OS molecule is represented in Fig. 2.2.1. The carbon and hydrogen atoms make the backbone of OS molecule and additionally they may contain some heteroatoms such as sulphur, oxygen, nitrogen and others [25].

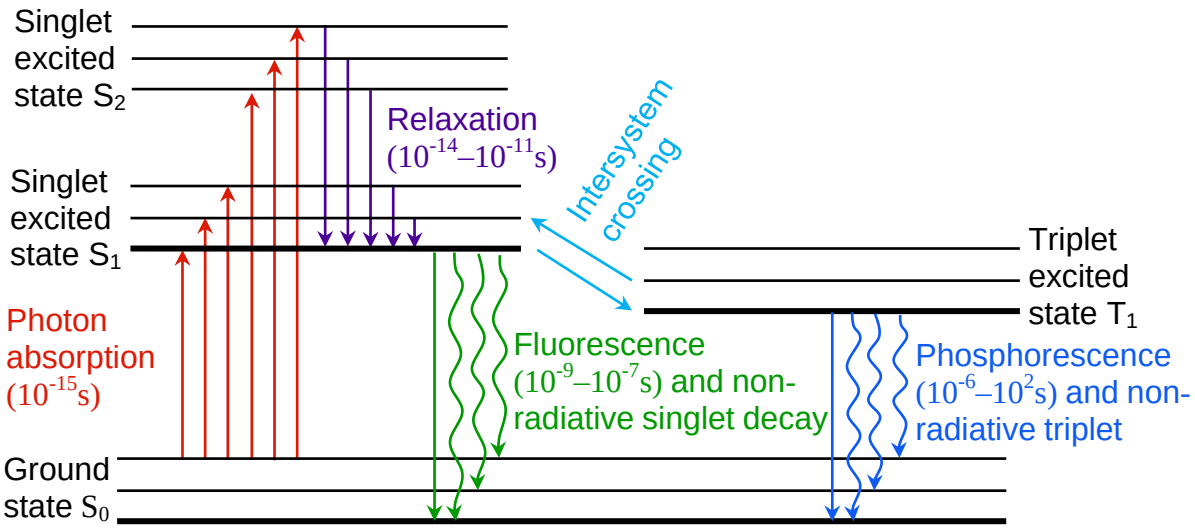

Fig. 2.2.1 *The energy level diagram of an exciton state shows the pathways of relevant excitation with their time-scales. Each level is drawn as including multiple vibronic sublevels* [25].

Electrical conductivity in OS

In order to explain electrical conductivity in OS the organic molecules of ethane, ethene and ethyne are shown in Fig.2.2.2 (a), (b), and (c), respectively. In Fig. 2.2.2 (a) the saturated organic molecule of ethane is shown. It can be seen from Fig.2.2.2 (a) that for ethane each carbon atom has all the four valence electrons used in covalent σ bonds. The ethane is for that reason an isolator. The molecules in Fig. 2.2.2(b) and (c) are unsaturated which means that they have one or more unpaired valence electrons, called π-electrons. The π-electrons may create weak π bonds between the neighbouring carbon atoms. The orbitals of neighbouring atoms are overlapped and π-electrons can be delocalized easily around atoms, resulting in electrical conductivity. Accordingly, unsaturated or conjugated organic materials behave as semiconductors. In contrast to IS, the conductivity of OS is extrinsic and arises from the injection of charges at electrodes, from intentional or unintentional doping and photogenerated electron-hole pair dissociation.

Name	Bonds	Structure
Ethane C_2H_6	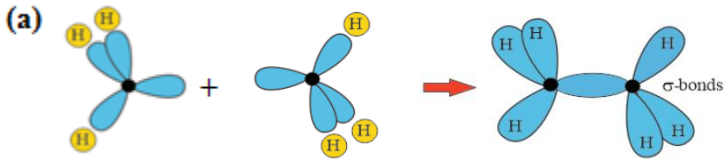 Six hydrogen atoms and two (*sp3*) hybridized carbon atoms to get ethane	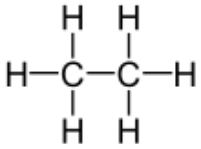
Ethene C_2H_4	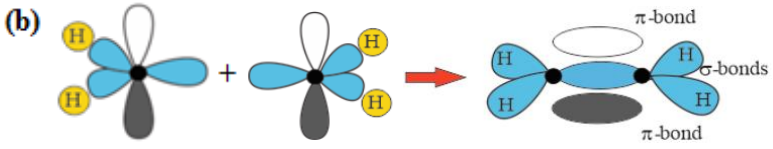 Four hydrogen atoms and two (*sp2*) hybridized carbon atoms to give ethene	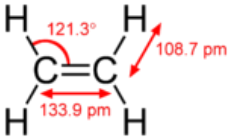
Ethyne C_2H_2	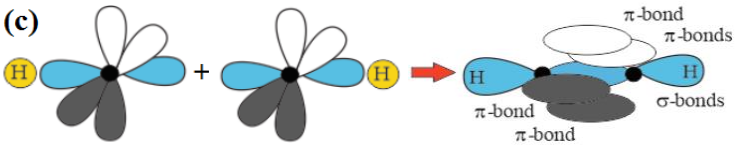 Two hydrogen atoms and two (*sp*)hybridized carbon atoms to gain ethyne	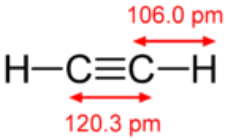

Fig. 2.2.2 *Molecular orbitals of three different organic molecules* [25].

Charge carriers in OS

When an electron or a hole is added on the conjugated molecule it will distort its surrounding environment to some degree. The distortion is coupled to the carrier and they diffuse together. This pseudo-particle is called a polaron. Therefore the polaron corresponds to the charged molecule and its accompanying polarization field (see Fig. 2.2.3). This auto-localized state reflects the strong electron-phonon interaction in OS.

Excitons in OS

Energetically much favourable state in OS is bound state of an electron and hole polaron called Frankel exciton (see Fig. 2.2.3). Polarons in Frankel exciton are attracted by Coulomb force. The excitons in OS have two important properties as compared to the IS. The first one is significant binding energy. The typical values of exciton binding energy are 0.5–1.5 electron-volt (eV) for organic crystals and 0.2–0.5eV for conjugated polymers. The second difference is the presence of well-defined spin states (singlet and triplet exciton), which in this particular respect does not differ from isolated molecules.

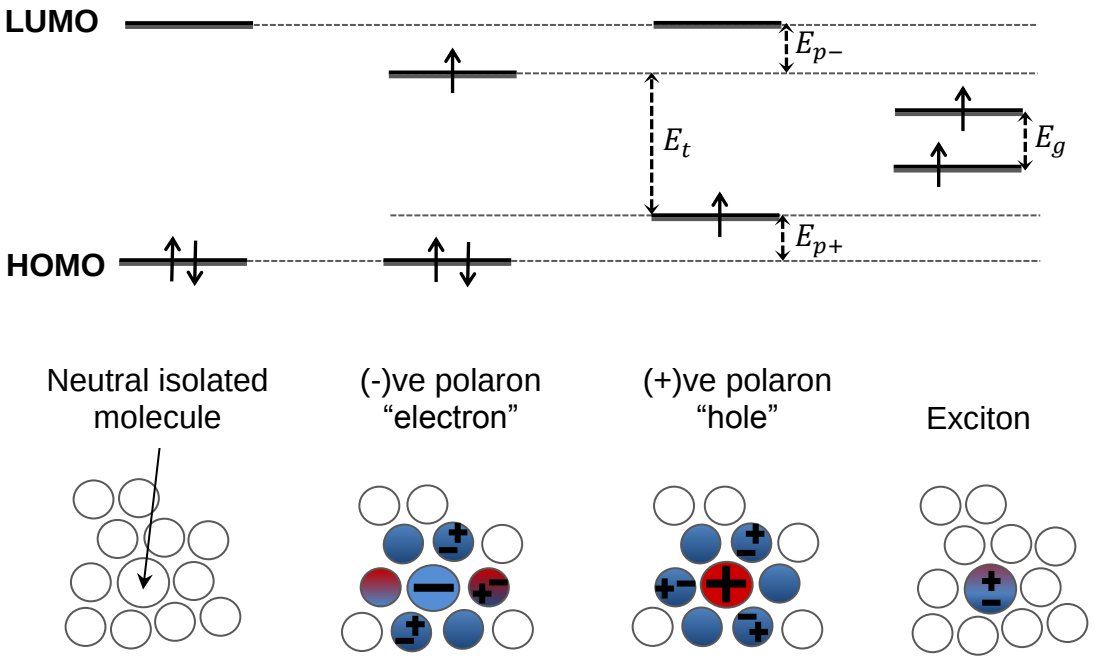

Fig. 2.2.3 *Energy diagram showing polaron and exciton states in OS.*

Transport of excitons and charge carriers

Exciton transport at the microscopic (molecular) level proceeds through consecutive energy transfer events. Three elementary types of energy transfer that are responsible for the exciton transport are cascade energy transfer, Förster transfer, and Dexter transfer. On the other hand, exciton transport is defined as a diffusion process at the mesoscopic device level.

The polarons in OS move by hopping among molecular localized sites, whose energy states are both spatially and energetically distributed. A density of states (DOS) for molecular sites must be considered in order to connect this hopping rate to mobility. The hopping rate is typically described by the Miller-Abrahams formalism [26]. The Gaussian distribution describes the energy levels of OS molecules characterized by intermolecular distances that are varying randomly. The transport is thermally activated and in general the mobility can be described by Arrhenius temperature dependence [27]:

$$\mu(T) = \mu_0 \exp\left[-(T_0/T)^2\right], \tag{2.2.1}$$

where $T_0 = 2\sigma/3k_B$, σ is the width of the DOS and μ_0 is the disorder free mobility achieved when $T \to \infty$. In principle, the hopping mobility μ_0 for electron or hole polarons is electric field dependent [28]. Usually the μ_0 obeys a so called Poole-Frenkel field dependence:

$$\mu_0 = \mu_0^* \exp\left(\gamma\sqrt{E}\right), \tag{2.2.2}$$

where $\mu_0^* = \mu_0\left(E=0\right)$, E denotes the electric field, γ is the field activation parameter, The following expression for γ usually gives a good fit to the experimental data,

$$\gamma = B\left[\frac{1}{k_B T} - \frac{1}{k_B T_0}\right], \tag{2.2.3}$$

where B is a constant characteristic of the system, and T_0 is generally much larger than room temperature. However, this implies that γ becomes negative when $T > T_0$ and the mobility decreases with increasing the electric field [27].

Recombination of charge carriers

The bimolecular recombination mechanism is the most widely observed in OS. In a chaotic OS with localized charge carriers, bimolecular recombination is limited by the rate at which oppositely charged carriers reach one another. Accordingly, the bimolecular recombination rate in OS is proportional to the mobility of charge carriers. It is described by the Langevin expression following the relation:

$$R_L = \gamma_L\left(np - n_i^2\right), \tag{2.2.4}$$

where $\gamma_L = \left(q/\varepsilon\right)\left(\mu_n + \mu_p\right)$ is the Langevin recombination coefficient, the intrinsic carrier density of electrons and holes $n_i = \sqrt{N_C N_V}\exp\left[-E_g/\left(2k_B T\right)\right]$, $\mu_{n(p)}$ are electron and (hole) mobilities, $\varepsilon = \varepsilon_0\,\varepsilon_r$, ε_0 is the permittivity of the free space and ε_r is the relative permittivity of OS material.

Two different classes of OS

It should be emphasized that there are two main categories of OS, namely, small molecular materials and polymers. Some representative materials from each category are depicted in Fig.2.2.4.

The processing techniques for preparing both types of OS are different. The small molecule OS are commonly deposited from the gas phase by sublimation or evaporation, whereas conjugated polymers are processed from solution, by spin-coating or printing techniques. The organic chemistry offers the opportunity to adapt the electrical, optical and mechanical properties of OS to different applications. The comparison between OS and IS is given in Table (2.2.1).

- **Small-molecular materials:** mainly prepared by thermal evaporation,

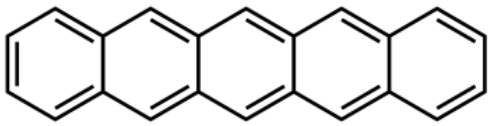

Pentacene

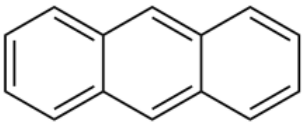

Anthracene

- **Polymers:** prepared by solution processing (spin-coating, inkjet printing),

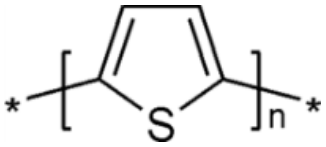

Polythiophene (P3HT)

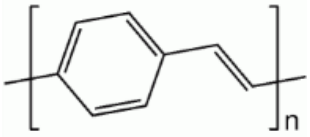

Polyphenylen-vinylene (PPV)

Fullerene (C_{60})

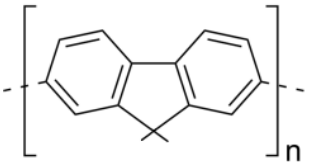

Polyfluorene (PFO)

Fig. 2.2.4 *The chemical structure of some small molecular materials and polymers.*

Table (2.2.1) A comparison between typical OS (pentacene) and IS (silicon).

Description	Organic semiconductor (**Pentacene**)	Inorganic semiconductor (**Silicon**)
Binding energy	*Weak* (*van der Waals*)	*Strong* (*covalent*)
Molecular density	2.9×10^{21} cm^{-3}	5.0×10^{22} cm^{-3}
Mechanical strength	*Weak*	*Strong*
Charge carriers	*Localized*	*Delocalized*
Conduction & valence band width	~0.1 eV	~5 eV
Charge transport mechanism	*Hopping*	*Band*
Charge carrier mobility	~1 $cm^2/(V.s)$	~1000 $cm^2/(V.s)$

2.2.2 The interface between metal and organic semiconductor

The metal/organic semiconductor interfaces are divided into two groups:

- ***Weakly interacting interfaces***:

  No new electronic states at the interface are formed due to the contact of metal and OS. It can refer to metal/OS interfaces that are not atomically clean. This is highly relevant for practical device fabrication that proceeds in moderate vacuum conditions or involving solvents.

- ***Strongly interacting interfaces***:

  The strongly interacting interface implies that a chemical reaction occurs at metal/OS interface. The chemical bonding between the metal and OS undergoes a net transfer of charge causing the vacuum level shift introduced by interface dipole, which is controlled by their chemical potentials. Currently, for this type of interface, it is difficult to model the energetics, and its energy level alignment is obtained experimentally. Hence, the integer charge transfer (ICT) model can be applied to describe the energy level alignment [29].

The weakly interacting interfaces of metals with OS have many properties in common with classic metal/IS contacts, and they are often interpreted in terms of Schottky–Mott theory Fig. 2.2.5. Strongly interacting interfaces, show some additional effects such as Fermi level pinning and screening (Fig.2.2.7) [29]. In the all cases, the Fermi energy level throughout the device is constant in equilibrium without illumination or voltage biasing. Any potential difference during interface formation is compensated by charge carriers diffusion creating an accumulation of charges or depletion region and consequently shifting the vacuum level till the Fermi level is uniform [30].

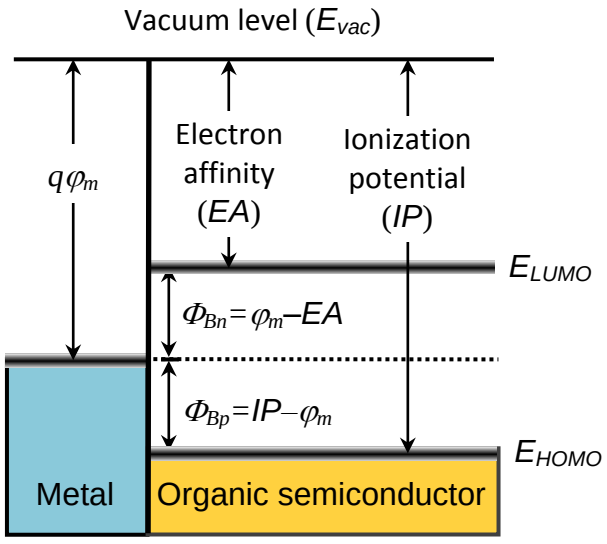

Fig. 2.2.5 *Schematic energy level diagram of the band alignment at a metal/organic interface,* (*Schottky–Mott Model*).

Weakly interacting contacts: The thermionic emission of metal/OS interface

In OS, at temperatures above $T = 0K$, the charge carriers are thermally excited over the bandgap energy E_g. The amount of thermally activated charge carriers is obtained by integration over all *E* as :

$$n = \int_{-\infty}^{\infty} D_{LUMO}(E) \cdot f_{FD}(T, E_F, E)\, dE\,, \tag{2.2.5}$$

$$p = \int_{-\infty}^{\infty} D_{HOMO}(E) \cdot \left[1 - f_{FD}(T, E_F, E)\right] dE\,, \tag{2.2.6}$$

where $D_{LUMO}(E), D_{HOMO}(E)$ are the density of state distributions of the lowest unoccupied molecular orbital (LUMO) and highest occupied molecular orbital (HOMO) levels, respectively, $f_{FD}(T, E_F, E)$ is the Femi-Dirac statistic, the Fermi energy level E_F is identical for both charge carriers electrons and holes [31].

After applying an approximations deduced from IS theory the integrals in 2.2.5 and 2.2.6 are solved and following expressions are obtained:

$$n = N_C \exp\left(\frac{E_F - E_{LUMO}}{k_B T}\right), \tag{2.2.7}$$

$$p = N_V \exp\left(\frac{E_{HOMO} - E_F}{k_B T}\right), \tag{2.2.8}$$

where N_c and N_v are here used as effective density of states.

The simplification is valid when temperature conditions: $k_B T \ll (E_F - E_{LUMO})$ and $k_B T \ll (E_{HOMO} - E_F)$ are satisfied. This usually includes room temperature. The product of electron and hole charge carrier concentrations is equal to the n_i^2 as no excess charge carriers are generated,

$$n_i^2 = np\,, \tag{2.2.9}$$

The metal electrodes are thermaly injecting the charge carriers into the OS. The properties of contacts are determined by the energy difference between the metal's Fermi energy and the HOMO and the LUMO of the OS. These offsets are indicated as to injection barriers.

Usually, for each contact, only one injection barrier is defined. For a cathode with injection barrier height for electrons (Φ_{Bn}), this is depicted in Fig. 2.2.6 (b). The concentration of injected charge carriers are given by:

$$n_{th}^{c} = N_C \exp\left(\frac{-q\Phi_{Bn}}{k_B T}\right), \tag{2.2.10}$$

$$p_{th}^{c} = N_V \exp\left(\frac{-q\left(E_g - \Phi_{Bn}\right)}{k_B T}\right). \tag{2.2.11}$$

The anode with injection barrier height for holes (Φ_{Bp}) is described similarly:

$$n_{th}^{a} = N_C \exp\left(\frac{-q\left(E_g - \Phi_{Bp}\right)}{k_B T}\right), \tag{2.2.12}$$

$$p_{th}^{a} = N_V \exp\left(\frac{-q\Phi_{Bp}}{k_B T}\right). \tag{2.2.13}$$

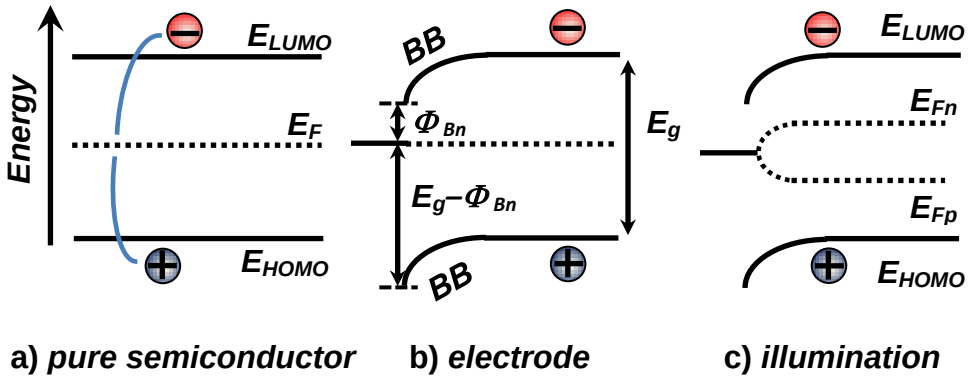

Fig. 2.2.6 *Energy structure of OS* (a) *thermally activated charge carriers of neat OS.* (b) *metal electrode (cathode) with an injection barrier* Φ_{Bn} *, electrons are injected into the semiconductor. The generated charge carrier gradients create a repulsive electric field indicated by band bending (BB).* (c) *generates excess charge carriers in the device and splits-up the quasi-Fermi levels.*

Additional charge carriers $np \gg n_i^2$ are generated in the OS, by illumination. These excess charge carriers can be incorporated in Eqns. 2.2.7 and 2.2.8, by allowing the Fermi energy to split up. Thus, two independent quasi-Fermi energies for

Electrons E_{Fn} and holes E_{Fp} are defined as:

$$n = N_C \exp\left(\frac{E_{Fn} - E_{LUMO}}{k_B T}\right), \tag{2.2.14}$$

$$p = N_V \exp\left(\frac{E_{HOMO} - E_{Fp}}{k_B T}\right), \tag{2.2.15}$$

Strongly interacting contacts

Many studies have experimentally demonstrated a strong correlation between the metal work function and the injection barrier height for holes Φ_{Bp} or the injection barrier height for electrons Φ_{Bn} at metal/OS interfaces (see Fig. 2.2.7 (a)). However, the Schottky–Mott limit is rarely reached at metal/OS interfaces [32].

The main differences to conventional semiconductors are found:

1) The presence of significant disorder implies tail states which cause the pinning of E_F to values away from the charge transport level. Such pinning of E_F is commonly observed at metal-organic contacts and is attributed either to tail states or to polaronic levels. A large number of these tail states for low energies would lead to a very low open circuit voltage (V_{OC}) in a solar cell. There is ICT model to explain the E_F pinning, which assumes polaronic or bipolaronic states at the metal-organic interface as in Fig. 2.2.7(b). As soon as the work function of the metal reaches this polaronic level, a charge transfer to the electrode is favourable and, consequently, an interface dipole is created. Generally speaking the induced density of interface states is quite sufficient to play a crucial function in the formation of the metal/OS barriers [33]. Therefore, the mechanism associated with the formation of the interface barriers is the charge transfer between the two materials due to the weak chemical interaction. This creates an electrostatic interface dipole which tends to align the metal Fermi level and the charge neutrality level (CNL) of OS. The CNL is defined as the point at which the interface states are equally donor-like and acceptor like $E_{CNL} = q\varphi_{CNL}$ [32], The CNL approach is applied to describe the metal/OS interface as shown in Fig. 2.2.7(c).

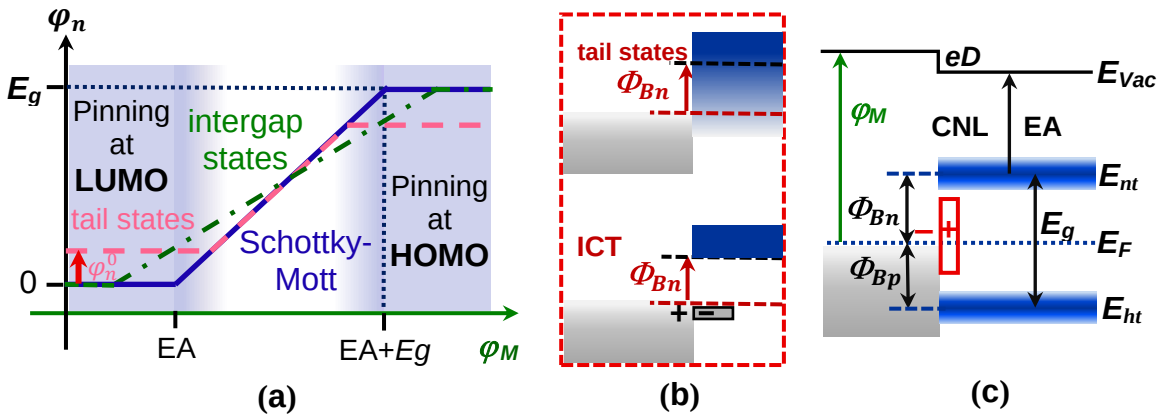

Fig. 2.2.7 *Metal/OS interfaces*: (a) Φ_{Bn} *depends on the* φ_M *, without tail states where* $EA < \varphi_M < \left(EA + E_g\right)$ *and does not exceed* E_g , (b) *the Fermi-level pinning at tail states or at the polaronic level and* (c) *an interface dipole caused by the non-filled surface states up to the* CNL [33].

The image charge screening affect the energy of electron and hole transport levels $E_{et} \approx \left(LUMO\right)$, $E_{ht} \approx \left(HOMO\right)$ in OS in the vicinity of the metal/OS interface. The valence and conduction band states approach each other near the metal [33]. The transport energy gap is reduced near the metal as schematically depicted in Fig. 2.2.8. Thus, there is an unconventional band bending near interfaces between the OS and the metal due to the much higher screening ability of the metal than of the OS. Finally, the image charge screening is substantially larger in OS as compared to IS materials. Firstly, this is a consequence of the low dielectric constant of OS materials which are in the range of $\varepsilon_r \sim 3$, while for IS materials $\varepsilon_r > 10$, and secondly due to the more confined wave function of the molecular electronic states of OS in comparison to the band-like states in IS [34].

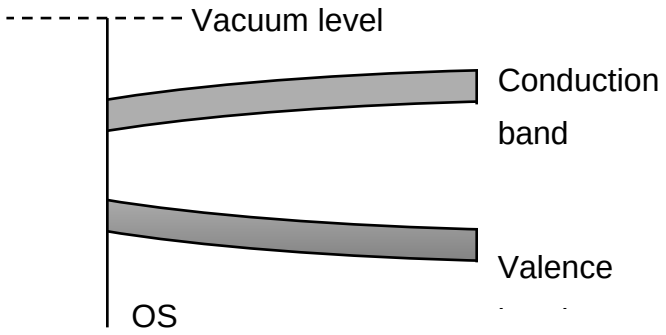

Fig. 2.2.8 *The valence and conduction band states approach each other near a metal/semiconductor interface as a result of the image charge potential.*

2.3 Surface recombination of charge carriers

The main types of charge carrier recombination are band-to-band recombination (radiative, and non-radiative), trap-assisted recombination namely Shockley–Read–Hall (SRH) recombination, Auger recombination, and surface recombination. As an introduction to the topic of surface recombination a short review of other (bulk) recombination mechanisms is given.

Band-to-band recombination

It is known as direct thermal recombination. In this process the electrons spontaneously decaying from the conduction band to the valence band. This process is usually radiative [35]. The expressions for recombination velocities are different for the low and high excitations as [36]:

$$R = -\frac{dn}{dt} = \frac{\Delta n_0}{\tau} e^{-\frac{t}{\tau}} \qquad (\textit{Low excitation}), \qquad (2.3.1)$$

$$R = -\frac{dn}{dt} = \frac{-B}{\left(Bt + \Delta n_0^{-1}\right)^2} \qquad (\textit{High excitation}), \qquad (2.3.2)$$

where τ is the carrier lifetime, $\Delta n_0 = \Delta n\left(t = 0\right)$, Δn is the excess electron concentration, and B is a constant called bimolecular recombination coefficient. It has typical values of $10^{-11} - 10^{-9}\, cm^3/s$ for direct-gap semiconductors. In OS direct recombination mechanism of charge carriers is Langevin type bimolecular recombination which was already mentioned in the section 2.1 [33].

Shockley–Read–Hall recombination

It is called trap-assisted recombination because the transition of electron from conduction to valence band is taking place through localized energy state created within the bandgap by a dopant or a defect in semiconductor (trap). The energy is released in the form of lattice vibration, a phonon. The SRH recombination is the significant process in silicon and other indirect bandgap materials. However, trap-assisted recombination can also take place in direct bandgap materials under conditions of very low carrier densities or in materials with a high density of traps such as Perovskites. [37]. The recombination velocity for this type of recombination is defined as:

$$R_{SRH} = C_n C_p N_t \frac{n\,p - n_i^2}{C_n\left(n + n_1\right) + C_p\left(p + p_1\right)}, \qquad (2.3.3)$$

where $C_{n(p)}$ are the capture coefficients of electrons (holes), N_t is the density of electron traps, n is the electron density in the conduction band, p is hole density in the valance band, here, both n_1, p_1 depend on the energetic position of the trap state expressed by fraction *u* of the E_g as: [33], [38]

$$n_1 = N_C \exp\left(\frac{-\left(1-u\right)E_g}{k_B T}\right), \text{ and } \; p_1 = N_V \exp\left(\frac{-u\,E_g}{k_B T}\right), \qquad (2.3.4)$$

where $u \in \left(0,...,1\right)$.

Auger recombination

In Auger recombination, the energy released by recombination of a free electron and hole is transferred to a third carrier which is excited to a higher energy level without moving to another energy band. After the interaction, the third carrier normally loses its excess energy which is spent on thermal vibrations. This process is a three-particle interaction, and it is significant in non-equilibrium conditions with very high carrier density. The recombination velocity is given as [35]:

$$R = C_n n^2 p, \tag{2.3.5}$$

and

$$R = C_p n p^2, \tag{2.3.6}$$

where, $C_{n(p)}$ are the Auger capture probabilities for electrons (holes).

Surface recombination

Besides the recombination processes in the bulk of semiconductor, in electronic and optoelectronic devices there are additional recombination losses that occur at the contact surfaces of semiconductor and metal electrode. The recombination at the metal/semiconductor interface needs to be treated separately. In semiconductor devices, the surface recombination-generation (R-G) is important as much as the bulk R-G at certain conditions. The surface R-G is an annihilation/creation of carriers near the vicinity of the semiconductor surface through the interaction with interfacial traps. The surface states or interfacial traps are equivalent to R-G centers localized at the material surface. Typically, interface traps are found to be distributed continuously in energy throughout the bandgap of the semiconductor. In the semiconductor, the same fundamental processes that occur in the bulk also occur at the surface. Electrons and holes can be captured at the surface centers or emitted from the surface centers as shown in Fig. 2.3.1. This relates to the interaction between conductive and valence band states with surface trap states.

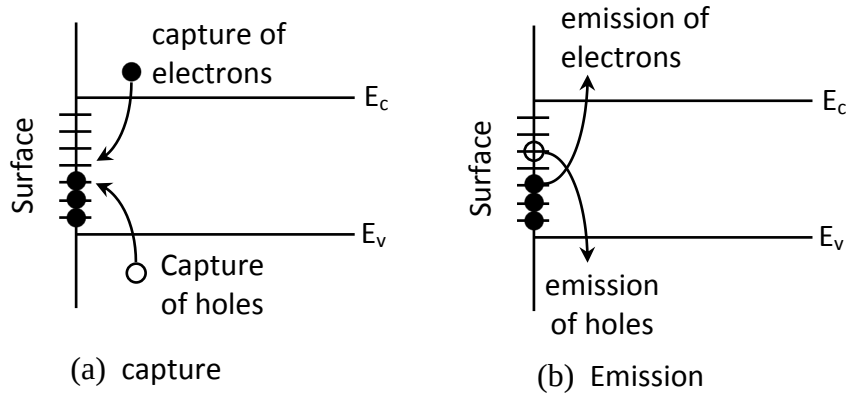

Fig. 2.3.1 *At the semiconductor surface, electrons and holes can be* (a) *captured leading to recombination,* (b) *emitted leading to generation* [35].

From the energy band description, additional transitions are expected to occur between surface centers at different energies. However, considering interfacial-trap densities, these apparently inter-center transitions are extremely improbable because of the diffused or spatially isolated nature of the centers on the surface plane (see Fig. 2.3.2).

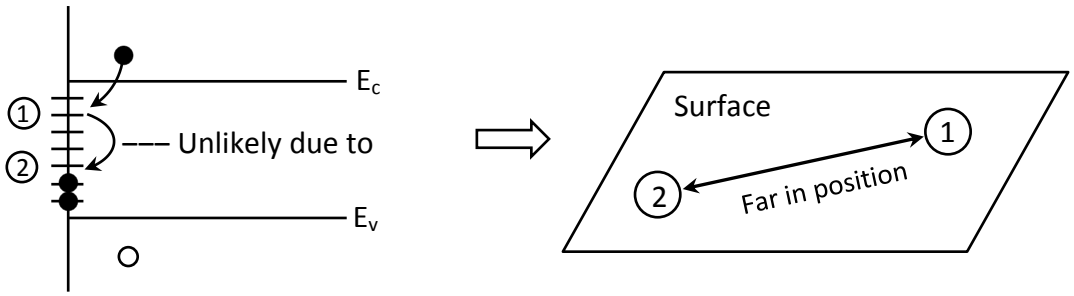

Fig. 2.3.2 *Illustration of surface inter-center transitions and surface trap spatial position* [35].

The very notable physical similarity between the surface and trap assisted bulk recombination leads to a parallel mathematical description of the processes. This allows establishing a number of relationships by direct inference from the corresponding bulk result. Nevertheless, there are two essential differences:

- It is logical to describe the net recombination rates in terms of carriers removed from a given band per unit area because the surface states are organized in a plane rather spread out over a volume.
- Usually, a single level dominates bulk R-G, the surface R-G includes centers distributed in energy throughout the bandgap as it was already mentioned. Therefore, the single-level surface rates must be integrated over all energies in the bandgap.

It is appropriate initially to determine the net recombination rates for interface traps that belong to a single energy level, and then modify the results taking into account the distributed nature of the states. So, to start the analysis, it is assumed that, the bandgap contains a single energy level. By analogy to bulk R-G, the surface R-G relationships for single level are:

$$r_{\mathrm{Ns}} = c_{\mathrm{ns}}\, p_{\mathrm{Ts}}\, n_s - e_{\mathrm{ns}}\, n_{\mathrm{Ts}}, \tag{2.3.7}$$

$$r_{\mathrm{Ps}} = c_{\mathrm{ps}}\, n_{\mathrm{Ts}}\, p_s - e_{\mathrm{ps}}\, p_{\mathrm{Ts}}, \tag{2.3.8}$$

where $r_{\mathrm{Ns}}, r_{\mathrm{Ps}}$ are the net electron and hole recombination rate at the surface centers, $c_{\mathrm{ns}}, c_{\mathrm{ps}}$ are the surface electron and hole capture coefficients in [cm^3/sec], p_{Ts} is the number of empty surface centers per cm^2 at energy E_{IT}, n_{Ts} is the number of filled surface centers per cm^2 at energy E_{IT}, n_s, p_s are the surface concentrations of electrons and holes in [cm^{-3}], e_{ns} and e_{ps} are the surface electron and hole emission coefficients in [1/sec].

Applying detailed balance [35]:

$$e_{\mathrm{ns}} = c_{\mathrm{ns}}\, n_{1\mathrm{s}}\,, \tag{2.3.9}$$

$$e_{\mathrm{ps}} = c_{\mathrm{ps}}\, p_{1\mathrm{s}}\,, \tag{2.3.10}$$

the $r_{\mathrm{Ns}}, r_{\mathrm{Ps}}$ are obtained as:

$$r_{\mathrm{Ns}} = c_{\mathrm{ns}}\left(p_{\mathrm{Ts}}\, n_s - n_{\mathrm{Ts}} n_{1\mathrm{s}}\right), \tag{2.3.11}$$

$$r_{\mathrm{Ps}} = c_{\mathrm{ps}}\left(n_{\mathrm{Ts}}\, p_s - p_{\mathrm{Ts}} p_{1\mathrm{s}}\right), \tag{2.3.12}$$

where $n_{1\mathrm{s}}$ and $p_{1\mathrm{s}}$ are defined as:

$$n_{1\mathrm{s}} = n_i \exp\left[\left(E_{IT} - E_i\right)/k_B T\right], \tag{2.3.13}$$

$$p_{1\mathrm{s}} = n_i \exp\left[\left(E_i - E_{IT}\right)/k_B T\right], \tag{2.3.14}$$

The degeneracy factor of surface center in equations 2.3.9 and 2.3.10 is taken to be unity.

By invoke the steady-state condition under which:

$$r_{\mathrm{Ns}} = r_{\mathrm{Ps}} \equiv R_s. \tag{2.3.15}$$

By solving the system of equations 2.3.11, 2.3.12, yields:

$$n_{\mathrm{Ts}} = \frac{c_{\mathrm{ns}}\, N_{\mathrm{Ts}}\, n_{\mathrm{s}} + c_{\mathrm{ps}}\, N_{\mathrm{Ts}}\, p_{1\mathrm{s}}}{c_{\mathrm{ns}}\left(n_{\mathrm{s}} + n_{1\mathrm{s}}\right) + c_{\mathrm{ps}}\left(p_{\mathrm{s}} + p_{1\mathrm{s}}\right)}, \tag{2.3.16}$$

where, N_{Ts} is the total number of surface states/cm^2; $N_{\mathrm{Ts}} = n_{\mathrm{Ts}} + p_{\mathrm{Ts}}$.

Furthermore, by substituting equation 2.3.16 and the same result for p_{Ts}, into equation 2.3.11 yields:

$$R_S = \frac{n_{\mathrm{s}} p_{\mathrm{s}} - n_i^2}{\left(\dfrac{1}{N_{\mathrm{Ts}}\, c_{\mathrm{ps}}}\right)(n_{\mathrm{s}} + n_{1\mathrm{s}}) + \left(\dfrac{1}{N_{\mathrm{Ts}}\, c_{\mathrm{ns}}}\right)(p_{\mathrm{s}} + p_{1\mathrm{s}})}, \tag{2.3.17}$$

where the both terms $N_{\mathrm{Ts}}\, c_{\mathrm{ns}} = s_n$ and $N_{\mathrm{Ts}}\, c_{\mathrm{ps}} = s_p$ have units of velocity, and they are the single-level surface recombination velocities (SRVs) of electrons and holes respectively.

Typically the surface centers are found to be distributed continuously in energy throughout the bandgap of the semiconductor. The net recombination rates associated to the individual centers in the distribution should be summed together in order to get the overall net recombination rate. A simple addition of rates is possible due to non-interacting centers at different energies. The task now is to change the single-level result appropriately to achieve the net recombination rate connected with a continuous distribution of non-interacting surface centers.

$$dR_s = \left(\frac{n_s p_s - n_i^2}{\left(\frac{n_s + n_{1s}}{c_{ps}} \right) + \left(\frac{p_s + p_{1s}}{c_{ns}} \right)} \right) D_{IT}(E) dE \,, \tag{2.3.18}$$

where $D_{IT}(E)$ is the interfacial traps density at energy E between E_C and E_V, and $D_{IT}(E)dE = N_{Ts}$ is the number of interfacial traps per cm^2 with energies between E and $E + dE$.

Then integration of 2.3.18 over all bandgap energies yields:

$$R_s = \int_{E_V}^{E_C} \left(\frac{n_s p_s - n_i^2}{\left(\frac{n_s + n_{1s}}{c_{ps}} \right) + \left(\frac{p_s + p_{1s}}{c_{ns}} \right)} \right) D_{IT}(E) dE \,, \tag{2.3.19}$$

It should be mentioned that, all the trap parameters in the last equation can vary with energy.

To conclude the surface R-G section a special case should be considered when having a low level injection and therefore flat energy bands at the interface.

The case assumptions are:

- the semiconductor is *n*-type,
- the energy band are flat at the surface $n_{s0} = N_D$,
- low level injection conditions prevail $\Delta n_s = \Delta p_s \le n_{s0}$.

By introducing the $n_s = n_{s0} + \Delta p_s$, $p_s = p_{s0} + \Delta p_s$, and under the stated conditions:

$$n_s p_s - n_i^2 \simeq n_{s0} \Delta p_s \,, \tag{2.3.20}$$

and,

$$\left(n_s + n_{1s}\right)/c_{ps} + \left(p_s + p_{1s}\right)/c_{ns} \simeq \left(n_{s0} + n_{1s}\right)/c_{ps} + p_{1s}/c_{ns} \,. \tag{2.3.21}$$

Now equation (2.3.21) becomes:

$$R_s \simeq \left(\int_{E_V}^{E_C} \frac{c_{\mathrm{ps}} D_{IT}}{1 + \frac{n_{1\mathrm{s}}}{n_{\mathrm{s0}}} + \frac{c_{\mathrm{ps}}}{c_{\mathrm{ns}}} \frac{p_{1\mathrm{s}}}{n_{\mathrm{s0}}}} dE \right) \Delta p_s , \tag{2.3.22}$$

and for *n*-type material R_s can be written as,

$$R_s = S_p \, \Delta p_s , \tag{2.3.23}$$

where S_p is SRV of holes:

$$S_p = \int_{E_V}^{E_C} \left(\frac{c_{\mathrm{ps}} D_{IT}}{1 + \frac{n_{1\mathrm{s}}}{n_{\mathrm{s0}}} + \frac{c_{\mathrm{ps}}}{c_{\mathrm{ns}}} \frac{p_{1\mathrm{s}}}{n_{\mathrm{s0}}}} \right) dE \quad . \tag{2.3.24}$$

Similarly, for *p*-type material,

$$R_s = S_n \, \Delta n_s , \tag{2.3.25}$$

where S_n is SRV of electrons:

$$S_n = \int_{E_V}^{E_C} \left(\frac{c_{\mathrm{ns}} D_{IT}}{1 + \frac{p_{1\mathrm{s}}}{p_{\mathrm{s0}}} + \frac{c_{\mathrm{ns}}}{c_{\mathrm{ps}}} \frac{n_{1\mathrm{s}}}{p_{\mathrm{s0}}}} \right) dE \quad , \tag{2.3.26}$$

Generally speaking under arbitrary conditions the hole and electron SRVs can be defined as:

$$S_p = \frac{R_s}{\Delta p_s} = \frac{\int_{E_V}^{E_C} \left(\frac{n_{\mathrm{s}} p_{\mathrm{s}} - n_i^2}{\left(\frac{n_{\mathrm{s}} + n_{1\mathrm{s}}}{c_{\mathrm{ps}}} \right) + \left(\frac{p_{\mathrm{s}} + p_{1\mathrm{s}}}{c_{\mathrm{ns}}} \right)} \right) D_{IT}(E) dE}{\Delta p_s} , \tag{2.3.27}$$

and

$$S_n = \frac{R_s}{\Delta n_s} = \frac{\int_{E_V}^{E_C} \left(\frac{n_{\mathrm{s}} p_{\mathrm{s}} - n_i^2}{\left(\frac{n_{\mathrm{s}} + n_{1\mathrm{s}}}{c_{\mathrm{ps}}} \right) + \left(\frac{p_{\mathrm{s}} + p_{1\mathrm{s}}}{c_{\mathrm{ns}}} \right)} \right) D_{IT}(E) dE}{\Delta n_s} , \tag{2.3.28}$$

It has to bear in mind that in this case, the SRVs are dependent on the injection level, the amount of the band bending, and possibly of the perturbed carrier concentrations [36].

According to Sandberg [15], [18] and Wagenpfahl [39], [22] it is essential to permit recombination between electrons and holes located on both sides of the interface, because it makes physically important current path in the case when energy barriers are formed on the semiconductor/metal interface. The electrons in their density-of-states facing a barrier at an interface do not need to cross it to recombine with holes on the other side of the interface they can recombine directly through the interface, e.g. through trap states which are always present at semiconductor heterojunctions (Fig. 2.3.3). Those trap states are predominantly the consequence of the sudden discontinuation of the semiconductor or by defects and impurities at the junction.

The model used to account for surface recombination in electronic and optoelectronic device physics is typically as follows. The surface recombination is characterized by the electron and (hole) SRVs, as it was already introduced in previous considerations, and leads to surface recombination currents of electrons $J_{SR,n}$ and holes $J_{SR,p}$ given by:

$$J_{SR,n} = q S_n \left(n_s - n_{th} \right), \tag{2.3.29a}$$

$$J_{SR,p} = q S_p \left(p_s - p_{th} \right), \tag{2.3.29b}$$

where n_{th}, p_{th} are the thermal electron and hole concentrations respectively.

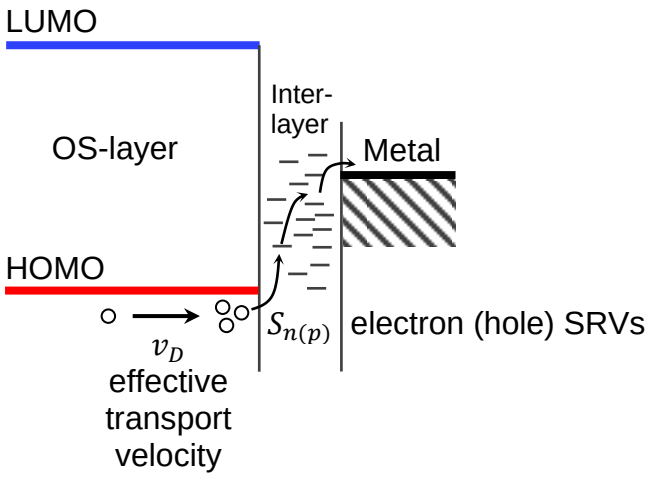

Fig. 2.3.3 *Schematic picture of the surface recombination at a semiconductor-electrode contact for holes being collected at a metal electrode*

The surface recombination may be extremely important mechanism of recombination because it affects the extraction and injection of free carriers at the semiconductor/metal surface. The schematic preview of the impact of surface recombination on these processes is given in Fig. 2.3.3. It is important to compare the velocity at which the free carriers are coming to, or moving away from the interface with the corresponding SRV (for those carriers). If the SRV is smaller than the average carrier velocity space charges are formed through accumulation or depletion [18], [38], [39].

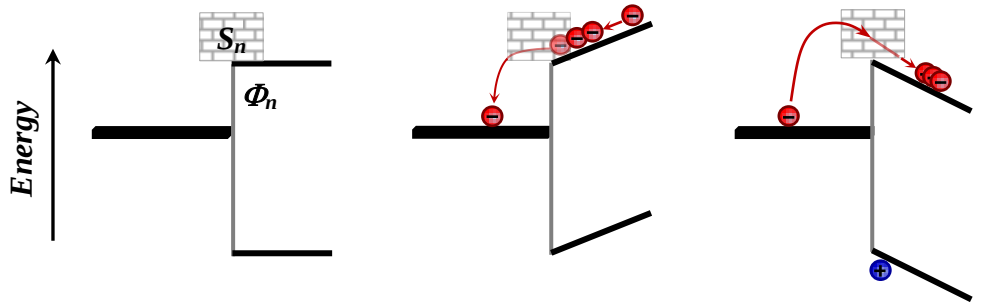

a) flat bands b) extraction c) injection

Fig. 2.3.4 *Space charge accumulation in metal/OS interface.*
(a) *No potential well or space charge can be created.*
(b) *Creation of a space charge accumulation* [39].

The space charge accumulation and depletion at the interface of metal and OS are illustrated in Fig. 2.3.4. Fig. 2.3.4. (a) shows the difference (Φ_n) between the E_F of metal and the LUMO level of semiconductor. There is no potential well or space charge accumulated due to the constant work function of the metal. In Fig.2.3.4. (b) the electron transport through the interface is limited due to the finite value of electron SRV (S_n). A space charge created when the electrons are transported towards the interface faster than those are extracted. And in Fig. (c) The injected amount of charge carriers is reduced by finite SRVs which create a local zone of charge carrier (depletion region) at the interface.

When modelling solar cells and photodetectors, equations 2.3.29 (a) and (b) are used as the boundary conditions at the anode and cathode interfaces.

For anode:

$$J^a_{SR,n} = q\,S^a_n\left(n^a_s - n^a_{th}\right), \tag{2.3.30a}$$

$$J^a_{SR,p} = q\,S^a_p\left(p^a_s - p^a_{th}\right). \tag{2.3.30b}$$

For cathode:

$$J^c_{SR,n} = q\,S^c_n\left(n^c_s - n^c_{th}\right), \tag{2.3.31a}$$

$$J^c_{SR,p} = q\,S^c_p\left(p^c_s - p^c_{th}\right), \tag{2.3.31b}$$

where $S^a_{n(p)}, S^c_{n(p)}$ are the SRVs for electrons (holes) at anode and cathode, $n^{a(c)}_{th}$, and $p^{a(c)}_{th}$ are the thermal electron and hole concentrations respectively at anode (cathode).

It is quite strange that all SRVs $\left(S_n^a, S_p^a, S_n^c, \text{and } S_p^c\right)$ are always considered to be constants in all calculation models. This section will finish by reconsidering these questions:

(**Q1**) What about the carriers that are moving from semiconductor to metal?

(**Q2**) Why SRVs are considered constants while they are dependent on energy band bending and space charge?

(**Q3**) Are all the carriers contributed to the current?

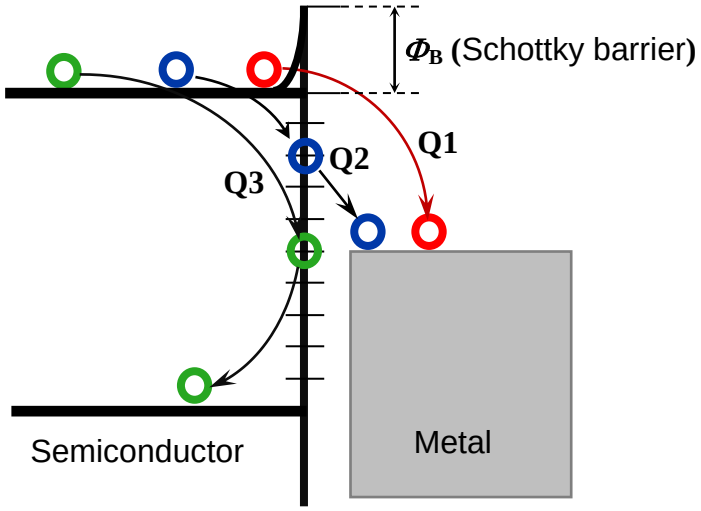

Fig. (2.3.5)

Chapter 3

Organic Solar Cells

3 Organic solar cells

3.1.1 Brief history of organic photovoltaics

The PV effect discovery is commonly ascribed to 1839 when Becquerel observed the photoelectrochemical process [40]. The first report on photoconductivity was introduced by Smith in 1873 and Adams in 1876, working on selenium [41]. The first solar cell was developed at Bell Laboratories in 1954 [42]. Over the years of development, the efficiency has exceeded 26% for crystalline Si solar cells [43]. Currently, the most common type of PVs used are Si-based solar cells which account of 95% of all PVs.

Pochettino in 1906 [44] and Volmer in 1913 [45] for the first time observed the photoconductivity in organic compound known as anthracene. The prospective use of organic materials in electronics and optoelectronics has been recognized in the late 1950s. Significant commercial potential, led to increased research in the field of photoconductivity and related topics. The PV effect was observed also in many biological molecules such as chlorophylls, carotenes, and other porphyrins, as well as the structurally related phthalocyanines [46].

During 1970 to 1980 much work has been done on realising and developing OSCs. However, very low efficiencies were achieved because of the low concentration and mobility of free charge carriers. In the first ten years of the current century, a new and strong interest in the OS has appeared motivated by two developments. The first one is the very high and fast quantum efficiency of the electron transfer from an excited polymer to fullerene (C_{60}) [47], [48], and the second one is the development of efficient displays based on organic light-emitting devices using low-cost technology. Organic solar cells have not yet entered the market compared to inorganic solar cells despite many improvements over the last years.

3.1.2 Device configurations

Besides the properties of conjugated materials which are important to achieve high-performance solar cells, the device structure can have a dramatic effect on the efficiency of harvesting sunlight. In fact, due to the creative design of the device architecture, several advances happened. For example, the efficiency increased dramatically from about 0.01% [49] in 1974 to more than 1 % [50] in 1979 when the system structure changed from a sandwich configuration with a single light absorber between two electrodes to a bilayer donor/acceptor organic heterojunction between electrodes. Additionally, solar cell efficiency exceeded 10% when a bulk heterojunction structure (BHJ) is formed by mixing donor and acceptor materials [51] and further by stacking devices to achieve a tandem structure. BHJ is homogeneous blend of two organic materials. Usually an organic dye or a semiconducting polymer, is used as electron donor and fullerene is commonly used for electron acceptor.

An OSCs' architecture consists of a photoactive layer, sandwiched between two electrodes. At least one of those electrodes should be transparent. Typically it is made of indium tin oxide (ITO) evaporated or sputtered on a transparent material such as glass or polyethylene terephthalate (PET). As it was mentioned before active film can be:

- *organic monolayer* ,
- *bilayer of two organic materials*,
- *monolayer bulkheterostructure*,
- *multilayer bulkheterostructure* (*tandem*).

Additional buffer layers are usually inserted between the electrodes and the active layer serving as a selective charge transporting/blocking layers.

Designing a structure with overlapping pillars in the dimensions of the diffusion length range could be the next step in optimizing the performance of OSCs' devices (Fig. 3.1.1) [52].

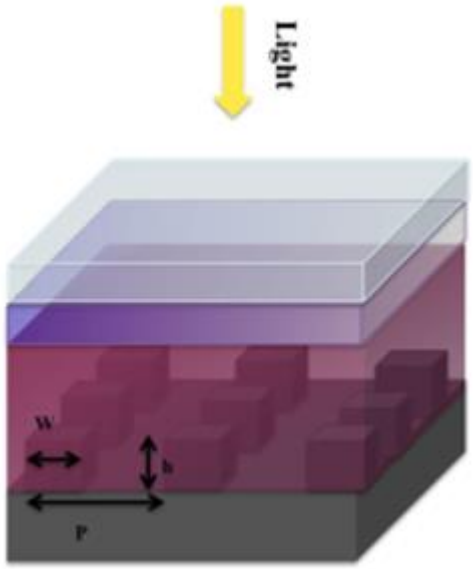

Fig. 3.1.1 *Organic solar cell model geometry with pillars in the range of diffusion length, where all the h, p and w dimensions are in* [*nm*].

OSCs with organic monolayer configuration

The first realised OSCs consisted of organic monolayer sandwiched between electrodes [53]. The photoactive region was very thin, and since both positive and negative photo excited charges were traveling through the same material, the recombination losses were high. Such cells had small efficiency and they were used only to study specific device properties such as current densities regimes through J-V characteristics [54]. Remarkable progress has been made in improving the efficiency of a single-layer OSCs from about 10^{-3} % [49] in the early 1970s to about 1% [50] in 1979. The device behaves as metal-insulator-semiconductor structures due to the presence of an interfacial oxide layer that grows on the metal surface of low work function. While the p-type organic layer is formed the rectifying contact. Also, an improvement in the open-circuit voltage occurs as a result of presence of the oxide layer (see Fig. 3.1.2).

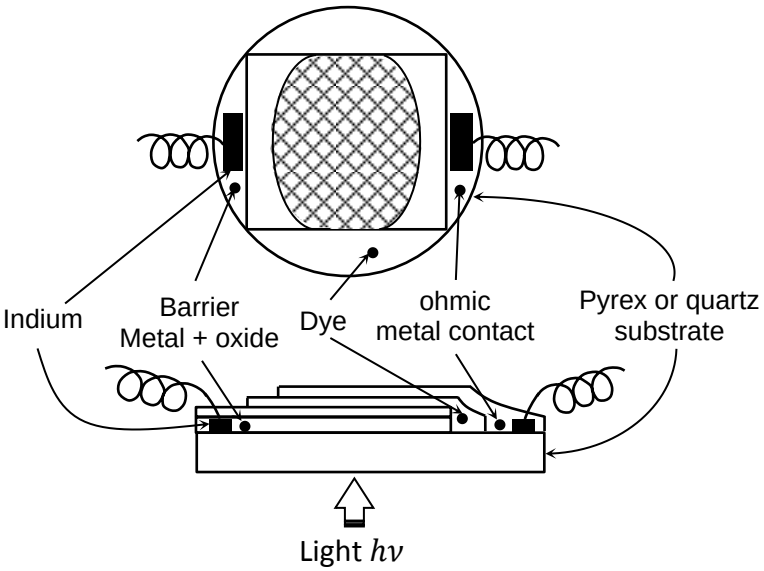

Fig. 3.1.2 *A typical monolayer OPV cell*

OSCs with planar bilayer configuration

In 1986, Tang developed a planar bilayer heterojunction solar cell device with a *PCE* of about 1% [55]. The structure includes an anode, hole transport layer (HTL) followed by acceptor and donor layers, electron transport layer (ETL), and a cathode as shown in Fig. 3.1.3.

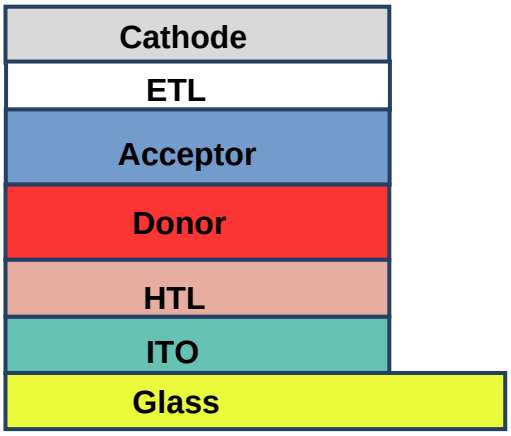

Fig. 3.1.3 *Structure of a bilayer OSCs*

The heterojunction between the donor and acceptor is necessary for the efficient splitting of photogenerated excitons into free carriers in the organic active layer, which is the reason for increasing the device efficiency dramatically compared to the device which consists of a pristine organic material sandwiched between the electrodes. Although the efficiency of the bilayer device represents a significant improvement compared to the single-layer device, it is still suffering from the short of the exciton diffusion length. The active layer thickness in these devices should be more than 100 nm to harvest the most sunlight while the excitons generated far away from the interface will decay before reaching the heterojunction. The architecture engineering of interfacial transport/blocking layers reduces this problem and enables the use of thicker active layers while preserving a short path for exciton diffusion length. The electron and hole transport layers have several functions represented in modifying the work function of electrodes to form an ohmic contact and blocking the electrons and holes to avoid unnecessary charge recombination.

OSCs with bulk heterojunction configuration

A BHJ concept was proposed simultaneously by Heeger [51] and Friend [56] in 1995, bringing a dramatic improvement in the OPVs efficiency. The reason for this improvement is that the donor/acceptor blend form a bi-continuous and interpenetrating network of nanoscale acceptor and donor domains (Fig. 3.1.4). As a result, the interfacial area between the donor and acceptor is increased significantly and each interface is within a distance less than the exciton diffusion length. The BHJ OSCs can harvest the sunlight with near-unity internal quantum efficiency, meaning that any photogenerated exciton will move to the interface and dissociate to form an electron and hole. In BHJ device structure the donor and acceptor phases are mixed randomly and contact the two electrodes simultaneously as shown in Fig. 3.1.4. In order to avoid the unfavorable contact between materials and electrodes (donor contacts with cathode or acceptor with anode) and unfavorable charge collection, interfacial layers such as ETL and HTL are inserted between the active layer and electrodes. Also, electrodes with different work functions were used to create a local field to help the movement of the charges. Furthermore, percolated pathways are required to form in order to transport the holes and electrons to the corresponding electrodes. Acceptor phase as well as donor phase should be continuous to make the transport way for appropriate charge carriers. Otherwise, the charge trapping islands or cul-de-sac (dead-end streets) can form during the thermodynamic phase separation and decrease the device efficiency. Therefore, the active layer morphology is very crucial to achieve high-performance OSCs.

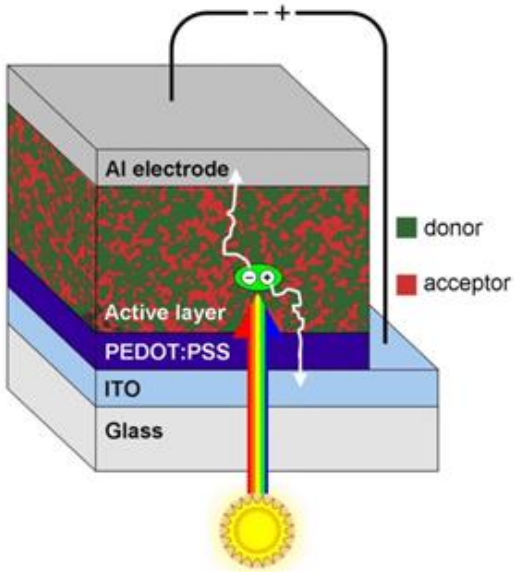

Fig. 3.1.4 *Structure of a BHJ OSCs*

Tandem OSCs' configuration

Most of the infrared spectrum is unable to be converted to excitons, because organic acceptor materials usually absorb in the visible range and donor materials doesn't absorb sunlight. At the same time, the low charge carrier mobility of the OS is limiting their thickness and consequently the amount of absorbed solar light. To overcome these limitations of the single junction structure, the concept of stacking several cells on top of each other to form tandem solar cells was proposed. With this concept, two or even more solar cells can be stacked together with each component having complementary absorption spectra. A typical organic tandem solar cell is shown in Fig. 3.1.5, which is composed of two stacked distinct devices. Each of the solar cells is based on the composite of the

donor and acceptor materials. The solar light which is not absorbed in the bottom device can further proceed towards the top device. The two cells are connected by an intermediate layer, which is employed to allow the recombination of the holes coming from one cell with electrons coming from the other. It is important that the intermediate layer should provide the alignment of the quasi-Fermi level of the acceptor of the bottom cell with the quasi-Fermi level of the donor of the top cell. According to Kirchhoff's law, the voltage of the whole device is equal to the sum of the voltage across each sub-device. As a result, the V_{OC} has in the case of a loss-free connection:

$$(V_{OC})_{Tandem} = (V_{OC})_1 + (V_{OC})_2 + \ldots \tag{3.1.1}$$

The performance of a tandem OSCs improved very fast, the power conversion efficiencies of these cells achieved 17.6% for single-junction [6], and exceed 18.5% for tandem OSCs [7].

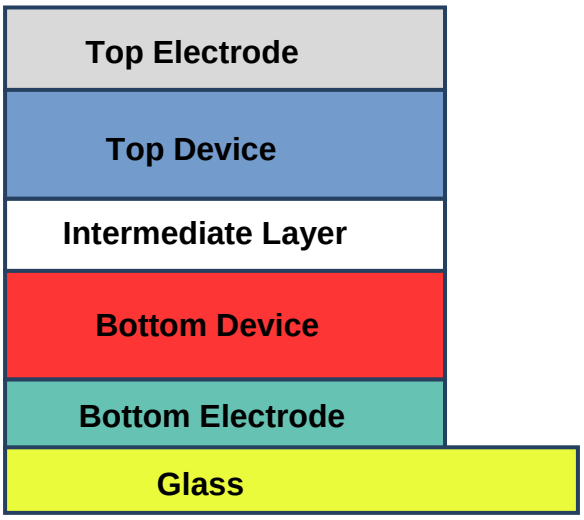

Fig. 3.1.5 *Structure of a tandem OSCs*

3.1.3 Operating principles of OSCs

The OSCs' process of converting solar energy into electricity comprises four steps: exciton generation, exciton diffusion, exciton dissociation, and free charge transport to the electrodes as shown in Fig. 3.1.6. Each step is critical for the efficiency of converting the solar energy into electricity.

Exciton generation

After a photon of incident light is absorbed, an electron is excited from the HOMO to the LUMO of the OSCs. This process is analogous to exciting an electron from the valence band to the conduction band in IS. However, as it was explained in section 2.2.1, immediately after this excitation process neutral Coulomb bound electron-hole pair called singlet exciton is formed. The binding energy of the singlet exciton is much higher than that in IS. As a result, it is estimated that only 10% of the photo excited singlet excitons results in free charge carriers in OS [57]. This is the reason why two components, an electron donor and an electron acceptor, are applied to split the excitons. The band gap of OS determines the portion of the solar spectrum which is absorbed. It is reported that a band gap of 1.1 eV is capable of absorbing 77% of the solar irradiation [27]. Obviously, designing organic materials with low band gap is a step to achieve high-efficiency OSCs.

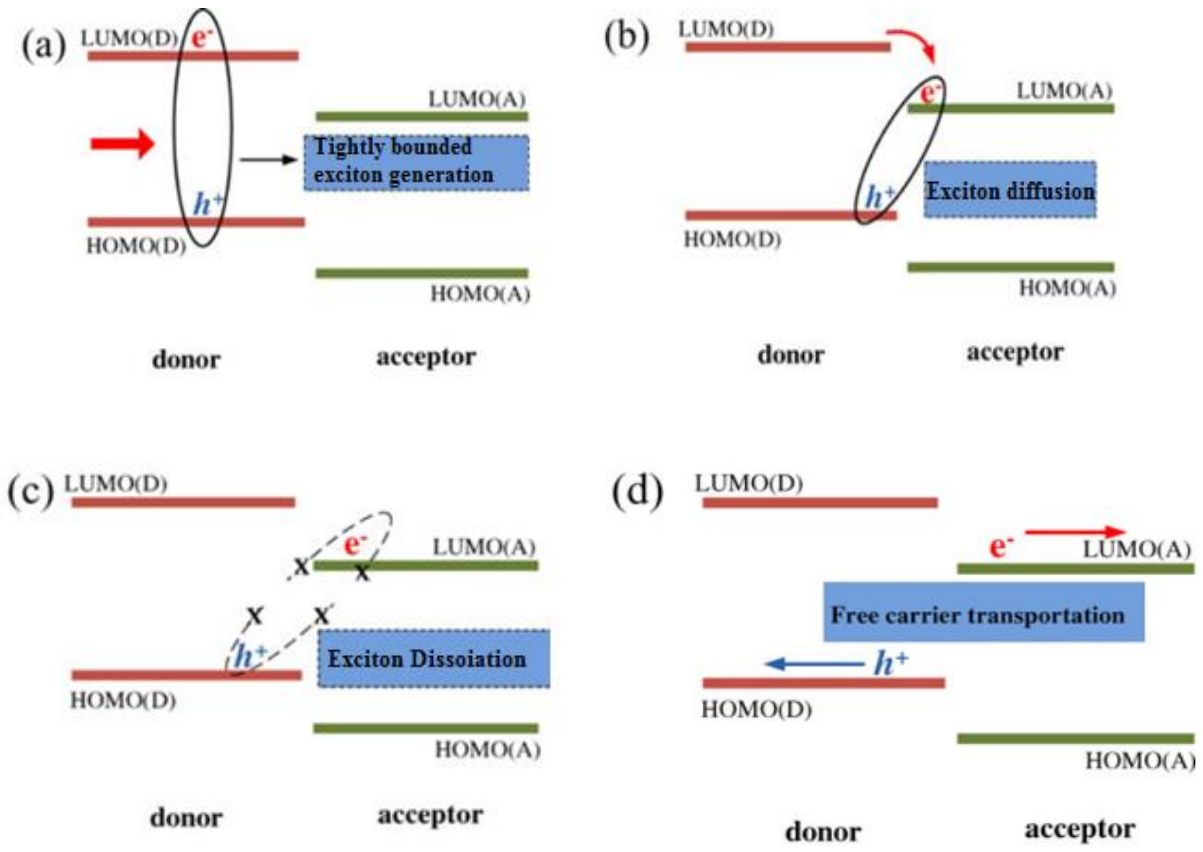

***Fig.* 3.1.6** *Schematic diagram showing basic processes undergoing the OCSs operation* [58].

Exciton diffusion

Excitons need to diffuse to the donor-acceptor (D/A) interface where they can dissociate to generate separated negative and positive charges. Thus, exciton diffusion length limits the the D/A phase separation length. Otherwise, excitons decay via radiative or non-radiative pathways before reaching the D/A interface which results in the loss of their energy. It has been noted that exciton diffusion lengths in organics are usually $\sim 10\, nm$. Also, as the excitons are neutral species, their diffusion happens via random hopping.

Exciton dissociation

In order to split the neutral excitons, either external electric fields or local electric fields created by D/A interface should be provided. At the interface, strong local electric fields exist due to the significant difference in the donor and acceptor work functions. Therefore, blending donor conjugated materials with electron acceptors to create heterojunction interfaces with energy difference is an efficient method to split the neutral excitons and form free charges. Different mechanisms were proposed to describe the dissociation process of the excitons. In most instances, it is believed that exciton state undergoes the down transition to the charge transfer state where the hole sits on the HOMO of a donor material and the electron on the LUMO of a neighbour acceptor molecule. As the hole and electron are still close to each other, they are still bounded by Coulomb force. Additional energy should be supplied to separate charge transfer state and generate free charge carriers.

Charge transport to the electrodes for collection

The separated charges need to transport to the electrodes before they recombine in order to provide good OSCs' efficiency. The mobilities of charge carriers in donor and acceptor materials are thus critical for efficient OSCs' operation. The charge carrier transport (CT) in OSCs is drift and diffusion based. In the case of drift free charges are driven by electric field which is the sum of built in field and external field. The built in electric field is formed by asymmetrical contacts where one low work-function metal is used for collecting electrons (cathode) and the other high work-function metal is used for collecting holes (anode). External field originates from bias voltage applied to electrodes. The concentration gradients of the respective charges lead to diffusion currents.

When charge carriers reach the appropriate interface between organic material and electrode, they are extracted. An Ohmic contact between organic materials and electrodes is desirable for efficient collection of the electrons on the cathode and holes on the anode. The nature of the organic material/electrode interfaces is complex (see Chapter 2.2.2). The usage of metal electrodes with different work functions for cathode and anode, or deposition of interlayers between electrodes and active layers were suggested and applied [59]. However, the mechanism is still debatable, and much remains to be done to understand the intricate details of these interfaces.

3.1.4 Performance characterization of OSCs

Quantum efficiency

There are two types of quantum efficiency (*QE*): External Quantum Efficiency (*EQE*) and Internal Quantum Efficiency (*IQE*). The *EQE* is defined as the ratio of the number of charge carriers collected by the solar cell and the number of incident photons, while the *IQE* represents the same but for absorbed photons. This explains why the value of *IQE* is always higher than the *EQE's* value. The *IQE* is dependent on incident photon wavelength. Also, the *EQE* can be expressed as the function of the wavelength of incident light as:

$$EQE(\lambda) = \frac{hc}{q\lambda}(SR), \tag{3.1.2}$$

where *SR* is the OSCs' spectral response (the ratio of solar cell photocurrent under zero bias and incident power at specific wavelength from the solar spectrum), *h* is the Planck's constant, *c* is the speed of light, and λ is the wavelength of sunlight. The *EQE* is otherwise called the incident photon to current efficiency *IPCE* and it is often calculated as:

$$IPCE = \frac{1240\, J_{SC}}{\lambda\, P_{in}}, \tag{3.1.3}$$

where the wavelength of an incident photon λ in nm, the photocurrent of the device J_{SC} in $\mu A/cm^2$, and P_{in} is the power of incident light in W/cm^2.

Short-circuit current

The short-circuit current density (J_{SC}) (Fig. 3.1.7) is the current density when the bias voltage is zero $(V = 0)$, which is the same conditions as the two electrodes of the cell are short-circuited together. It should be noticed that there is no power produced at this point.

The *EQE* expected under a light source can be estimated from the *EQE* and the spectral irradiance of the light source by integrating the product of *EQE* and the photon flux density E_λ . For the standard AM1.5G spectrum, the calculation is:

$$EQE = \int_0^\infty q\, EQE(\lambda) \frac{\lambda}{hc} E_\lambda^{AM1.5G}(\lambda)\, d\lambda, \tag{3.1.4}$$

where $E_\lambda^{AM1.5G}$ is the spectral irradiance of the AM1.5 G spectrum (Fig. 3.1.8).

Open-circuit voltage

Open-circuit voltage (V_{OC}) (Fig. 3.1.7) is one of the most important factors determining the solar cell efficiency. The V_{OC} is the voltage across the solar cell when no current is flowing through the device (J = 0), which is the same as the device being open-circuited. Because J = 0, no power is actually produced at this voltage. However, the V_{OC} marks the boundary for voltages at which power can be produced and it is the maximum voltage can be provided by a solar cell to an external circuit. The V_{OC} for crystal IS solar cells is derived from the splitting of hole and electron quasi-Fermi levels. The disorder in an organic material induces the gap tail states and relaxation of carriers into these tail states brings the quasi-Fermi level of the electrons down and holes up, and then reduces V_{OC} . Furthermore, the various kinds of carrier recombination can cause additional loss of V_{OC} [60]. In particular, the V_{OC} depends on four important factors, namely temperature, light intensity, the electrode work functions and material microstructure. Although, a generally accepted view is that V_{OC} in the BHJ OSCs originates from the energy offset between the HOMO of the donor and LUMO of the acceptor material [61], [62], early studies reveal that the V_{OC} is determined by the difference in the work functions of the two electrodes, the so-called metal-insulator-metal model [63].

Fill factor

Fill factor (FF) of the solar cell is the ratio of the maximum output power to the product of J_{SC} and V_{OC} . The typical J-V curve for the solar cell is shown in Fig. 3.1.7. It illustrates the V_{OC} , J_{SC} , FF , and the coordinates J_{mpp} and V_{mpp} of the maximum power point (mpp). The shape of the *J-V* curve determines how ‘‘difficult or easy’’ the photogenerated carriers can be extracted out of a device and an ideally FF should be 100% when the J-V curve is exactly a rectangle. The FF is defined as:

$$FF = \frac{J_{mpp} V_{mpp}}{J_{SC} V_{OC}}, \tag{3.1.5}$$

since higher FF refers to higher maximum power, high FF is desired. However, the diode-like behaviour of solar cells results in FF always being less than one.

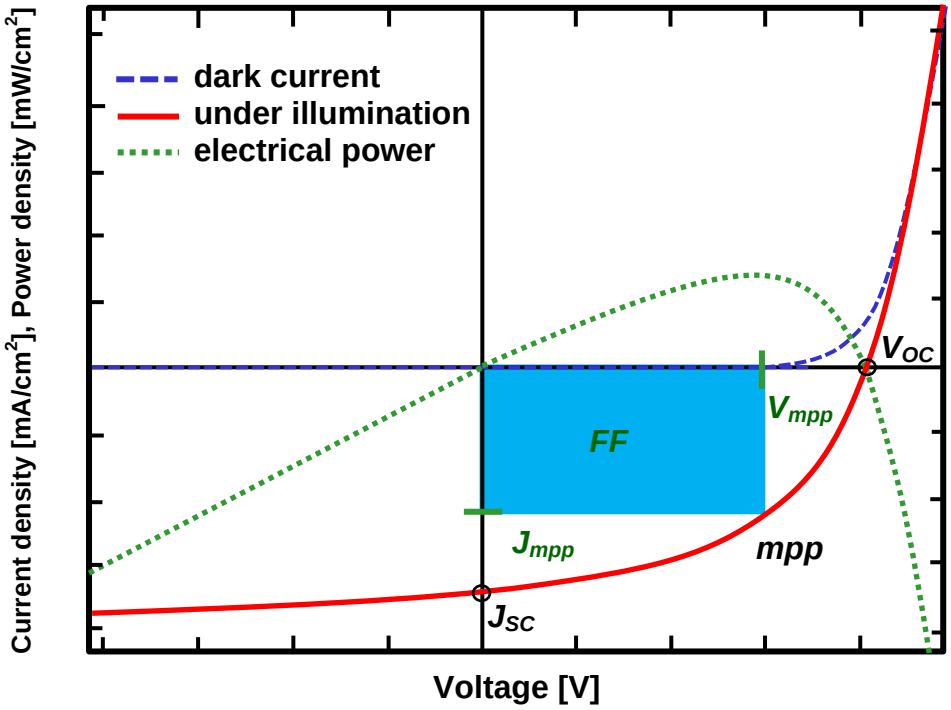

Fig. 3.1.7 *J-V Characteristics of a solar cell in dark and under illumination.*

Power conversion efficiency

The most important parameter of a solar cell is the PCE and it is defined as the percentage of the incident power P_{in} (light power) that is converted into the output power (electrical power). PCE can be denoted as (η) also. The maximum output power is used also for defining PCE, as shown in the following equation form, PCE is written as:

$$PCE = \frac{P_{out}}{P_{in}} = \frac{\left|J_{mpp}\right| \times V_{mpp}}{P_{in}} \times 100\% = \frac{FF \times \left|J_{SC}\right| \times V_{OC}}{P_{in}} \times 100\%. \tag{3.1.6}$$

This form shows clearly that all the FF, J_{SC}, and V_{OC} have a direct impact on PCE.

The PCE of OSCs it is an important parameter since it determines how efficiently the surface occupied by a solar cell is being used for optoelectronic conversion and how much area must be covered with solar cells to produce a demanded amount of electrical power. Higher PCE is certainly desirable. However, there are trade-offs between PCE and cost for each solar cell technology that must be balanced [64].

The PCE is also very dependent on the intensity and spectrum of the light source since solar cells do not absorb and convert photons to electrons at all wavelengths with the same efficiency. To draw comparisons between various solar cells, a standard spectrum must be chosen for the calculation of PCE. Because the spectrum of the sunlight at the Earth's surface varies with location, cloud coverage, and other factors the AM1.5G spectrum, shown in Fig.3.1.8, is the most commonly used as the standard spectrum for measuring and comparing the performance of PVs that are intended for outdoor usage.

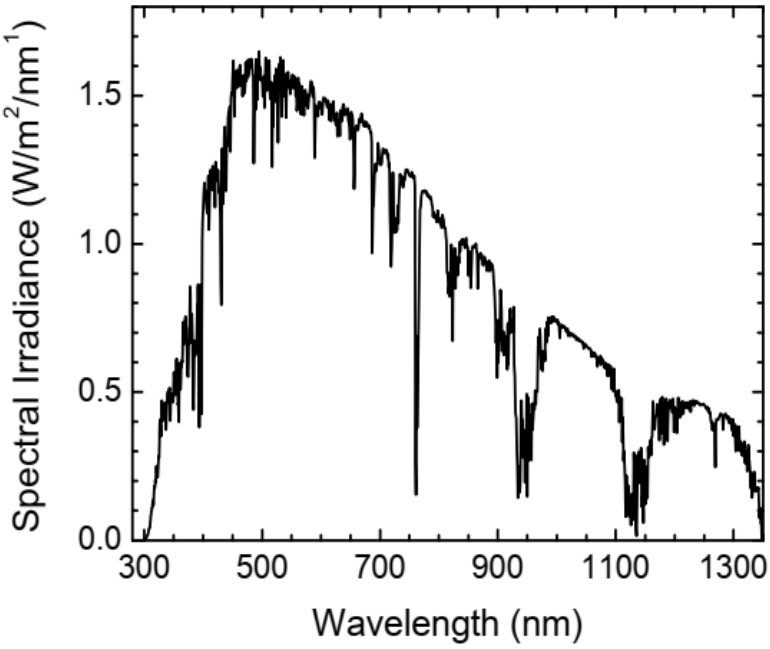

Fig. 3.1.8 *Spectral irradiance of the* AM1.5G *solar spectrum up to* 1350 *nm.*

3.2 The overview of development tracing the efficiency enhancement

In recent years, considerable attention has been paid to overcome the obstacles for commercialisation of OPVs. To take advantage of the low cost of OPVs major improvements are required in their efficiency and lifetime. To realize such hard requirements significant research has been dedicated to the development of OSCs' structure [45, 47, 49,50, 58–61], photoactive layer materials [62–74] and engineering the device interfaces [75,79].

Although the OSCs' structure has already been considered in the previous chapter (Chapter 3.1) the story will supplement here in the context of efficiency enhancement. The first organic dye-sensitized solar cells realised during 1970s and beginning of 1980s [53] had poor efficiency with PCEs of ~0.01–0.10%. Those were the ***single-layer*** cells. Since the positive and negative excited charges were travelling through the same thin photoactive material, the recombination losses were high. The first heterojunction OSCs invented by Tang in 1986 [55] was realised by contacting an electron donor layer with an electron acceptor layer making in that way a ***bi-layer*** cell. This was a milestone in OPV research enabling the PCE to achieve values close to 1.0% for the first time. Because of the high electrical field produced at the D/A interface, excitons diffusing to the interfacial zone were effectively dissociated. However, the D/A interface area was very small, therefore, only excitons near the depletion layer could reach it and become dissociated. Since the typical diffusion lengths of excitons are in the range of 10 nm, while the photoactive film thickness should be more than 100 nm in order to absorb most of the sunlight, the efficiency of these cells was limited. Introduction of ***charge selective transporting/blocking layers*** has also led to improvements in OSCs' efficiency. By adding the hole transporting and electron blocking layer of poly(3,4-ethylenedioxythiophene) polystyrene sulfonate (PEDOT:PSS) to CuPc/C_{60} bi-layer cell the 3.6% efficiency was achieved [65]. The difficulty with bi-layer devices has been overcome by using the new concept of ***bulk heterojunctions*** introduced by Heeger [51] and Halls [56] in 1995. The BHJ are achieved by blending donors and acceptors. Blended cells exhibit a large D/A interface area and most excitons reach the D/A interface. In 2001 Shaheen and co-workers [66] have reported solar cells from MDMO-PPV blended with PCBM with 2.5% efficiency. Li and his colleagues [67] in 2005 utilized P3HT:PC_{61}BM blend film as photoactive layer of OSCs, and achieved the PCE of 4.4%. Heeger and co-workers [68] in 2005 improved the OSCs' PCE up to 5% by optimizing the morphology of P3HT:PC_{61}BM blend film through ***thermal annealing*** method. Soon after the P3HT/PCBM solar cell with PCE of 6% was demonstrated using thermal annealing at temperatures approaching the glass transition [69]. The annealing process was recognised as very important in the production of organic solar cells.

In 2008 Liang et. al. [70] developed a ***new semiconducting polymer*** PTB1 based on alternating thieno-[3,4-b]thiophene (TT) and benzodithiophene (BDT). This result led to a PCE of 5.6% when PTB1:PC_{71}BM photoactive layer is used. Subsequently, they further optimized the molecular structure of PTB1-like derivatives, named PTBn (n=2–7) giving PTB7/PC_{61}BM based OSCs with PCE of 6% in 2009 [71] and PTB7/PC_{71}BM OSCs with PCE 7.4% in 2010 [72]. In 2010, Zhao et al. [73] achieved an encouraging PCE of 6.5% with a new fullerene derivative, Indene-C_{60} bisadduct (ICBA). They also used thermal and solvent annealing of P3HT:ICBA OSCs to achieve stronger absorption and the optimum surface morphology. Liao and his colleagues [74] in 2013 proposed a novel PBDTTT type low bandgap polymer by incorporating 2-ethylhexyl-thienyl group into the BDT unit in PTB7 for extending the absorption spectrum and increasing absorption coefficient. With the inverted device structure ITO/ZnO-C_{60}/PTB_7-Th:PC_{71}BM/MoO_3/Ag the best PCE reached 9.35% [74]. Later, by employing dual-doped ZnO nano-film as cathode interlayer, the

performance was improved to 10.31% [75]. Zhao et. al. in 2016 [76] fabricated BHJ OSCs with the architecture of ITO/ZnO/PffBT4T-C_9C_{13}:$PC_{71}BM$/V_2O_5/Al, and presented a hydrocarbon solvent-based processing system that was used to prepare a better OSCs' morphology and performance than that obtained with conventional solvents. OSCs' PCE increased from 6.4% to 11.7%. The new solvent processing system required no excessive chemical synthesis or new device engineering and was readily applicable to other material systems.

Non-fullerene electron acceptor materials have attracted much attention in recent years. In 2015, Lin and his companions [77] reported an electron acceptor material (ITIC) consisting of a bulky seven-ring fused core and 2-(3-oxo-2,3-dihydroinden-1-ylidene) malononitrile end groups. This new electron acceptor material offered better absorption in the visible region, slightly up-shifting LUMO, higher electron mobility, and improved miscibility with donor materials compared with conventional fullerene acceptors. When using PTB7-Th as donor and ITIC as acceptor, the fullerene-free OSCs showed a record PCE of 6.8%. These preliminary results demonstrate that the fused ring–based push–pull molecule ITIC is a promising alternative to fullerene derivatives for high-performance OSCs. The same author et.al. in 2016 [78] developed an efficient fused-ring electron acceptor (ITIC-Th) based on indacenodithieno[3,2-b]thiophene core and thienyl side-chains for OSCs, which exhibited even stronger absorption in the visible and near infrared regions, lower energy levels, and higher electron mobility. They also found that this ITIC-Th acceptor could match better with low bandgap PTB7-Th or wide bandgap PDBT-T1 donor materials in energy level. The OSCs based on ITIC-Th:PDBTT1 achieved a significantly PCE of 9.6%. In 2016 Zhao and et. al. [79] announced a wide bandgap donor material PBDB-T with thienyl side chains for realizing a better absorption spectrum and more appropriate molecular energy level alignment with ITIC, delivering a certified PCE of 10.78%. As a continuation of research in 2017 [80] they used fluorinated non-fullerene IT-4F as acceptor and PBDB-T-SF as donor to construct photoactive layer. The best device fabricated from PBDBT-SF:IT-4F yielded a certified PCE of 13.1%. Then, in 2018, they further demonstrated the feasibility of replacing fluorine substituents in high-performance PV polymer donors with chlorine, and synthesized a donor PBDB-T-2Cl. As a result, the PBDB-T-2Cl-based OSCs led to a PCE of over 14% [81]. Fei and colleagues in 2018 [82] discovered new non-fullerene acceptor (C8-ITIC) by replaced phenyl side chains of ITIC with alkyl chain, The new acceptor exhibited lower bandgap, higher absorptivity, and an increased crystallinity. The PCE of related OSCs exceeded 13%. Zheng et al. in 2018 [83] improved the interfacial properties in fullerene-free OSCs by an effective strategy for hole-transporting layers (HTLs) through simply mixing WOx nanoparticles with PEDOT:PSS emulsion. The PCE of these devices were 14.57%. Liu et al. in 2019 [84] designed and synthesized a new non-fullerene acceptor TfIF-4FIC via an end-group fluorination. When blended with PBDB-T-2F to fabricate single-junction OSCs, the device offered a PCE of 15%.

The further enhancement of OSCs' performance was achieved by constructing ***tandem solar cells*** for realizing a complementary absorption spectrum. Cui and his colleagues [85] fabricated 2-terminal tandem solar cells using J52-2F:IT-M as front cell and PTB7-Th:IEICO-4F as bottom cell. The best device showed a 14.9% PCE. Also in 2019 [86] the same authors utilized a chlorinated non-fullerene acceptor BTP-4Cl, which exhibits an extended optical absorption and displays a higher voltage than its fluorinated counterpart BTP-4F when used in OSCs' devices. Due to the simultaneously improved short-circuit current density and open-circuit voltage, a high efficiency of 16.5% was achieved.

In 2018, Meng et. al. [7] achieved a power conversion efficiency record of 17.3% using a two-terminal monolithic solution-processed tandem OPV.

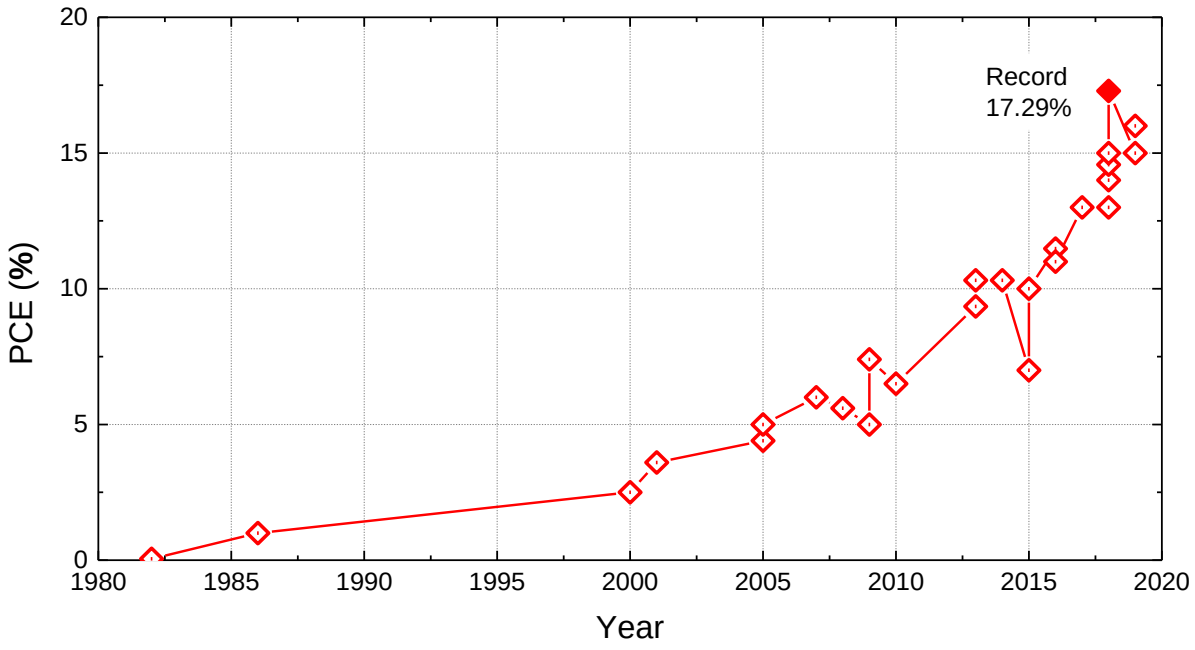

Fig. 3.2.1. *The efficiency enhancement of OSCs in about 40 years*

3.3 The drift diffusion model of organic solar cells

The development of OSCs was driven mainly by experimental research, improving device structure, fabrication methods, active layer material properties, as it was specified in Section 3.2. Although intensive theoretical investigations were conducted general physical model for OS has not been accomplished yet. OSCs' models are to a great extent relying on models developed for inorganic solar cells. Satisfactory results are obtained [13], [33], [87] but it is still not clear what are the most important processes in OSCs which determine their operation. Further development of OSCs is closely related to clarification of physical basis, and the utilization of their full capabilities is entirely conditioned by the development of an accurate and comprehensive physical model.

Searching for a description of intrinsic material physics one should start from Boltzmann equation (BE). The BE is an integrodifferential equation, whose integral term is usually very complicated [87], and there is no hope to find exact analytical solutions. Many numerical methods have been developed that yield very satisfactory results. Deferent approaches such as Monte Carlo, drift-diffusion equations, and hydrodynamic equations, are therefore frequently used [33]. Models most often applied to OSCs are depicted in Fig. 3.3.1.

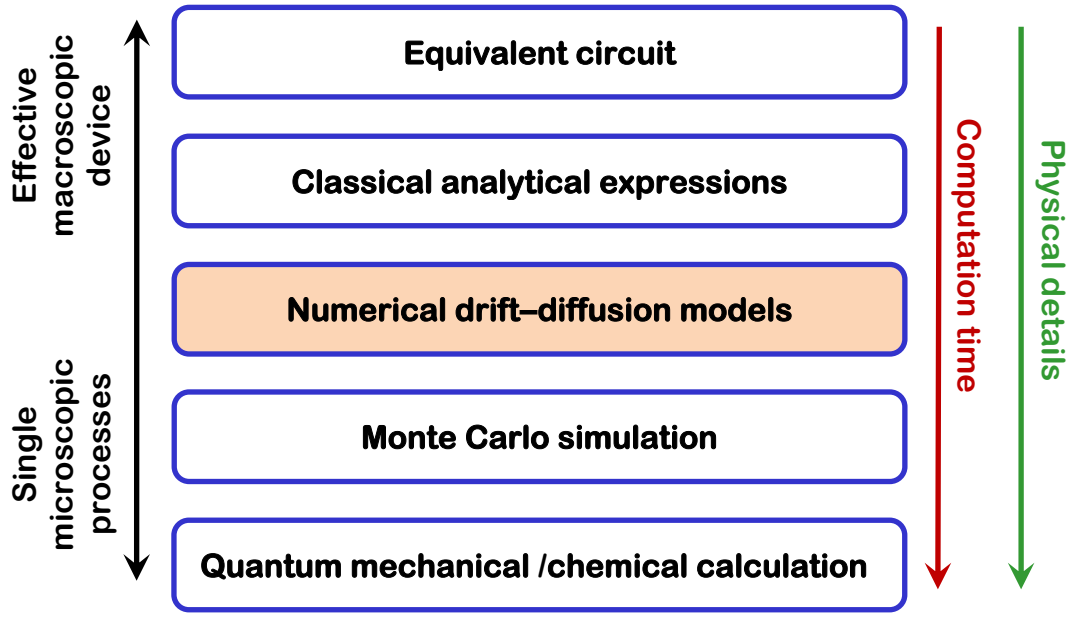

Fig. 3.3.1 *Overview of the simulation models for OS devices* [33].

3.3.1 Drift-diffusion model equations

The drift-diffusion model (DDM) is based on the drift-diffusion transport equations which can be derived from BE [87]. DDM is the main model for describing a semiconductor device operation. It uses an approach between the microscopic and the macroscopic as shown in Fig. 3.3.1. This implies that some of the material parameters such as mobilities, diffusion coefficients, charge carrier lifetimes, recombination coefficients, etc. have to be treated as effective parameters, which are not strictly connected to the underlying physical processes. Either they have to be found from

the experiment, or they can, to some extent, be related to novel theories describing the microscopic processes within OS [13]. It is shown in many articles [88], [89], [58], [90] that drift-diffusion simulations are very powerful in describing the J-V characteristics of OSCs.

The one–dimensional DDM equations include Poisson's equation and the continuity equations for electrons and holes [88].The Poisson's equation has the form:

$$\frac{\partial^2 \varphi}{\partial x^2} = \frac{q}{\varepsilon}\left[n(x) - p(x)\right], \tag{3.3.1}$$

where $\varphi(x)$ is the electrical potential profile in the photoactive layer. The continuity equations for electrons and holes are:

$$\frac{\partial n(x)}{\partial t} = G - R_n + \frac{1}{q}\frac{\partial J_n(x)}{\partial x}, \tag{3.3.2}$$

$$\frac{\partial p(x)}{\partial t} = G - R_p - \frac{1}{q}\frac{\partial J_p(x)}{\partial x}, \tag{3.3.3}$$

where G is the generation rate and $R_{n(p)}$ is the recombination rate of electrons (holes). The current density of electrons $J_n(x)$ and holes $J_p(x)$ are defined by the drift-diffusion expressions:

$$J_n(x) = -q\mu_n n(x)\frac{\partial \varphi(x)}{\partial x} + qD_n\frac{\partial n(x)}{\partial x}, \tag{3.3.4}$$

$$J_p(x) = -q\mu_p p(x)\frac{\partial \varphi(x)}{\partial x} - qD_p\frac{\partial p(x)}{\partial x}, \tag{3.3.5}$$

where $\mu_{n(p)}$ is the electron (hole) mobility and $D_{n(p)}$ is the electron (hole) diffusion coefficient, which is assumed to obey the Einstein relation,.

$$D_{n(p)} = \mu_{n(p)} V_t, \tag{3.3.6}$$

with V_t is the thermal voltage:

$$V_t = k_B T / q, \tag{3.3.7}$$

3.3.2 Charge carrier generation rate

It was shown that the interference effects have a strong impact on OSCs' behavior [89], [58]. The transfer-matrix optics (TMO) is used for calculation of the optical field distribution in the OSCs' active layer.

Multiple interference in multilayer thin film structure calculated by TMO.

The thin-film multilayer structure is shown in Fig. 3.3.2. with forward and backward propagating optical electric field components denoted as $E^+$and E^-, respectively.

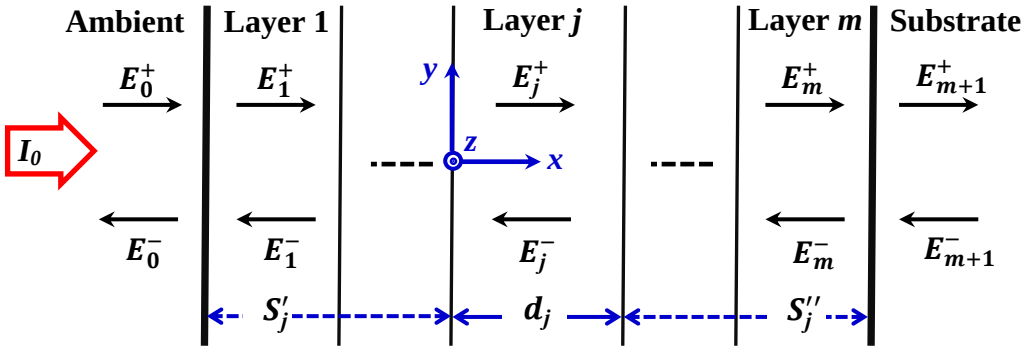

Fig. 3.3.2 *Schematic structure of m-layers between ambient and substrate* [91].

When TMO calculation is applied to OSCs it is assumed that:

- layers are homogenous and isotropic,
- the normal incidence of light is considered,
- light is presented as a plane wave.

The interface I and propagation L matrices are defined for each interface and layer. The interface matrix I_{jk} between the layer j and the layer k $(k = j + 1)$ has the form:

$$I_{jk} = \begin{bmatrix} \left(\tilde{n}_j + \tilde{n}_k\right)/2\tilde{n}_j & \left(\tilde{n}_j - \tilde{n}_k\right)/2\tilde{n}_j \\ \left(\tilde{n}_j - \tilde{n}_k\right)/2\tilde{n}_j & \left(\tilde{n}_j + \tilde{n}_k\right)/2\tilde{n}_j \end{bmatrix}, \tag{3.3.8}$$

where $\tilde{n}$ is the complex index of refraction for each layer $\tilde{n} = n + i\kappa$. The propagation matrix for the layer j is defined as:

$$L_j = \begin{bmatrix} \exp\left(-i\xi_j \cdot d_j\right) & 0 \\ 0 & \exp\left(i\xi_j \cdot d_j\right) \end{bmatrix}, \tag{3.3.9}$$

where $\xi_j = \dfrac{2\pi\tilde{n}_j}{\lambda}$, and d_j is the thickness of the layer j.

The incident optical electric field (subscript 0) is related to the field in the substrate (subscript $m+1$) by:

$$\begin{bmatrix} E_0^+ \\ E_0^- \end{bmatrix} = S \begin{bmatrix} E_{m+1}^+ \\ E_{m+1}^- \end{bmatrix}, \tag{3.3.10}$$

where S is the total transfer matrix:

$$S = \begin{bmatrix} S_{11} & S_{12} \\ S_{21} & S_{22} \end{bmatrix} = \left(\prod_{v=1}^{m} I_{(v-1)v} L_v \right) I_{m(m+1)} . \tag{3.3.11}$$

The optical electric field profile inside the layer j is calculated as:

$$E_j(x) = E_j^+(x) + E_j^-(x) . \tag{3.3.12}$$

To determine this optical electric field profile it is necessary to express S matrix as $S = S'_j \, L_j \, S''_j$ where:

$$S'_j = \begin{bmatrix} S'_{j11} & S'_{j12} \\ S'_{j21} & S'_{j22} \end{bmatrix} = \left(\prod_{v=1}^{j=1} I_{(v-1)v} L_v \right) I_{(j+1)j} , \tag{3.3.13}$$

$$S''_j = \begin{bmatrix} S''_{j11} & S''_{j12} \\ S''_{j21} & S''_{j22} \end{bmatrix} = \left(\prod_{v=\mathrm{j}+1}^{m} I_{(v-1)v} L_v \right) I_{m(m+1)} . \tag{3.3.14}$$

Then for layer j:

$$\begin{bmatrix} E_0^+ \\ E_0^- \end{bmatrix} = S'_j \begin{bmatrix} E_j'^+ \\ E_j'^- \end{bmatrix}, \tag{3.3.15}$$

and

$$\begin{bmatrix} E_j''^+ \\ E_j''^- \end{bmatrix} = S''_j \begin{bmatrix} E_{m+1}^+ \\ E_{m+1}^- \end{bmatrix}, \tag{3.3.16}$$

where $E_j'^+$ and $E_j'^-$ refer to the left boundary $(j-1)\,|\,j$ in the layer j. $E_j''^+$ and $E_j''^-$ refer to the right boundary $j\,|\,(j+1)$ in the same layer j. After manipulations, (for more details of derivation see Ref. [91]) 3.3.12 becomes:

$$E_j(x) = E_j^+(x) + E_j^-(x) = t_j^+ \left[\exp\left(ik_j x\right) + r_j'' \exp\left(ik_j(2d_j - x)\right) \right] E_0^+, \quad (3.3.17)$$

$$t_j^+ \left[S'_{j11} + S'_{j12}\, r_j'' \exp\left(i2k_j\, d_j\right) \right]^{-1}, \quad (3.3.18)$$

$$r_j'' = S''_{j21} / S''_{j11}\,. \quad (3.3.19)$$

When the optical electric field denoted by $E_j(x)$ in 3.3.17 is determined in the layer *j*, the intensity of light at the position *x* within *j*-layer of the device is:

$$I_j(x,k) = T_j I_0(\lambda) \Big[\exp\left(-\alpha_j x\right) + \rho_j''^2 \exp\left(-\alpha_j(2d_j - x)\right) + 2\rho_j'' \exp\left(-\alpha_j d_j\right) \cos\left(\frac{4\pi n_j}{\lambda}(d_j - x) + \delta_j'' \right) \Big], \quad (3.3.20)$$

where $I_0(\lambda)$ is the incident light intensity, $T_j = \left(n_j / n_0\right) t_j^2$ is the internal intensity transmittance, ρ_j and δ_j are the absolute value and the argument of the complex reflection coefficient. The first and second terms within the square brackets of 3.3.20 originate from the optical electric field propagating in the positive *x*-direction $E_j^+(x)$, and in the negative x-direction $E_j^-(x)$, respectively, and the third term results from the interference of the first two. When the thickness of the thin film becomes comparable with the light wavelength, the third term becomes especially important. But when the thickness is much larger than the light wavelength $\left(d_j \gg \lambda\right)$, the third term can be neglected. Equation 3.3.20 converges to the Beer-Lambert law for bulk materials.

Once the light intensity distribution is calculated in the active layer, the dissipated energy rate per unit volume *Q* can be determined as:

$$Q(x,\lambda) = \alpha(\lambda)\, I(x,\lambda), \quad (3.3.21)$$

where $\alpha(\lambda) = 2\pi\kappa/\lambda)$ is the absorbtion coefficient of the active layer. Then, the photon density absorbed in the active layer is:

$$n(x) = \int \frac{\lambda}{hc} Q(x,\lambda) d\lambda\,. \quad (3.3.22)$$

If electron-hole pairs are assumed to be generated directly by exction dissociation with internal quantum efficiency η_i then the generation rate is calculated as:

$$G(x) = \eta_i \int \frac{\lambda}{hc} Q(x,\lambda) d\lambda\,. \quad (3.3.23)$$

If the exciton dissociation process is described as a two-step electric field dependent process through Braun's model [88], [92] then the generation rate is calculated as in Ref. [88].

3.3.3 Charge cerriers transport

The CT through a disordered material is not a simple displacement as in a homogeneous IS. It is affected and even dominated by a large concentration of localized states, either inside bulk or at the boundaries (surface states). It was shown, both empericaly [93] and theoriticaly (Gaussian Disorder Model- GDM) [28] that the mobility is temperature and electric field dependent (see Sec. 2.2.1). Also, there is an improved model called EGDM (Extended GDM) which includes the carrier concentration mobility dependence [28]. The mobility dependence on electric field and carrier concentration is considered weak at low electric fields (less than 10^7 V/m) and low carrier concentrations [88]. Therefore, it is usually safe to assume a constant mobility from short-circuit to open-circuit range.

3.3.4 Recombination

The basic model used for charge carrier recombination in OS is the Langevin recombination as it was introduced in Sec. 2.2.1. However, in a BHJ solar cell charge carriers can only recombine at the D/A interface. Therefore, the coefficient γ is not necessarily equal to the calculated Langevin coefficient $\gamma_L = (q/\varepsilon)(\mu_n + \mu_p)$ and in fact, often is reduced [28]. Hence, carrier recombination follows a modified (reduced) Langevin character and recombination rate is modeled according to the following rate equation:

$$\frac{dn}{dt} = -\gamma(n)n^2 = -\xi\frac{q(\mu_n + \mu_p)}{\varepsilon}n^{\lambda+1}, \qquad (3.3.24)$$

with ξ is a Langevin reduction factor, and $\lambda+1$ is the total recombination order. The rate constant is dependent on the charge carrier density. For example the total recombination order determined for the annealed RR-P3HT:PCBM blends is increased by 0.45 ($\lambda+1=2.45$) compared with standard Langevin order [94] and it is in a good agreement with experiment [95]. The reduction factor ξ used to modify the Langevin equation is closely related to the morphology of the blend and the effective interfacial area. Experimentally, the rate constants corresponding to a second-order recombination process for RR-P3HT:PCBM were found to be $\xi = 10^{-2} - 10^{-3}$ times lower than that estimated by the Langevin formula [28], [94].

3.3.5 Boundary conditions

The system of equations formed by the Poisson's equation and the continuity equations of electrons and holes is classified as the boundary value problem. To obtain the solution of such a system it is necessary to specify the electrical potential and carrier densities at both ends, $x = 0$ (anode) and $x = d$ (cathode), where d is the active layer thickness. Two different types of boundary conditions (BCs) are usually used in OSCs' modeling, fixed, Dirichlet boundary conditions (DBCs) [88] [96] and mixed, Robin boundary conditions (RBCs) [97], [98].

- The DBCs imply ideal ohmic contacts, so the surface electrical potential and carrier concentrations are defined as [88]:

At anode: $\varphi(x=0)=0$ (3.3.25a)

$$n(x=0)=N_C\exp\left(-E_g/k_BT\right), \quad (3.3.25b)$$

$$p(x=0)=N_V\,. \quad (3.3.25c)$$

At Cathode: $\varphi(x=d)=E_g-V\,,$ (3.3.26a)

$$n(x=d)=N_C\,, \quad (3.3.26b)$$

$$p(x=d)=N_V\exp\left(-E_g/k_BT\right). \quad (3.3.26c)$$

- The RBCs include surface recombination and thermal injection at contacts and they are defined as:

At anode: $\varphi(x=d)=0\,,$ (3.3.27a)

$$\left(n(x=0)-n_{th}^{a}\right)S_n^a=\pm\frac{1}{q}J_n(x=0)\,, \quad (3.3.27b)$$

$$\left(p(x=0)-p_{th}^{a}\right)S_p^a=\pm\frac{1}{q}J_p(x=0)\,, \quad (3.3.27c)$$

At cathode: $\varphi(x=d)=-V+V_{bi}\,,$ (3.3.28a)

$$\left(n(x=d)-n_{th}^{c}\right)S_n^c=\pm\frac{1}{q}J_n(x=d)\,, \quad (3.3.28b)$$

$$\left(p(x=d)-p_{th}^{c}\right)S_p^c=\pm\frac{1}{q}J_p(x=d)\,, \quad (3.3.28c)$$

where $S_{n(p)}^{a(c)}, n_{th}^{a(c)},$ and $p_{th}^{a(c)}$ are specified in section 2.3, and the choice of the +/– sign depends on the sign of corresponding current density.

When the injection barrier heights for majority carriers are zero $\Phi_{Bn}=\Phi_{Bp}=0$, and all SRVs tend to infinity $S_n^a=S_p^a=S_n^c=S_p^c\to\infty$ then the RBCs are transformed into DBCs.

3.3.6 Numerical calculations

The discretization of the system of equations is usually done by using the finite difference method (FDM) [99] including Scharfetter and Gummel (S-G) approach [100]. For system equations 3.3.1- 3.3.5 together with RBCs (3.3.27, 3.3.28) detailed discretization and derivation of algebraic system of equations is given in Appendix A.

The domain discretization is done by dividing the active layer thickness into N equal elements $\Delta x = d/N = h$ as shown in the Fig. 3.3.3. Further, the equations are discretized by FDM together with S-G method (see Appendix A). The final system consists of $3\times(N+1)$ algebraic equations, each equation is a function of $3\times(N+1)$ variables.

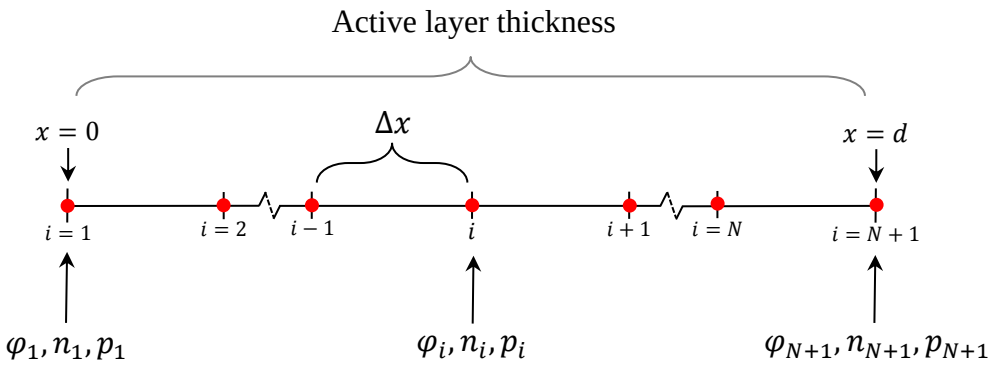

Fig. 3.3.3 *The domain discretization.*

The variables can be presented in the form of vectors:

$$\begin{aligned} \mathrm{v} &= (\varphi_1, \varphi_2, ..., \varphi_{N+1}), \\ \mathrm{n} &= (n_1, n_2, ..., n_{N+1}), \\ \mathrm{p} &= (p_1, p_2, ..., p_{N+1}), \end{aligned} \tag{3.3.29}$$

and the system of equations is as follows:

$$\begin{aligned} f_{\mathrm{v}1} &= (\mathrm{v}, \mathrm{n}, \mathrm{p}) = 0, \\ f_{\mathrm{n}1} &= (\mathrm{v}, \mathrm{n}, \mathrm{p}) = 0, \\ f_{\mathrm{p}1} &= (\mathrm{v}, \mathrm{n}, \mathrm{p}) = 0, \\ f_{\mathrm{v}2} &= (\mathrm{v}, \mathrm{n}, \mathrm{p}) = 0, \\ f_{\mathrm{n}2} &= (\mathrm{v}, \mathrm{n}, \mathrm{p}) = 0, \\ f_{\mathrm{p}2} &= (\mathrm{v}, \mathrm{n}, \mathrm{p}) = 0, \\ &\vdots \\ f_{\mathrm{v}_{N+1}} &= (\mathrm{v}, \mathrm{n}, \mathrm{p}) = 0, \\ f_{\mathrm{n}_{N+1}} &= (\mathrm{v}, \mathrm{n}, \mathrm{p}) = 0, \\ f_{\mathrm{p}_{N+1}} &= (\mathrm{v}, \mathrm{n}, \mathrm{p}) = 0, \end{aligned} \tag{3.3.30}$$

The notation can be simplified by using $\mathbf{x} = (\mathrm{v}, \mathrm{n}, \mathrm{p})$ and denoting equation system as **F**:

$$\mathbf{F}(\mathbf{x}) = 0\,, \tag{3.3.31}$$

Newton's algorithm [99] is a convenient method to solve such a system of equations. The function **F**(**x**) can be linearly developed as:

$$\mathbf{F}(\mathbf{x} + \Delta\mathbf{x}) = \mathbf{F}(\mathbf{x}) + \mathbf{J}(\mathbf{x}) \cdot \Delta\mathbf{x}\,, \tag{3.3.32}$$

where **J** is the Jacobian square matrix of dimensions $3\times(N+1)\times3\times(N+1)$ whose elements are the corresponding partial derivatives of the three vectors $f_\mathrm{v}, f_\mathrm{n}, f_\mathrm{p}$ with respect to $\mathrm{v}_i, \mathrm{n}_i, \text{and}\, \mathrm{p}_i$ as:

$$\mathbf{J} = \begin{bmatrix} \frac{\partial f_{\mathrm{v}_1}}{\partial \mathrm{v}_1} & \cdots & \frac{\partial f_{\mathrm{v}_1}}{\partial \mathrm{v}_{N+1}} & \frac{\partial f_{\mathrm{v}_1}}{\partial \mathrm{n}_1} & \cdots & \frac{\partial f_{\mathrm{v}_1}}{\partial \mathrm{n}_{N+1}} & \frac{\partial f_{\mathrm{v}_1}}{\partial \mathrm{p}_1} & \cdots & \frac{\partial f_{\mathrm{v}_1}}{\partial \mathrm{p}_{N+1}} \\ \frac{\partial f_{\mathrm{n}_1}}{\partial \mathrm{v}_1} & \cdots & \frac{\partial f_{\mathrm{n}_1}}{\partial \mathrm{v}_{N+1}} & \frac{\partial f_{\mathrm{n}_1}}{\partial \mathrm{n}_1} & \cdots & \frac{\partial f_{\mathrm{n}_1}}{\partial \mathrm{n}_{N+1}} & \frac{\partial f_{\mathrm{n}_1}}{\partial \mathrm{p}_1} & \cdots & \frac{\partial f_{\mathrm{n}_1}}{\partial \mathrm{p}_{N+1}} \\ \frac{\partial f_{\mathrm{p}_1}}{\partial \mathrm{v}_1} & \cdots & \frac{\partial f_{\mathrm{p}_1}}{\partial \mathrm{v}_{N+1}} & \frac{\partial f_{\mathrm{p}_1}}{\partial \mathrm{n}_1} & \cdots & \frac{\partial f_{\mathrm{p}_1}}{\partial \mathrm{n}_{N+1}} & \frac{\partial f_{\mathrm{p}_1}}{\partial \mathrm{p}_1} & \cdots & \frac{\partial f_{\mathrm{p}_1}}{\partial \mathrm{p}_{N+1}} \\ \vdots & \ddots & \vdots & \vdots & \ddots & \vdots & \vdots & \ddots & \vdots \\ \frac{\partial f_{\mathrm{v}_{N+1}}}{\partial \mathrm{v}_1} & \cdots & \frac{\partial f_{\mathrm{v}_{N+1}}}{\partial \mathrm{v}_{N+1}} & \frac{\partial f_{\mathrm{v}_{N+1}}}{\partial \mathrm{n}_1} & \cdots & \frac{\partial f_{\mathrm{v}_{N+1}}}{\partial \mathrm{n}_{N+1}} & \frac{\partial f_{\mathrm{v}_{N+1}}}{\partial \mathrm{p}_1} & \cdots & \frac{\partial f_{\mathrm{v}_{N+1}}}{\partial \mathrm{p}_{N+1}} \\ \frac{\partial f_{\mathrm{n}_{N+1}}}{\partial \mathrm{v}_1} & \cdots & \frac{\partial f_{\mathrm{n}_{N+1}}}{\partial \mathrm{v}_{N+1}} & \frac{\partial f_{\mathrm{n}_{N+1}}}{\partial \mathrm{n}_1} & \cdots & \frac{\partial f_{\mathrm{n}_{N+1}}}{\partial \mathrm{n}_{N+1}} & \frac{\partial f_{\mathrm{n}_{N+1}}}{\partial \mathrm{p}_1} & \cdots & \frac{\partial f_{\mathrm{n}_{N+1}}}{\partial \mathrm{p}_{N+1}} \\ \frac{\partial f_{\mathrm{p}_{N+1}}}{\partial \mathrm{v}_1} & \cdots & \frac{\partial f_{\mathrm{p}_{N+1}}}{\partial \mathrm{v}_{N+1}} & \frac{\partial f_{\mathrm{p}_{N+1}}}{\partial \mathrm{n}_1} & \cdots & \frac{\partial f_{\mathrm{p}_{N+1}}}{\partial \mathrm{n}_{N+1}} & \frac{\partial \mathrm{fp}_{N+1}}{\partial \mathrm{p}_1} & \cdots & \frac{\partial f_{\mathrm{p}_{N+1}}}{\partial \mathrm{p}_{N+1}} \end{bmatrix}. \tag{3.3.33}$$

As in the case of solving one equation of a single variable using the classic Newton method, the first step is an initial guess. The vector $\mathbf{x}_0$ is defined with the beginning of the iterative procedure. The function **F** is approximated by linear development in the vicinity of the initial guess vector $\mathbf{x}_0$ as:

$$\mathbf{F}(\mathbf{x}) \approx \mathbf{F}(\mathbf{x}_0) + \mathbf{J}(\mathbf{x}_0) \cdot (\mathbf{x} - \mathbf{x}_0)\,. \tag{3.3.34}$$

Then the solution of 3.3.31 could be found as:

$$\mathbf{x} = \mathbf{x}_0 - \left(\mathbf{J}(\mathbf{x}_0)\right)^{-1} \mathbf{F}(\mathbf{x}_0)\,, \tag{3.3.35}$$

The solution $\mathbf{x}$ is the approximate zero of the function $\mathbf{F}(\mathbf{x})$, and to get the solution with better accuracy, the iterative procedure is applied by taking $\mathbf{x}$ as a new initial guess.

In general, the vector $\mathbf{x}$ can be updated as:

$$\mathbf{x}_{k+1} = \mathbf{x}_k + \Delta\mathbf{x}_k = \mathbf{x}_k - \left(\mathbf{J}(\mathbf{x}_k)\right)^{-1}\mathbf{F}(\mathbf{x}_k), \qquad (3.3.36)$$

where *k* is the iteration counter.

After each iteration the absolute value of $\Delta\mathbf{x}_k$ is compared with a pre-specified tolerance δ which defines the accuracy level of the calculation. If $\Delta\mathbf{x}_k > \delta$ then the iterations proceed and if $\Delta\mathbf{x}_k < \delta$ the iterative process ends, and the last calculated vector $\mathbf{x}$ is the solution.

Newton's method converges quadratically. When carrying out this method the system converges quite rapidly once the approximation is close to the actual solution of the nonlinear system. This is seen as an advantage because Newton's method may require fewer iterations, compared to other methods with a lower rate of convergence to reach the solution. However, the success of an algorithm is highly dependent on initial guess. In this thesis the analytical solution of eqs. 3.3.1–3.3.5 obtained under the assumption of constant electric field and monomolecular recombination [101], [90] is used for the initial guess. For the initial guess calculations the multiple interference effects in OSCs' active layer (see Sec.3.3.2) don't need to be taken into account, much simpler approach which assumes a Beer-Lambert absorption profile can be applied to determine the generation rate profile [90].

3.4 S-shaped J-V characteristic in organic solar cells

The S-shaped J-V characteristic is a deformation that is sometimes observed in the OSCs. This deviation from a regular exponential current-voltage relation leads to a reduction of the FF and the PCE, even though the V_{oc} and J_{sc} are not necessarily affected. Also, the maximum power point decreases significantly, as can be seen in Fig. 3.4.1.

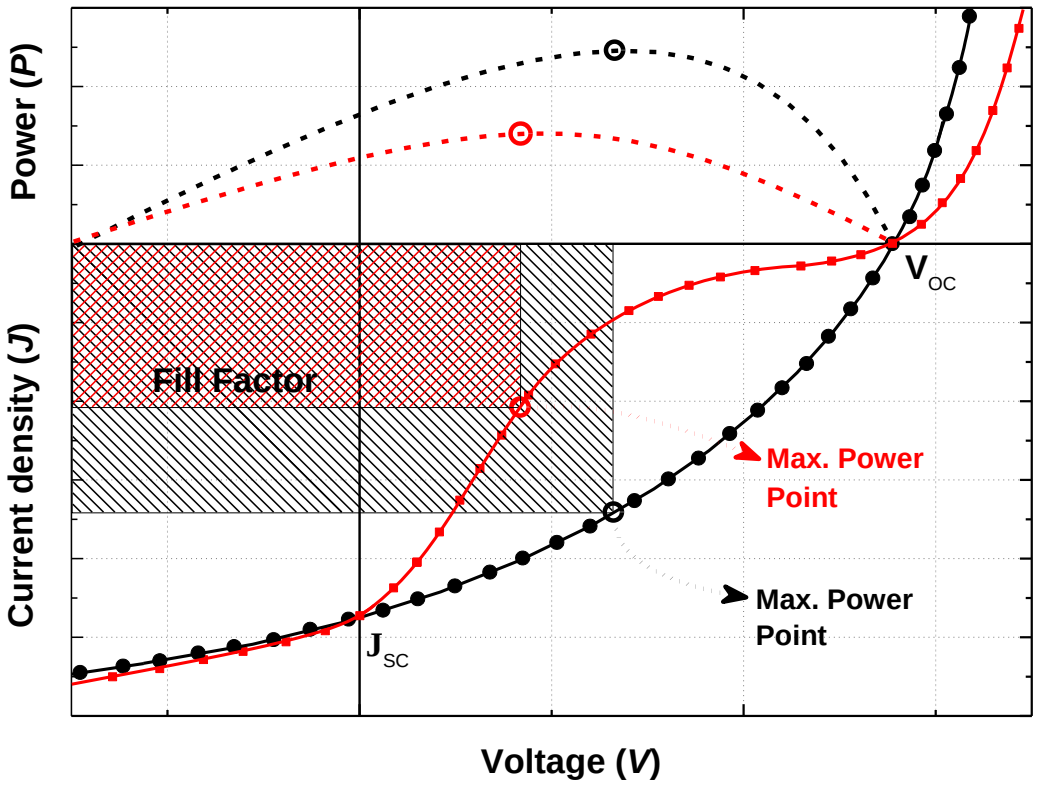

Fig. 3.4.1 *Normal J-shaped (black) and S-shaped (red) J-V characteristics*
The solid lines show the J-V curve, and the dashed lines show the P-V curve

Many researchers intensively investigated the S-shaped J-V curve in OSCs in order to find the causes of such behaviour. In 2007 Glatthaar et al. [102] and Geiser et al. [103] stated that the reason for the kink of the J-V curve in P3HT:PCBM solar cell under illumination is a slow charge transfer at one of the electrical contacts of the absorber layer. In 2008, Gupta and his group [104], [105] have observed that the shape of the J-V characteristics strongly depends on the quality of polymer cathode interface in the two different OSCs with P3HT-PCBM and MEHPPV-CNPPV active layer.

The physio-chemical defects in the polymer–metal interface give rise to the charge carrier accumulation (due to inefficient collection) and the consequent space-charge effect. Uhrich et al. [106] in the same year interpreted the S-shaped J-V characteristics in terms of insufficient energy level alignment between the photoactive layer 4P-TPD:C60 and the hole transport layer. A year later Kumar et al. [107] investigated the reasons for the formation of an S-shape feature in the J-V curves of P3HT:PCBM solar cells. Starting from the fact that interfaces play a critical role in charge extraction and electric-field distribution, they came to the conclusion that Interfacial dipoles, defects, and traps can create barriers for carrier extraction leading to this anomalous feature. In the same year, Jin and his colleagues [108] again observed that the polymer-electrode interfaces, both on the anode and the cathode side, had a large effect on the PV parameters of P3HT:PCBM based solar cell, especially on FF. Low conductivity and high resistance caused by the polymer-electrode interfacial effect are found to be a reason for the S-shaped J-V curve of the degraded sample. One more evidence for reduced charge carrier extraction rates causing S-curve in P3HT:PCBM based BHJ solar cells is given in [109]. The experiments done in 2010 by Lilliedal et al. [110] clearly show the appearance of an S-shape in the J-V curves of roll-to-roll processed inverted P3HT:PCBM PSCs can be effectively removed by photo-annealing after production. Wagenpfahl and his group [39] explained the J-V characteristic S-deformation by the reduced majority carrier SRVs at contacts. Tress et al. in 2011 [111] have performed DDM simulations of bilayer devices showing the appearance of S-kinks in the J-V curve when the electron and hole mobilities are imbalanced with a mismatch factor of more than 100 ($\mu_n/\mu_p > 100$). Wang et al. [112] also investigated small molecule BCP: C60 OSCs, and observed that S-shapes were introduced and became more pronounced with increasing thickness of the exciton blocking layer BCP. The simulation results indicate that when the BCP layer is thicker than 15nm the interfacial recombination induce an S-shape characteristic in the J-V curves. Also, Tress et al. in 2011 [113], 2013 [21], [114] provided further theoretical and experimental evidence, and pointed out the importance of charge transport barriers at interfaces between the active layer and transport layers as well as between transport layers and electrodes. Explanations for the shape of the J-V curves were given using DDM simulations, showing the importance of selective contacts. Also, Finck and his colleagues [115] have shown that even a many order of magnitude mismatch of the carrier mobilities is insufficient to generate S-shaped J-V curves. Instead, they proved that S-shaped J-V curves result when a sigmoid-shaped electron mobility profile is entered into the DDM calculation. At the end of 2013 Saive et al. [116] measured the potential distributions by scanning Kelvin probe in well operating and degraded (which exhibit S-shaped J-V curve) P3HT/PCBM solar cells and compared them. They found that in the case of S-shaped J-V characteristics, there is a huge potential drop at the PCBM/Al top contact, which does not occur in solar cells with normal J-V Characteristics. In 2014 Sandberg and his group [15] used a numerical DDM to clarify the effect of imperfect contacts leading to S-shaped J-V characteristics in BHJ solar cells.

The effect of reduced SRVs, interfacial minority carrier doping, and traps for majority carriers at the electrodes are simulated and compared to the case with increased injection barriers. They found in general two different causes of S-shaped J-V curve reduced surface recombination for the majority carriers and the minority carrier doping and traps for majority carriers. Also, in 2014 Sims et al. [117] showed that a low hole mobility at hole conductive layer could produce an S-shaped J-V curve. Love and his group in 2016 [118] stated that the blends cast from chlorobenzene have reasonably high mobility, so a build-up of space charge simply due to an imbalance in carrier mobilities can likely be ruled out as a cause of S-shaped J-V curve in OSCs. Instead, the J-V curve deviation can be ascribed to changes in vertical phase separation. In 2019 Pockett [119] considered the degradation of OSCs for devices with interlayers and with no interlayers in their structure. The strong S-shape deviation in J-V curve appeared in devices having interlayers.

The conclusion was made that S-shape kink in J-V characteristics originates from some interlayer physics. Sesa et al. [120] in 2019 studied the transition of ITO/PEDOTPSS/P3HT:PCBM/Al J-V profiles from 'S' shape to 'J' shape by increasing aluminium thickness prepared using low evaporation rates. The results indicated that the S-shaped J-V curve arises from charge trapping due to the presence of highly oxidised aluminium at the active-layer/cathode interface. The new back-to-back diode model was used for modelling this feature. An overview of effects that lead to the S-shape deviation in OSCs' J-V curve can be found in [14].

In the summery, the appearance of S-kink in J-V characteristics of OSCs was so far attributed to many different physical effects such as formation of charge dipole, defects, and traps at interfaces [6], the presence of injection and extraction transport barriers [13-15], the imbalanced mobilities [11, 16], reduced surface recombination [10, 18, 21], vertical phase segregation [20, 23] and oxygen doping [22].

Chapter 4

The Surface Recombination and the Thermal Injection Influences on the J-V Characteristics of Organic Solar Cells

4 The surface recombination and thermal injection influences on J-V characteristics of organic solar cells.

The significance of the impact of surface processes on the performance of OSCs was perceived in the previous section through the systematization of research results available in the literature. Original investigation results on this topic achieved by the author are presented in this chapter. The greatest attention is paid to the analysis of the surface recombination of both majority and minority charge carriers and the impact of the injection barrier heights for majority carriers on the OSCs' contacts on the J-V characteristics. The investigation was conducted by the usage of DDM and comparison of simulation results with measured J-V curves for ITO/(poly(3,4-ethilenedioxythiophene):poly(styrenesulfonate)) PEDOT:PSS/ (poly(3-hexylthiophene)) P3HT: (1-(3-methoxycarbonyl) propyl-1-phenyl-[6, 6]-methanofullerene) PCBM/Al and ITO/PEDOT:PSS/P3HT: (indene-C60 bisadduct) ICBA/Al solar cells.

4.1 Experimental details

Device fabrication

The ITO/PEDOT:PSS/P3HT:PCBM/Al and ITO/PEDOT:PSS/P3HT:ICBA/Al devices were fabricated and tested at the Institute for Micromanufacturing of Louisiana Tech University. The fabrication details for ITO/PEDOT:PSS/P3HT:PCBM/Al solar cell are given in Table 4.1 and for ITO/PEDOT:PSS/P3HT:ICBA/Al device are given in Table 5.2. Also, the top schematic of the substrate and the device cross-section of P3HT:PCBM based solar cells are given in Fig. 4.1.1 and for P3HT:ICBA based solar cells is given in Fig. 4.1.2.

Table 4.1 *The fabrication parameters of* ITO/PEDOT:PSS/P3HT:PCBM/Al *solar cell*

Parameter	Value
Solvent	Chlorobenzene
P3HT	12mg/mL
PCBM	50% wt
Additive (OT)	0% vol
Spin Coating Recipe	1000 RPM, 50s
Thickness	130nm (Profilometer)
PEDOT:PSS	Low Conductivity, 4000 RPM, 30s
Aluminium	100nm, 0.4nm/s, 1μTorr
Annealing	150°C, 15min, (Post-production)

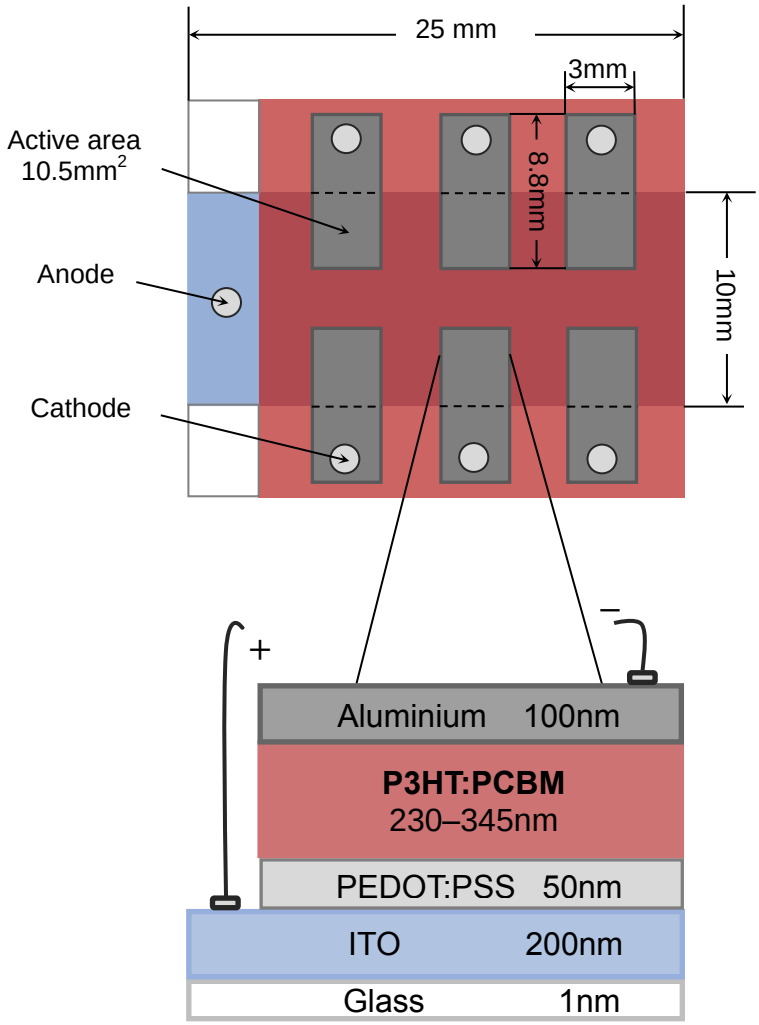

Fig. 4.1.1 P3HT:PCBM *based solar cell, the top schematic of substrate and device schematic*.

Table 4.2 *The fabrication parameters of* ITO/PEDOT:PSS/P3HT:ICBA/Al *solar cell*

Parameter	Value
Solvent	Chlorobenzene
P3HT	12mg/mL
ICBA	50% wt
Additive (OT)	0% vol
Spin Coating Recipe	900 RPM
Thickness	130.2nm (Profilometer)
PEDOT:PSS	3000 RPM, 30s (Thickness: 30nm)
Aluminium	100nm, 0.5nm/s, 1μTorr
Annealing	150°C, 15min (Post-production)

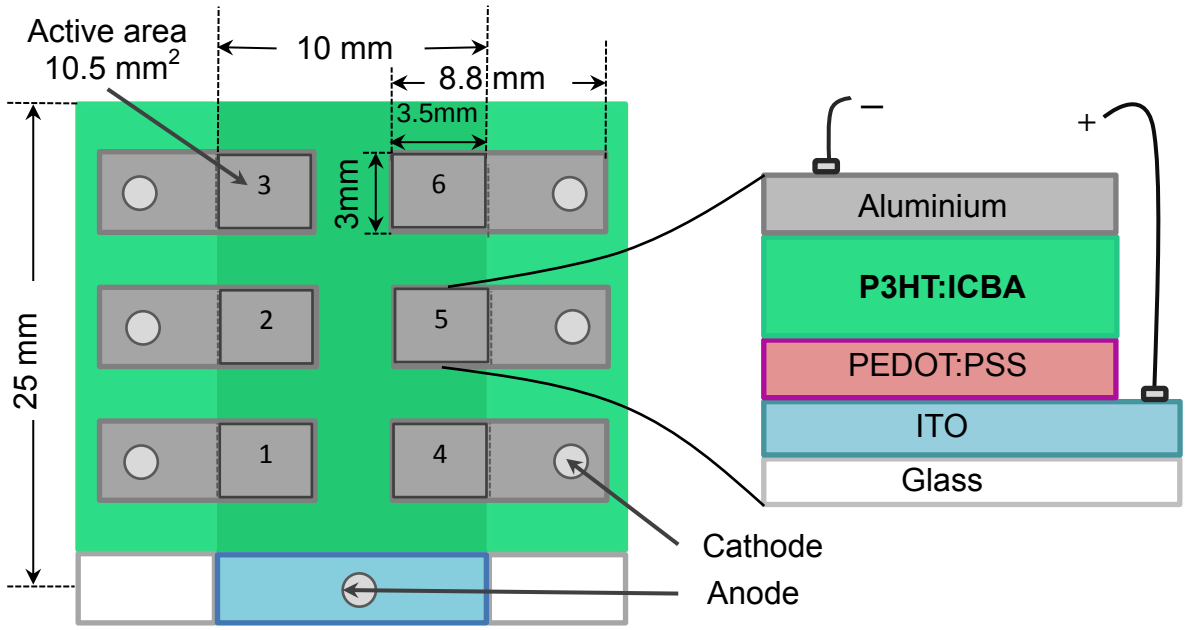

Fig. 4.1.2. P3HT:ICBA *based solar cell, the top schematic of substrate and device schematic*.

Device characterization

The characterization of devices was done by illuminating them with AM1.5 solar spectrum of 100mW/cm^2 optical power density from the Spectra-Physics 66900 solar simulator and by measuring J-V characteristics using Keithley 2400 source meter.

Optical testing

Optical testing of P3HT:PCBM and P3HT:ICBA films on quartz substrates were also conducted by measuring reflected and transmitted spectra for each film from which corresponding extinction coefficients (κ) and refractive indexes (n) were determined by FILMeasure software. In Fig. 4.1.3. the κ and n spectral dependence for 130nm thick P3HT:PCBM film are shown. The same optical parameters for 130nm thick P3HT:ICBA film are depicted in Fig. 4.1.4.

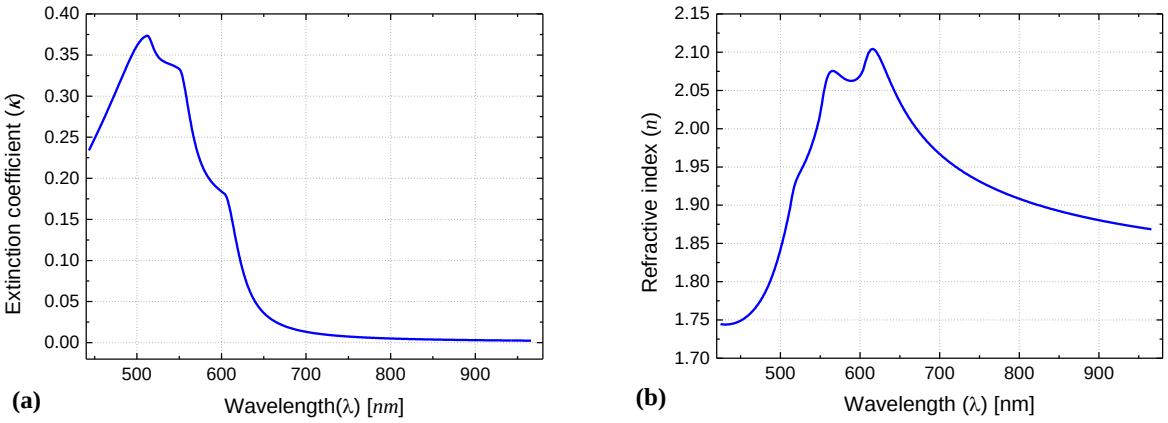

Fig. 4.1.3. *The spectral dependence for* P3HT:PCBM *film of thickness* 130*nm of both* (a) *extinction coefficients* (*κ*) *and* (b) *refractive indexes* (*n*).

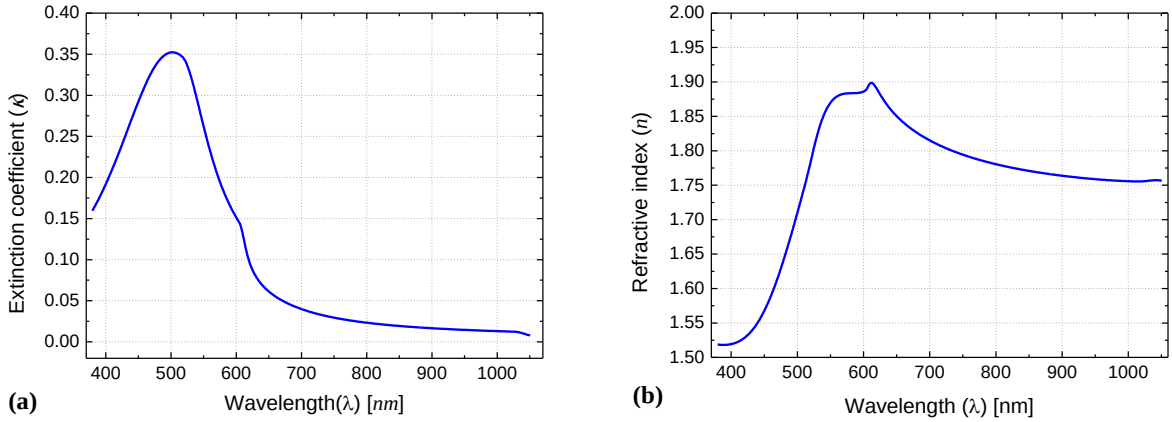

Fig. 4.1.4. *The spectral dependence for* P3HT:ICBA *film of thickness* 130*nm of both* (a) *extinction coefficients* (*κ*) *and* (b) *refractive indexes* (*n*).

4.2 The impact of the surface recombination on the OSCs' J-V characteristics

The surface recombination plays an important role in determining the OSCs' performance and has a great impact on their efficiency. In this section isolated influence of the surface recombination on the OSCs' J-V curve by using DDM is analysed. The DDM used in the simulation was explained in section 3.3 with an optical generation profile given by equation 3.3.23, Langevin recombination defined in equation 2.2.4, constant mobilities for electrons and holes. The boundary conditions are specified in equations 3.3.27 and 3.3.28. Finite difference discretization including Scharfetter and Gummel approach and Newton's method are used for numerical solving. The approach applied for solving the system of equations 3.3.1–3.3.5 to derive the electrical potential profile as well as the electron and hole concentration profiles in the solar cell photoactive layer, which are then used for calculating the J-V characteristics, is described in appendix A. The corresponding Matlab code is given in appendix B.

The parameters for ITO/PEDOT:PSS/P3HT:PCBM/Al and ITO/PEDOT:PSS/P3HT: ICBA/Al solar cells are presented in Table 4.3. The device parameters used in simulations in this chapter belong to the P3HT:ICBA based solar cell.

Table 4.3 *The parameters for* ITO/PEDOT:PSS/P3HT:PCBM/Al *and* ITO/PEDOT:PSS/P3HT:ICBA/Al *solar cells*

Symbol	Quantity	P3HT:PCBM	P3HT:ICBA	Reference
d	Active layer thickness [nm]	130		[121]
T	Absolute temperature [K]	293		[121]
ε_r	Relative permittivity	3.4		[39]
E_g	Energy gap [eV]	1.4		[122]
N_C,N_V	The effective density of states [m^{-3}]	1×10^{26}		[39]
V_{bi}	Built-in voltage [V]	0.62		[90]
			0.8	[121]
η_i	Internal quantum efficiency	0.62	1.0	*
μ_p	Hole mobility $[cm^2/(V\cdot s)]$	3×10^{-4}		[88]
			2.08×10^{-5}	[123]
μ_n	Electron mobility $[cm^2/(V\cdot s)]$	2.5×10^{-3}		[88]
			4.92×10^{-4}	[90], [124]
τ_n	Electron lifetime [s]	1×10^{-4}		[90]
			6.2×10^{-5}	[125]
τ_p	Hole lifetime [s]	1×10^{-7}		[90]
			3×10^{-7}	[126]

***** *From least square fit to experimental data*

At the beginning of the analysis to investigate only the effect of SRVs on the J-V curves, the equilibrium thermionic concentrations for electrons and holes on both anode and cathode are taken to be zero $(n_{th}^{a(c)} = p_{th}^{a(c)} = 0)$. So the boundary conditions are reduced to:

$$J_n(x=0) = \pm q\, n(x=0)\, S_n^a, \qquad J_p(x=0) = \pm q\, p(x=0)\, S_p^a, \qquad (4.1)$$

$$J_n(x=d) = \pm q\, n(x=d)\, S_n^c, \qquad J_p(x=d) = \pm q\, p(x=d)\, S_p^c. \qquad (4.2)$$

The assumption that the diffusion current is dominant in equations 3.3.4 and 3.3.5 [127] implies the choice of +/– signs at the right hand side of equations 4.1 and 4.2. The boundary conditions are transformed to:

$$J_n(x=0) = q\, n(x=0)\, S_n^a, \qquad J_p(x=0) = -q\, p(x=0)\, S_p^a, \qquad (4.3)$$

$$J_n(x=d) = -q\, n(x=d)\, S_n^c, \qquad J_p(x=d) = q\, p(x=d)\, S_p^c. \qquad (4.4)$$

The values of SRVs can be changed from zero to infinity. It is a difficult and pretty exhausting task to analyse the simulation results obtained by varying the four SRV parameters in such a wide range. However, changing the $S_n^a, S_n^c, S_p^a,$ and S_p^c within a specified range provides very good insight into their influence on the OSCs' J-V curve. The possible way to classify the SRVs values can be found in the literature [18]. It is explained that when the SRV value is much larger than the effective transport velocity (v_E) of charge carriers at the specific contact [18], the contact is acting as the conductive one. On the other side, if the SRV value is much lower than v_E, the contact has a blocking character. Certainly, if the SRV has a value comparable to v_E, the contact is neither conductive nor blocking.

In order to systematize the simulation results, the SRV values are specified as shown in Fig. 4.2.1, the small S-value to represent the blocking contact, large L-value to define the conductive contact, and medium M-value for specifying the contact that is neither conducting nor blocking. Because the diffusion current is assumed to be dominant, the average diffusion velocity (v_d) is taken as the effective transport velocity of charge carriers at contacts. The average electron (hole) diffusion velocity is given by:

$$v_d^{n(p)} = \frac{L_{n(p)}}{\tau_{n(p)}}, \qquad (4.5)$$

where $L_{n(p)} = \sqrt{D_{n(p)}\, \tau_{n(p)}}, D_{n(p)} = V_t\, \mu_{n(p)}, V_t = k_B T/q$, $\tau_{n(p)}$ is the electron (hole) lifetime, $D_{n(p)}$ is the diffusion coefficient of electrons (holes), and V_t is the thermal voltage.

In these analysis three *S*-values are considered ($S = 0.1v_d, 0.01v_d, 0.002v_d$), one *M*-value ($M = v_d$), and three *L*-values ($L = 10v_d, 100v_d, 500v_d$).

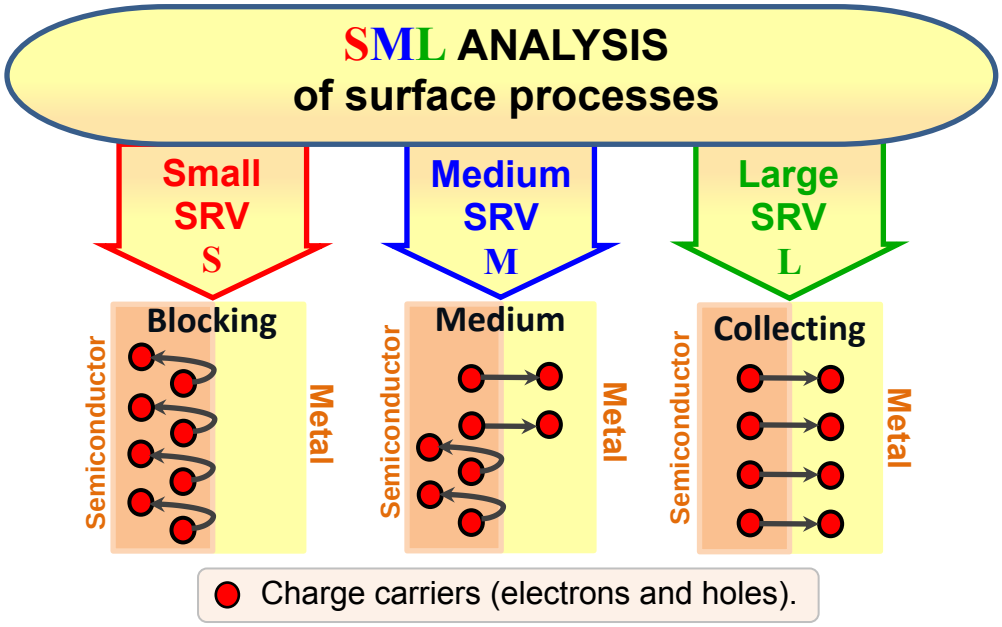

Fig. 4.2.1. *Schematic diagram assumption of the SML analysis* [128].

As the first step of the analysis, the measured J-V characteristics of ITO/PEDOT:PSS/P3HT:ICBA/Al OSCs is reproduced by the model. The J-V curve exhibits a slight S-shape deviation which is successfully simulated. This J-V curve serves as a reference for a further study and it is shown in Fig. 4.2.2 [129].

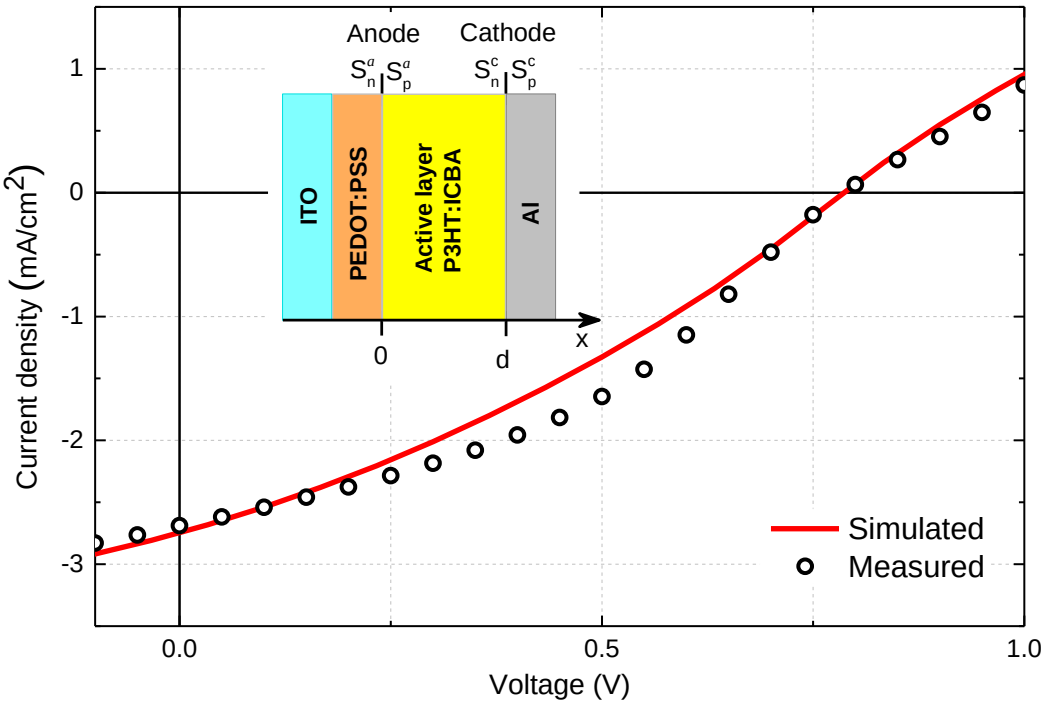

Fig. 4.2.2. *Measured* (circles) *and simulated* (full line) ITO/PEDOT:PSS/P3HT:ICBA/Al *solar cell* J-V *curves. The device cross section - Inset.*

The analysis was done for the case when the hole mobility is an order of magnitude less than the electron mobility $\mu_p << \mu_n$, the J-V curves with $S_n^a, S_n^c, S_p^a,$ and S_p^c taking *S*, *M*, and *L* values are then generated. The obtained results are systemized and graphically summarized in Figs. 4.2.3 and 4.3.4. It can be seen from Figs. 4.2.3 and 4.2.4 that the best OSCs' performance is achieved when all SRVs have *L*-value $(S_n^a = S_n^c = S_p^a = S_p^c = L)$ and exactly this simulated J-V curve gives the best fit to the measured data (reference experimental curve). It is turned out that the simulation results are almost the same for L=10 $v_d^{n(p)}$, L=100 $v_d^{n(p)}$, and L=500 $v_d^{n(p)}$. Since the calculated curves are indistinguishable, the graphs in Figs. 4.2.3 and 4.2.4 do not show the curves for L=100 $v_d^{n(p)}$ and L=500 $v_d^{n(p)}$. A conclusion can be made that 10 $v_d^{n(p)}$ is a sufficient SRV value for any contact in the device to behave as an ideally conductive. Both Fig. 4.2.3 and Fig. 4.2.4 are organized so that on each graph one SRV is changing its value from *S* to *L*, while others are constant and set to *L*-value. The results are different for different *S*-values, which implies that the lower limit from which the contact behaves as ideally blocking wasn't reached. It can be noticed from Fig. 4.2.3 and Fig. 4.2.4 that changing in the SRV values for electrons S_n^a and S_n^c have a greater impact on the J-V curve of OSCs than changing in the SRV values for holes S_p^a and S_p^c. Compared to the measured J-V characteristics of OSCs, it is obvious that lowering the S_p^a and S_n^c leads to an S-shape deviation in the fourth quadrant denoted as "S-shape down" which is shown in Fig. 4.2.3(a) and (b). On the other hand, lowering the values of S_n^a and S_p^c leads to an S-shape deviation in the first quadrant which are denoted as "S-shape up" which can be seen in Fig. 4.2.4(a) and (b).

The observed behaviour of J-V curves can be explained as follows. For positive bias voltages (V) lower than the V_{bi}, the resultant electric field in the device is inverse. This V-range corresponds to the fourth quadrant of J-V characteristics (solar cell operation regime) and a reverse electric current is flowing through the device. For good performance in this operation regime, it is important that the anode is conductive for holes (S_p^a=*L*) and the cathode is conductive for electrons (S_n^c=*L*). If this is satisfied, the J-V curve in the fourth quadrant will have a regular J-shape regardless of S_n^a and S_p^c values, as it can be seen in Fig. 4.2.3(a) and (b). When $V > V_{bi}$ the resultant electric field in the solar cell is forward, and forward current is flowing through the device. For regular operation in this V-range, which corresponds to the first quadrant of J-V characteristics, it is important that the anode is conductive for electrons (S_n^a=*L*) and the cathode is conductive for holes (S_p^c=*L*). The values of S_n^c and S_p^a are not relevant for this operation regime, which can, again, be confirmed by Fig. 4.2.4(a) and (b). Therefore, if one wants to have a J-V curve without an S-shape either down or up, it has to provide S_n^a=S_n^c=S_p^a=S_p^c=*L* on both contacts. In other words, contacts have to be conductive for both charge carrier types because the current is changing its direction during device operation.

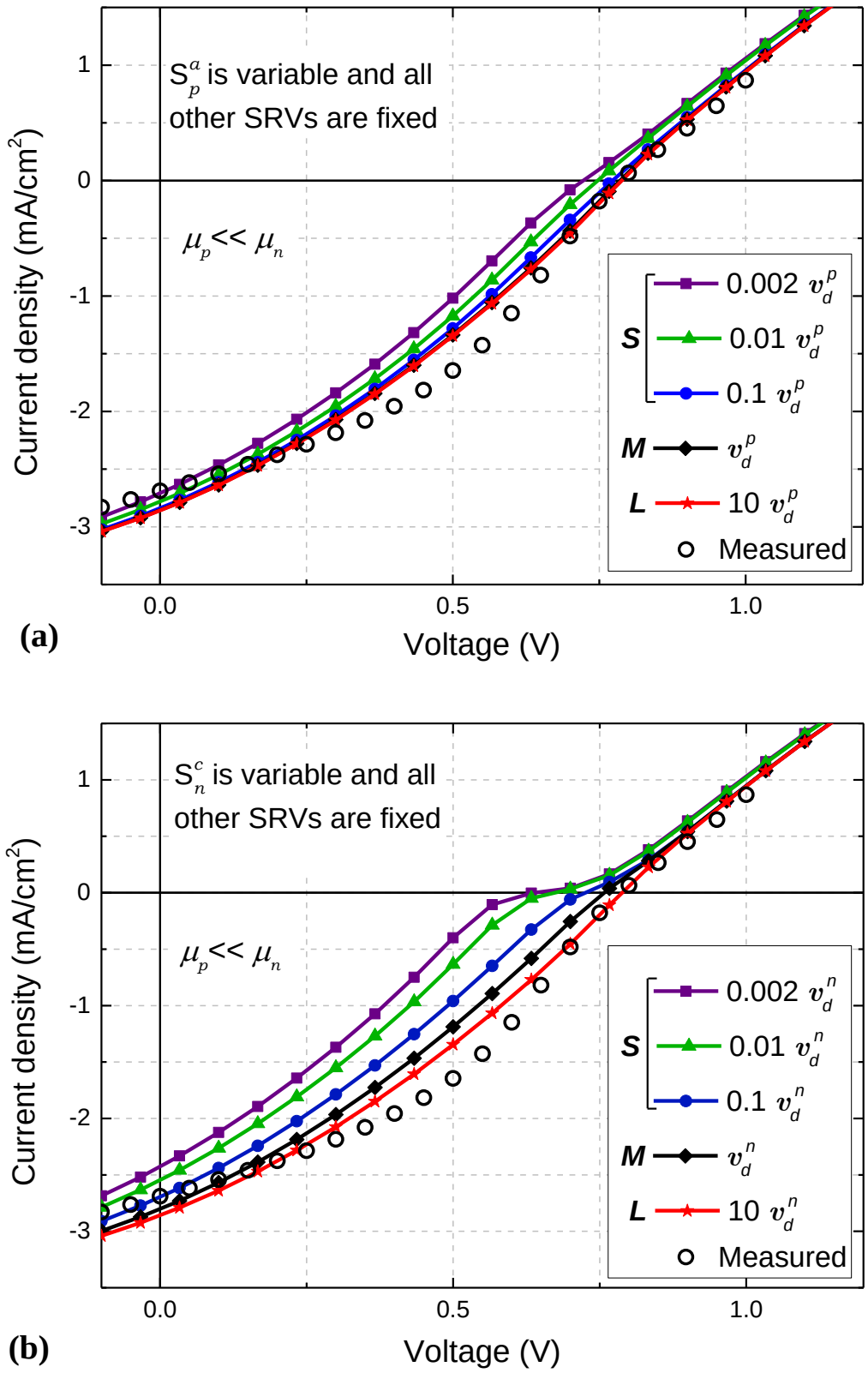

Fig. 4.2.3 The ITO/PEDOT:PSS/P3HT:ICBA/Al *solar cell* J-V *curves of measured* (open circles) *and simulated* (solids with marks) *for* $\mu_p << \mu_n$ *and different SRV values*. (a) S_p^a *is varied and* $S_n^a=S_n^c=S_p^c=L$, *and* (b) S_n^c *is varied and* $S_n^a=S_p^a=S_p^c=L$, [127].

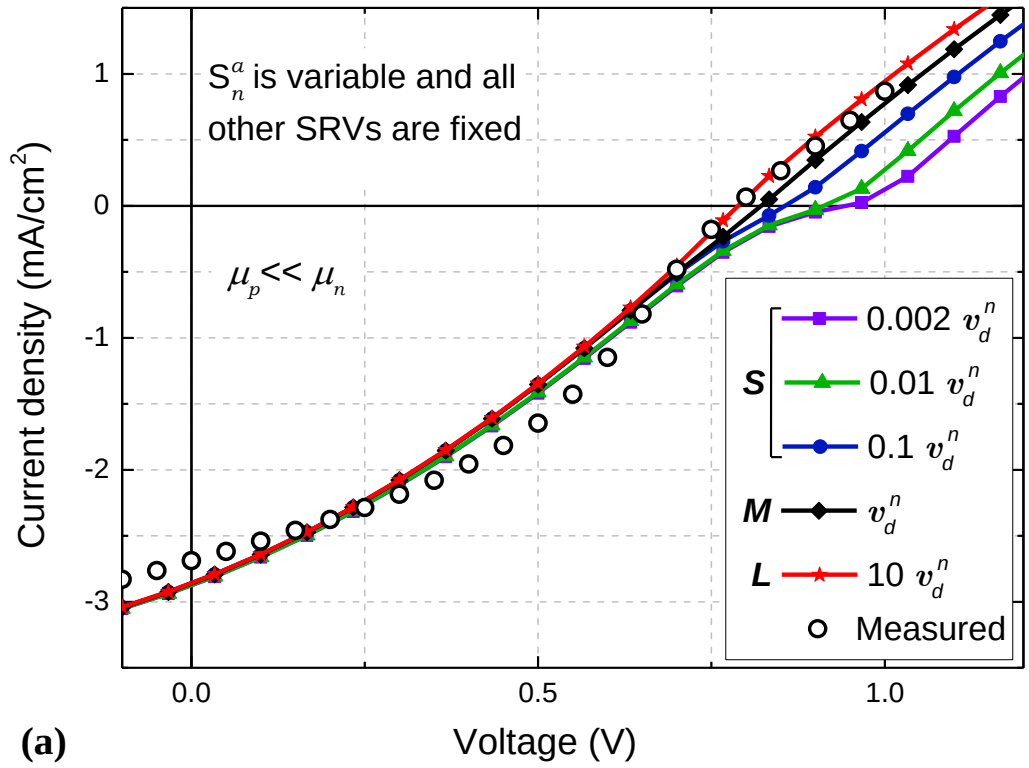

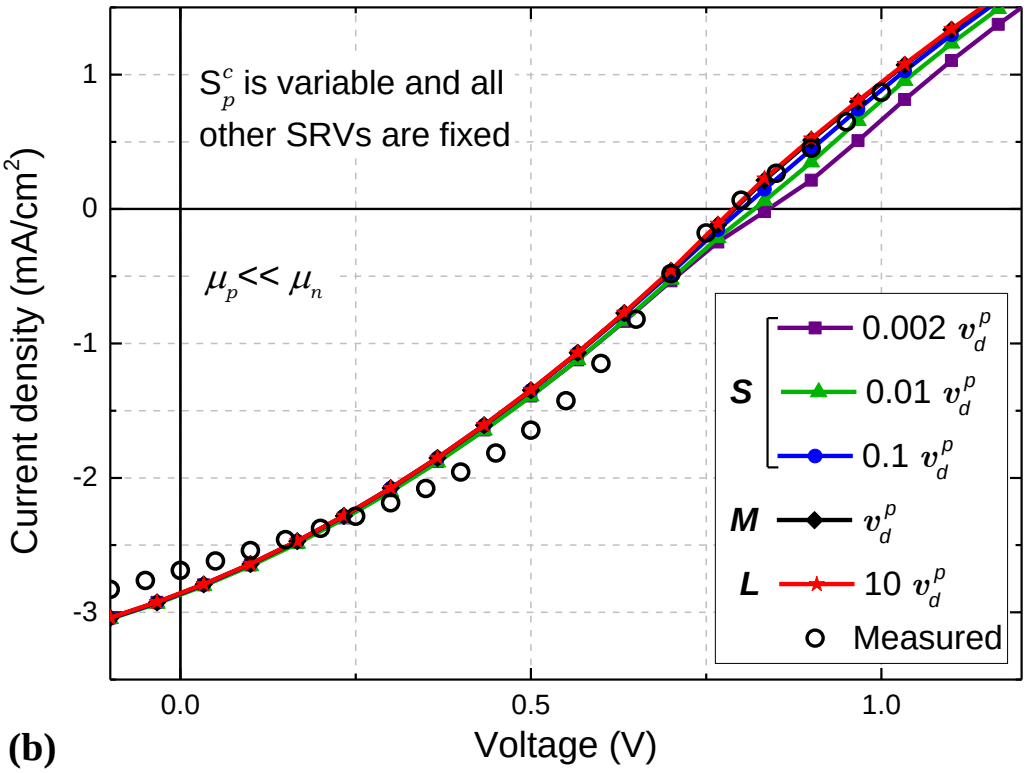

Fig. 4.2.4 The ITO/PEDOT:PSS/P3HT:ICBA/Al *solar cell* J-V *curves of measured* (open circles) *and simulated* (solids with marks) *for* $\mu_p << \mu_n$ *and different SRV values.* (a) S_n^a *is varied and* $S_n^c=S_p^a=S_p^c=L$, *and* (b) S_p^c *is varied and* $S_n^a=S_n^c=S_p^a=L$ [127].

The accumulation of charge carriers near the contacts was identified as one of the causes of the S-shape bending in the J-V characteristics of OSCs by many authors as outlined in chapter 4. In this study, the S-shape deviation in J-V characteristics calculated by the DDM can be also interpreted as a consequence of the charge accumulation. First, more attention will payed to the fourth quadrant of the J-V characteristics because it is the operating regime of the solar cell It is already explained that the J-V curve in this quadrant is governed by the S_p^a and S_n^c values. If anyone of these two SRVs has M or S value, it means that contacts are not ideally conductive for majority carriers and they accumulate each on their contact. Holes accumulate on the anode (when $S_p^a=M$ or S), and electrons accumulate on the cathode (when $S_n^c=M$ or S). This leads to a reduction in V_{bi} (Fig. 4.2.5, Inset), and consequently in the open-circuit voltage V_{oc}. The J-V curve in the fourth quadrant is shifted to the left and the S-shape down is produced (Fig. 4.2.5).

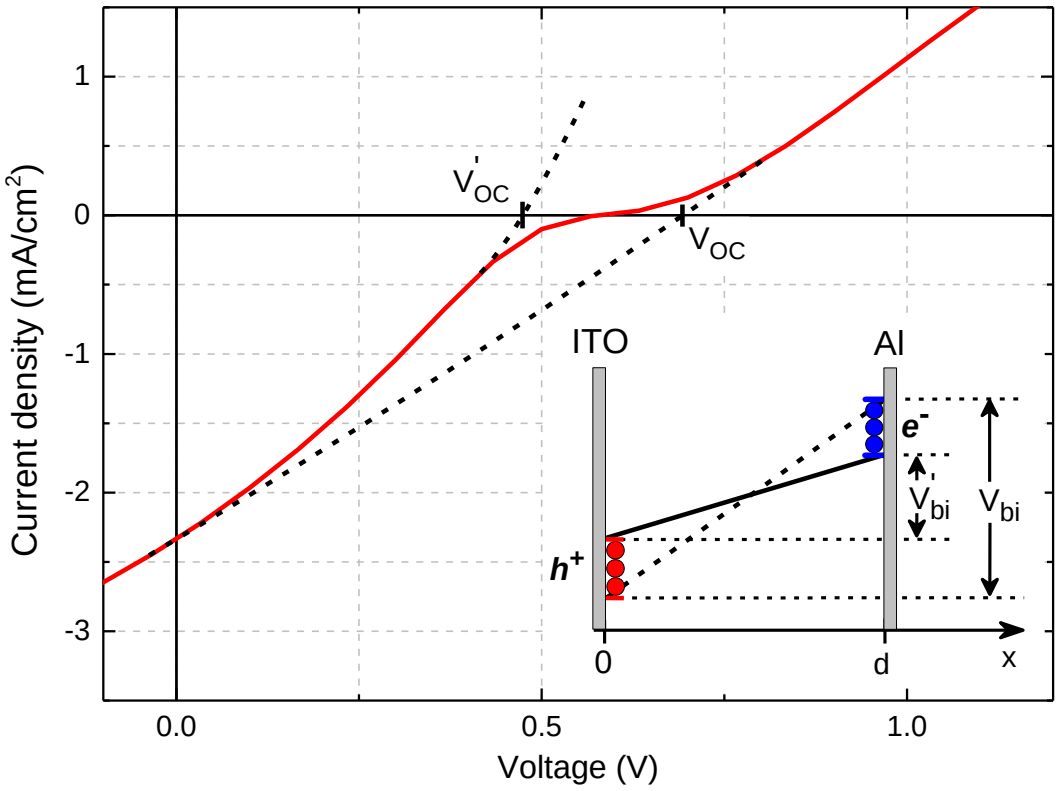

Fig. 4.2.5 *The simulated* ITO/PEDOT:PSS/P3HT:ICBA/Al *solar cell* J-V *curves, for* $S_p^a=S_n^c=S=0.002v_d^{n(p)}$ and $S_n^a=S_p^c=L$. *The accumulation of holes on the anode and electrons on the cathode inducing the reduction in* V_{bi} *is sketched in the inset* [127].

For bias voltages higher than the reduced V_{bi}, the current direction turns and contacts change their role. In this bias regime anode is collecting electrons and the cathode is collecting holes. When $S_n^a=S_p^c=L$ accumulated carriers are extracted by ideally conductive electrodes and in the first quadrant OSCs' J-V curve has the usual shape and position. Lowering the S_n^a and/or S_p^c to M or S

values leads to accumulation of electrons on anode and holes on the cathode. Consequently, the V_{bi} is increased (Fig. 4.2.6, Inset) and the upper part of the J-V curve is shifted to the right, leading to the formation of the S-shape up (Fig. 4.2.6).

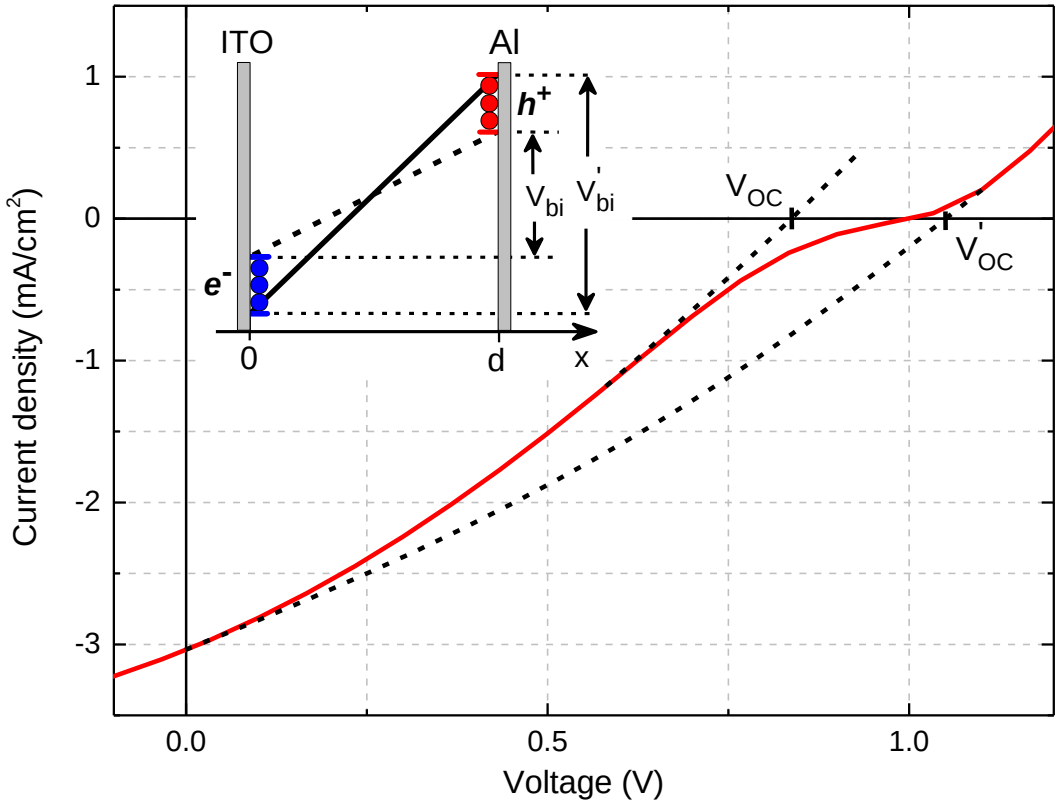

Fig. 4.2.6 *The simulated* ITO/PEDOT:PSS/P3HT:ICBA/Al *solar cell* J-V *curves, for* $S_n^a=S_p^c=S=0.002v_d^{n(p)}$ *and* $S_p^a=S_n^c=L$. *The accumulation of holes on the cathode and electrons on the anode inducing the increase in* V_{bi} *is sketched in the inset* [127].

The imbalanced charge transport in OSCs was also designated as a source of the S-shape deviation in J-V curves (see chapter 4). Since electron mobility is an order of magnitude higher than hole mobility in these calculations (Table 4.3) the analysis is repeated for the case when the mobility for electrons and holes are the same, and also for the case when the hole mobility is an order of magnitude higher than electron mobility. The simulated J-V curves obtained for $\mu_p=\mu_n$ are shown in Figs. 4.2.7 and 4.2.8, and $\mu_p >> \mu_n$ are shown in Figs. 4.2.9, and 4.2.10. Figs. 4.2.7, 4.2.8, 4.2.9, and 4.2.10 are organized the same as Figs. 4.2.3 and 4.2.4 only experimental J-V characteristic is omitted, and J-V curve calculated for $S_n^a=S_n^c=S_p^a=S_p^c=L$ is used as a reference instead. The results are similar to the previous ones except that the impact of the S_p^a and S_p^c is becoming more pronounced as the ratio of the hole to electron mobility μ_p/μ_n is increased.

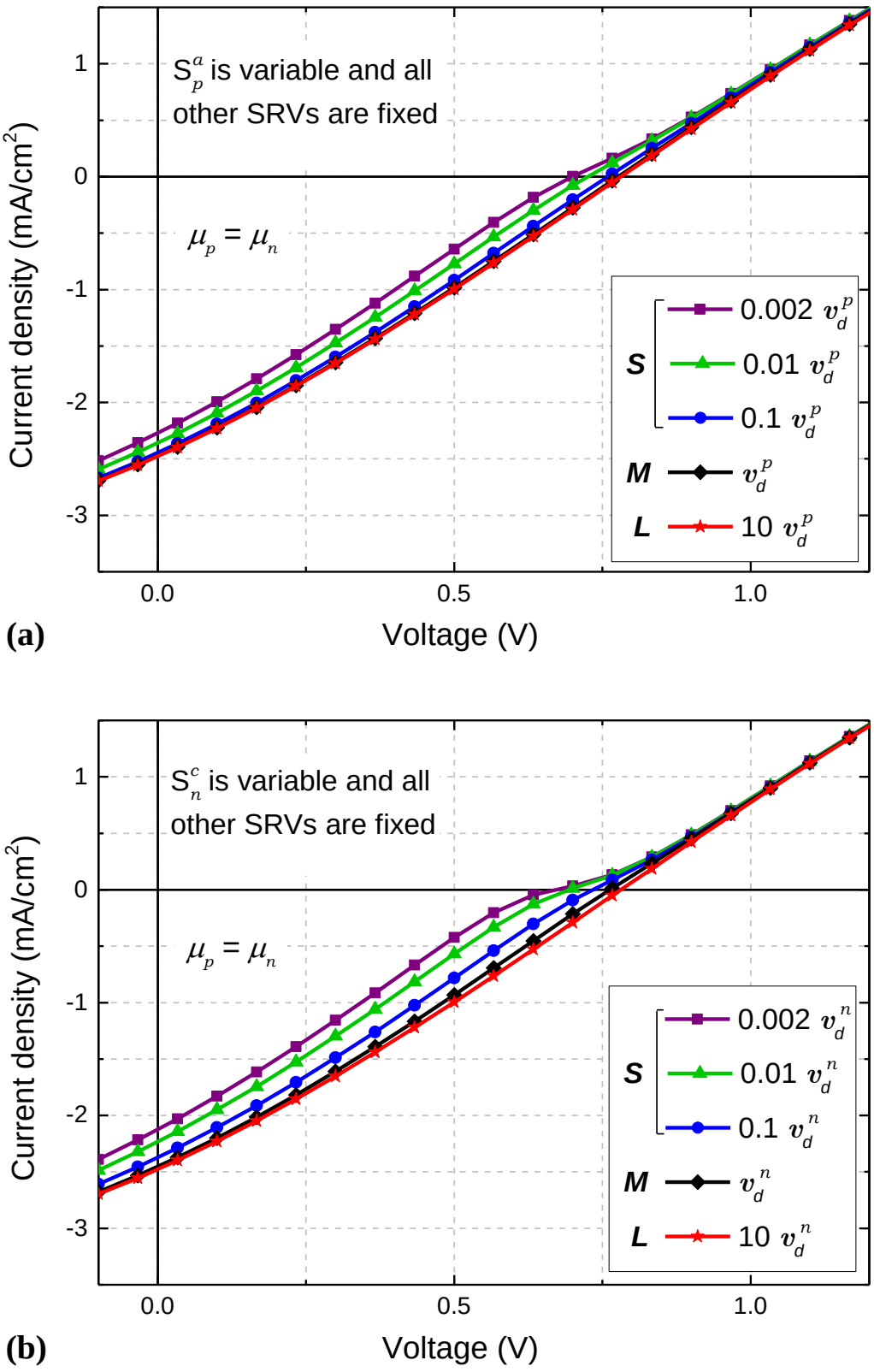

Fig. 4.2.7 *Simulated* ITO/PEDOT:PSS/P3HT:ICBA/Al *solar cell* J-V *curves, for* μ_p=μ_n=2.077×10^{-5} cm^2/(V·s) *and different* SRV *values* [127] (a) S_p^a *is varied and* S_n^a=S_n^c=S_p^c=L, *and* (b) S_n^c *is varied and* S_n^a=S_p^a=S_p^c=L.

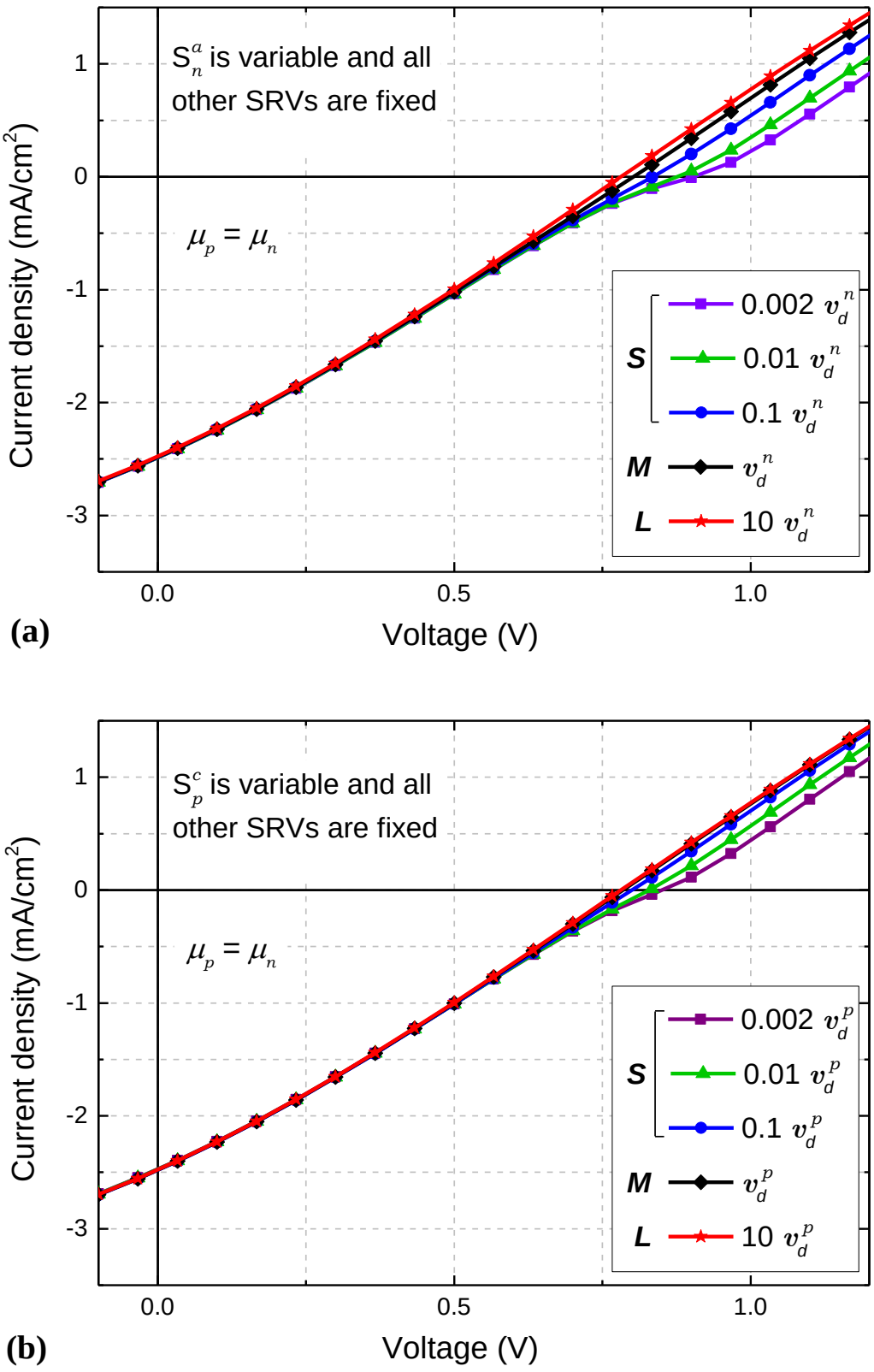

Fig. 4.2.8 *Simulated* ITO/PEDOT:PSS/P3HT:ICBA/Al *solar cell* J-V *curves, for* μ_p=μ_n=2.077×10^{-5} cm^2/(V·s) *and different* SRV *values.* [127] (a) S_n^a *is varied and* S_n^c=S_p^a=S_p^c=L, *and* (b) S_p^c *is varied and* S_n^a=S_n^c=S_p^a=L.

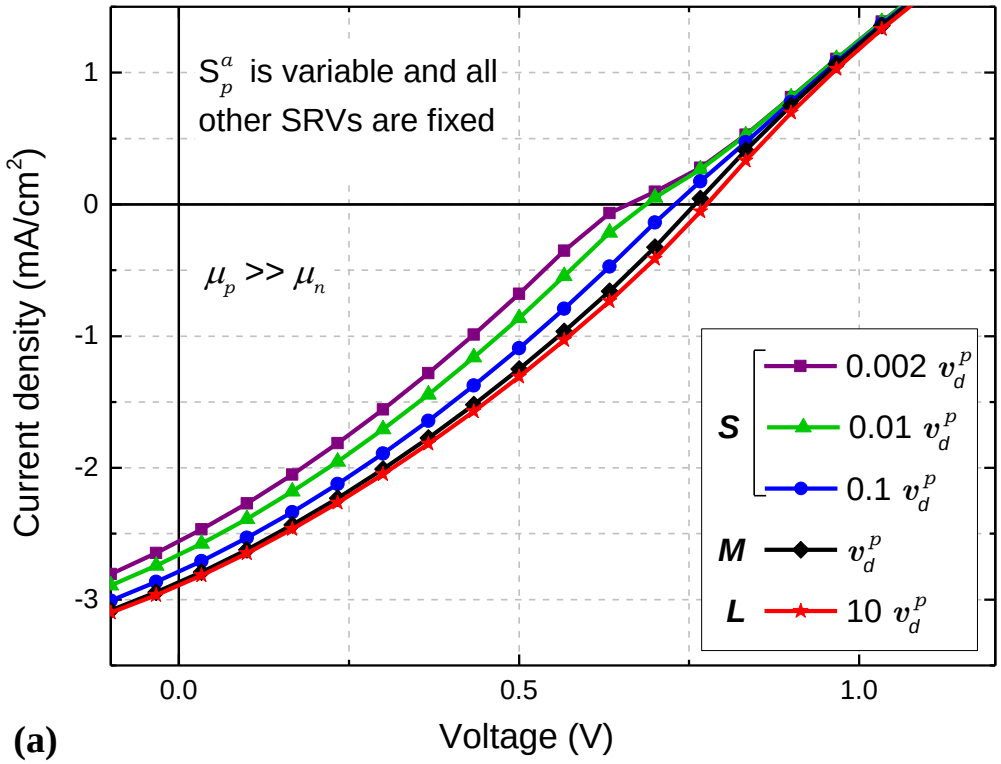

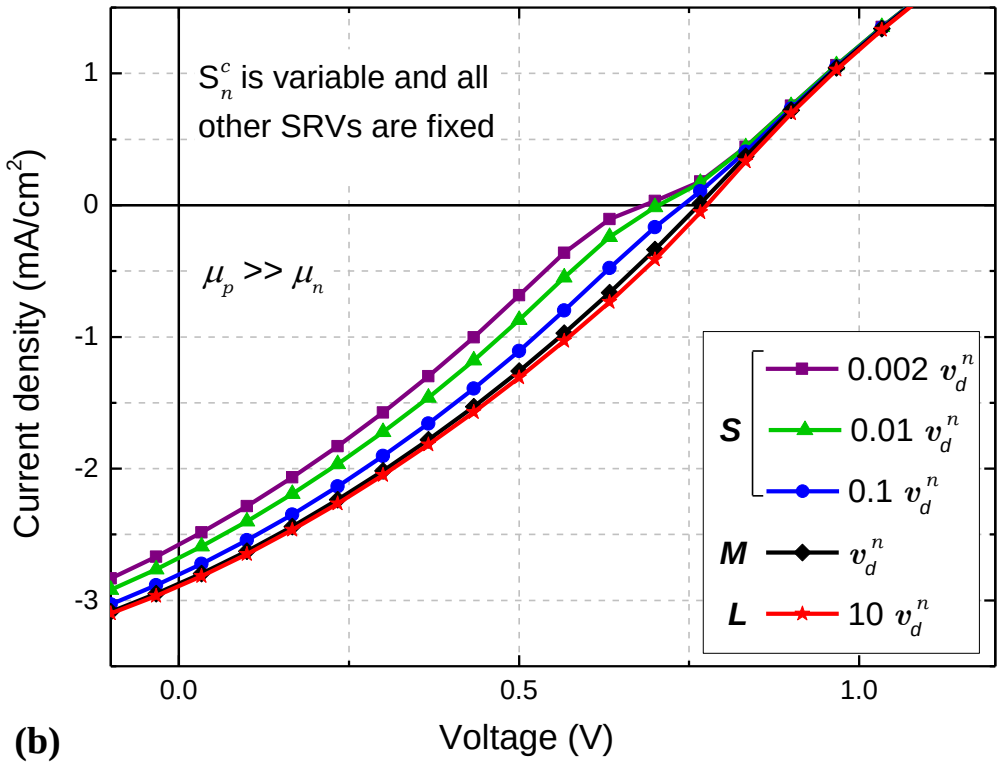

Fig. 4.2.9 *Simulated* ITO/PEDOT:PSS/P3HT:ICBA/Al *solar cell* J-V *curves, for* μ_p=4.92×10^{-4} cm^2/(V·s), μ_n=2.077×10^{-5} cm^2/(V·s) *and different* SRV *values* [127] (a) S_p^a *is varied and* S_n^a=S_n^c=S_p^c=L *and* (b) S_n^c *is varied and* S_n^a=S_p^a=S_p^c=L,

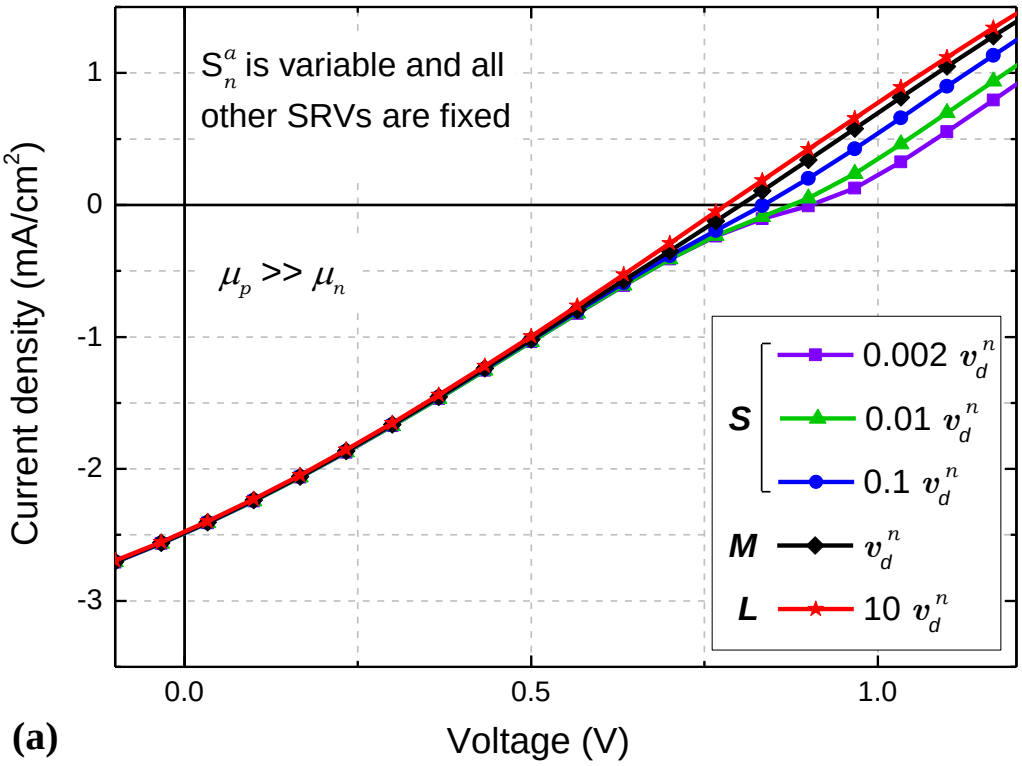

(a)

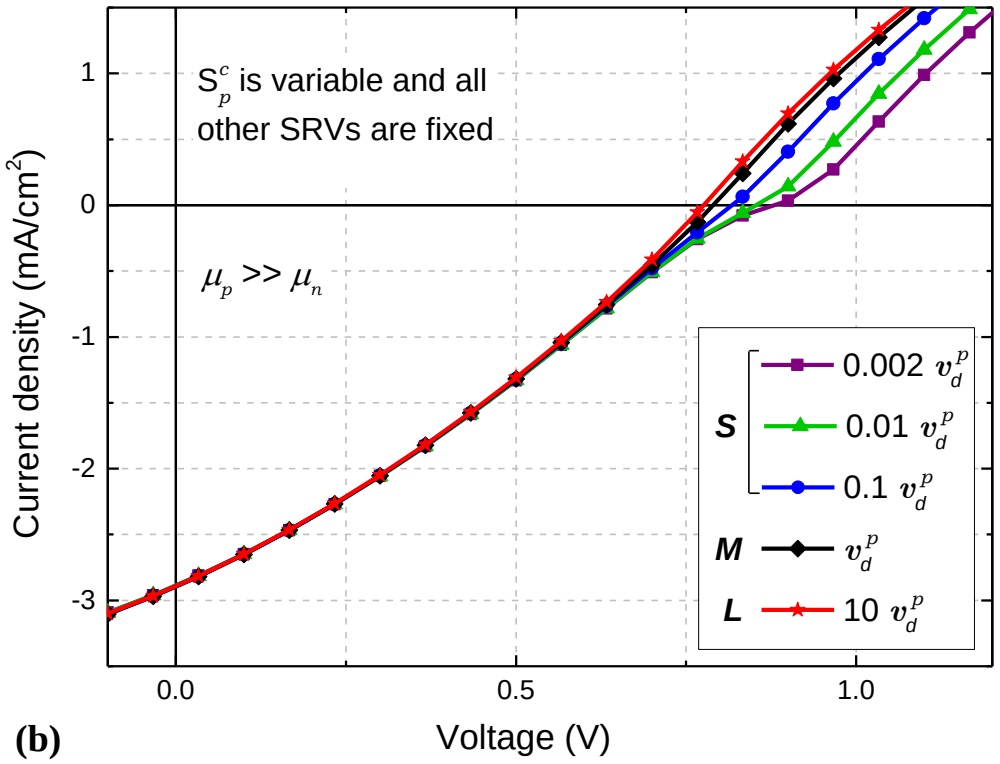

(b)

Fig. 4.2.10 *Simulated* ITO/PEDOT:PSS/P3HT:ICBA/Al *solar cell* J-V *curves, for* μ_p=4.92×10^{-4} cm^2/(V·s), μ_n=2.077×10^{-5} cm^2/(V·s) *and different* SRV *values* [127] (a) S_n^a *is varied and* S_n^c=S_p^a=S_p^c=L *and* (b) S_p^c *is varied and* S_n^c=S_n^c=S_p^a=L.

The analyses so far were focused on the case when the value of only one SRV is reduced (having M or S-value) and the other SRVs have L-value. It should be emphasized that the S-shape bending in the J-V curve becomes more and more pronounced by increasing the number of SRVs that are reduced which is shown in Fig. 4.2.11.

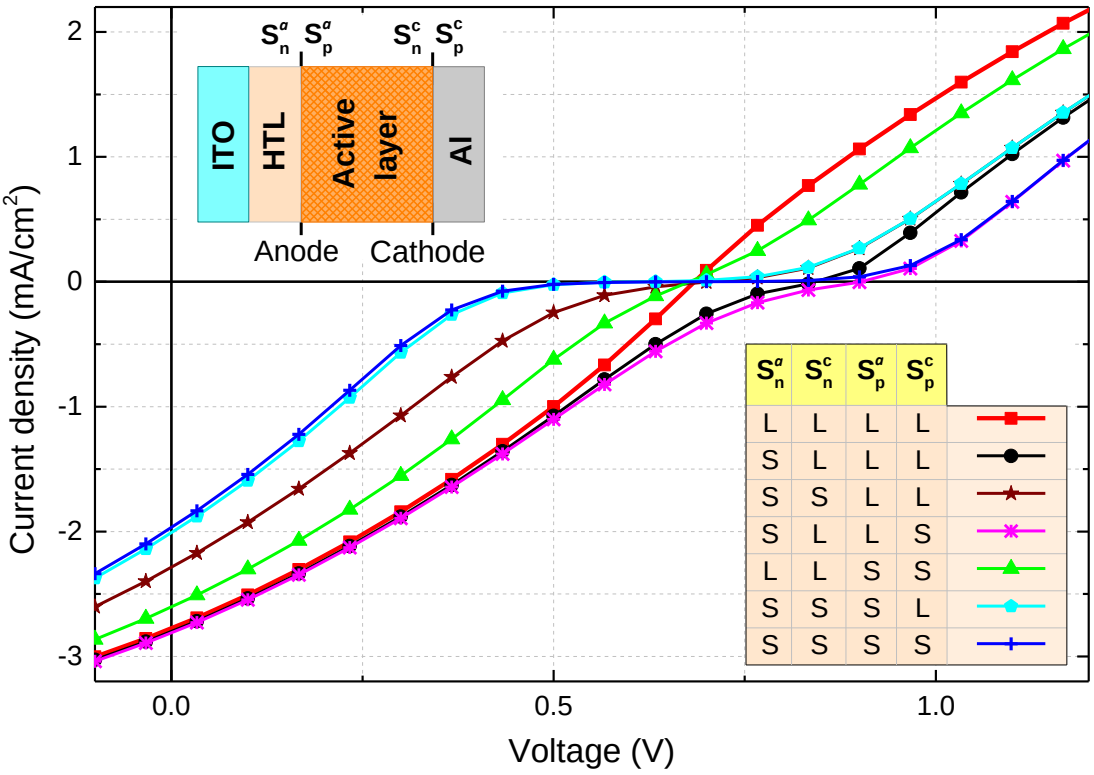

Fig. 4.2.11 *The simulated* OSCs' J-V *characteristics for 7–different combinations Of the* SRVs *values, and device cross-section – Inset* [129].

4.3 The impact of the injection barrier heights for majority carriers on the J-V characteristics of OSCs.

After perceiving the separate effect of surface recombination on the J-V curve of OSCs in the previous section, where the conclusion is that the regular OSCs' operation occurs when the $S_n^a=S_n^c=S_p^a=S_p^c=L$, the analyses can be continued by including thermal injection in the DDM calculations. The thermal injection on electrodes is taken into account through the boundary conditions which then have the form:

$$J_n(0) = q\,S_n^a\left(n(0)-n_{th}^a\right), \qquad J_p(0) = -q\,S_p^a\left(p(0)-p_{th}^a\right), \tag{4.6}$$

$$J_n(d) = -q\,S_n^c\left(n(d)-n_{th}^c\right), \qquad J_p(d) = q\,S_p^c\left(p(d)-p_{th}^c\right). \tag{4.7}$$

where the density of thermally injected charge carriers on the anode n_{th}^a, p_{th}^a, and the cathode n_{th}^c and p_{th}^c are defined in section 2.2 by the equations 2.2.10–2.2.13.

As it was explained in section 2.2, the Φ_{Bp} is the injection barrier height for holes as majority carriers on the anode and the Φ_{Bp} is the injection barrier height for electrons as majority carriers on the cathode. To analyse the impact of injection barrier heights for majority carriers on OSCs' J-V curve as the first step the Φ_{Bn} is set to zero and the Φ_{Bp} is changed in the range from 0eV to 1eV with a step of 0.1eV. The calculated J-V curves, by taking the parameters of P3HT:ICBA based solar cell from Table 4.3, are shown in Fig. 4.3.1. It can be deduced from Fig. 4.3.1 that the Φ_{Bp} value strongly affects the V_{oc} of OSCs but it doesn't introduce the S-shape. Also, changing the value of Φ_{Bp} above 0.7eV has no effect on the J-V curve. As the second step, the Φ_{Bp} is set to zero and the Φ_{Bn} is changed over the same range (0–1eV), again with the step of 0.1eV. The results are shown in Fig. 4.3.2. The V_{oc} is strongly affected by the Φ_{Bn} until it reaches the value of 0.3eV, above which, further change has no impact on V_{oc}. When Φ_{Bn} is larger than 0.2eV, the J-V characteristic exhibits the S-shape. It is important to notice that the S-shape which arises from the existence of a significant injection barrier for electrons on the cathode is different compared to S-shape bending caused by surface recombination (see Fig. 4.3.2). The S-shape which is the consequence of the high electron injection barrier on the cathode makes the S-kink at the point where it intersects the voltage axes after which it proceeds to grow monotonically, and it has only one saddle point. This type of the S-shaped J-V characteristic is less often found in the literature [15], [114]. On the other hand, the S-shape in the J-V characteristics of OSCs which originates from the surface recombination manifests the S-bending in the vicinity of the voltage axis, after which it rises almost exponentially making two saddle points. The S-shaped J-V curves produced by SRVs reduction calculated by this model are depicted in Fig. 4.2.11.

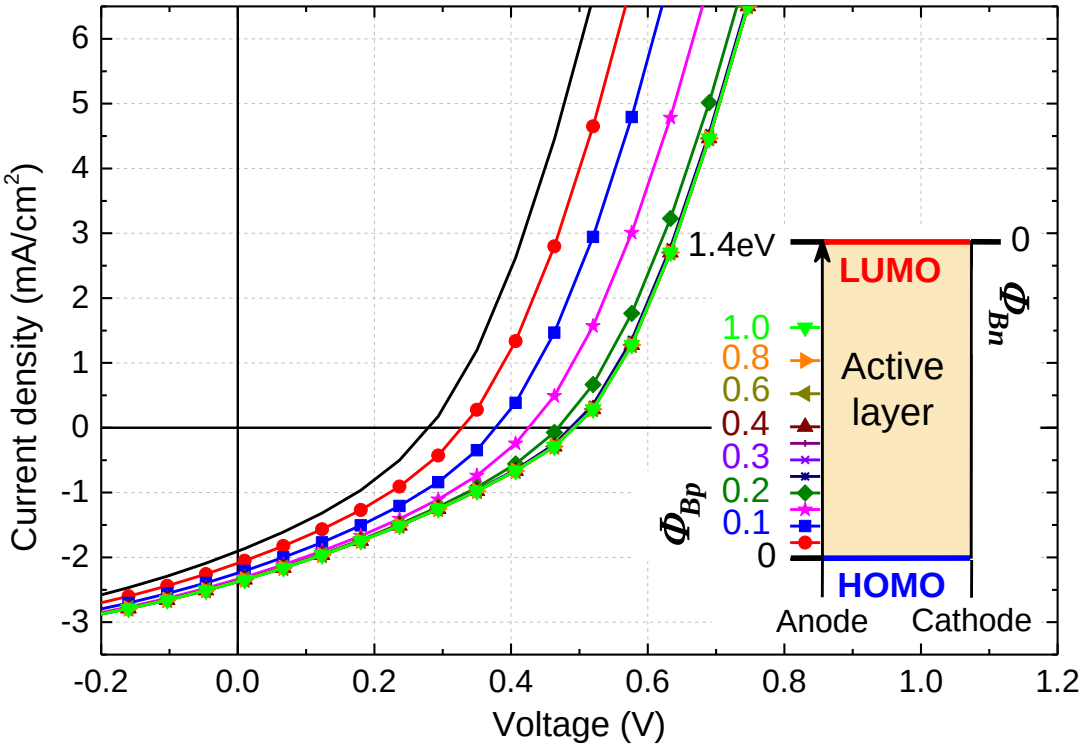

Fig. 4.3.1 *Simulated* J-V *characteristics for different values of* Φ_{Bp} *in the absence of* Φ_{Bn}, *The energy diagrams with different values of* Φ_{Bp} *are depicted in the inset* [129]. P3HT:ICBA *based solar cell parameters are used in the calculation (Table 5.3).*

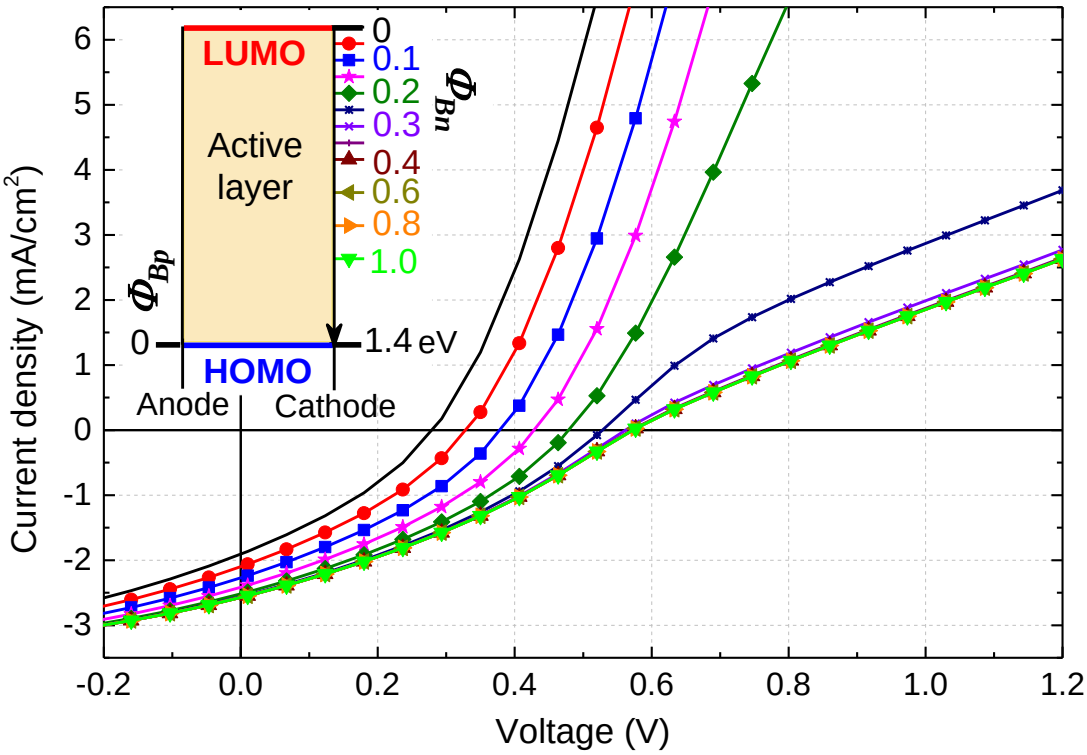

Fig. 4.3.2 *Simulated* J-V *characteristics for different values of* Φ_{Bn} *in the absence of* Φ_{Bp}. *The energy diagrams with different values of* Φ_{Bn} *are depicted in the inset* [129]. P3HT:ICBA *based solar cell parameters are used in the calculation (Table 5.3).*

4.4 Validation of the model

The model is verified by the comparison between the simulated and the measured J-V characteristics for ITO/PEDOT:PSS/P3HT:PCBM/Al and ITO/PEDOT:PSS/P3HT:ICBA/Al solar cells. The device parameters of solar cells are given in Table 4.3. For the P3HT:PCBM based OSCs a regular J–shaped J-V curve was measured and it is reproduced very well by the model, as shown in Fig. 4.4.1. The simulated curve is obtained by taking all SRVs to have L-value and the injection barrier heights for electrons and holes to be Φ_{Bn}=0.25eV and Φ_{Bp}=0.6eV, respectively. The obtained J-V curve is at the limit of S-shaping. Here it should be mentioned that the critical height of Φ_{Bn} after which OSCs' J-V curve exhibit S-bending depends strongly on parameter values especially $\mu_{n(p)}$, $N_{C(V)}$. On the other hand, for the P3HT:ICBA based OSCs, a malformed S-shaped J-V curve was recorded. the S-shaped J-V characteristics have modelled and a good agreement with the experiment is accomplished, as it is depicted in Fig. 4.4.2. Again, all SRV values in the calculation are taken to be L, and Φ_{Bn}=0.7eV and Φ_{Bp}=0.6eV are applied. It can be concluded that the S-shape bending in the measured J-V curve is the consequence of the electron injection barrier higher than 0.2eV, rather than the reduction of SRVs values on electrodes.

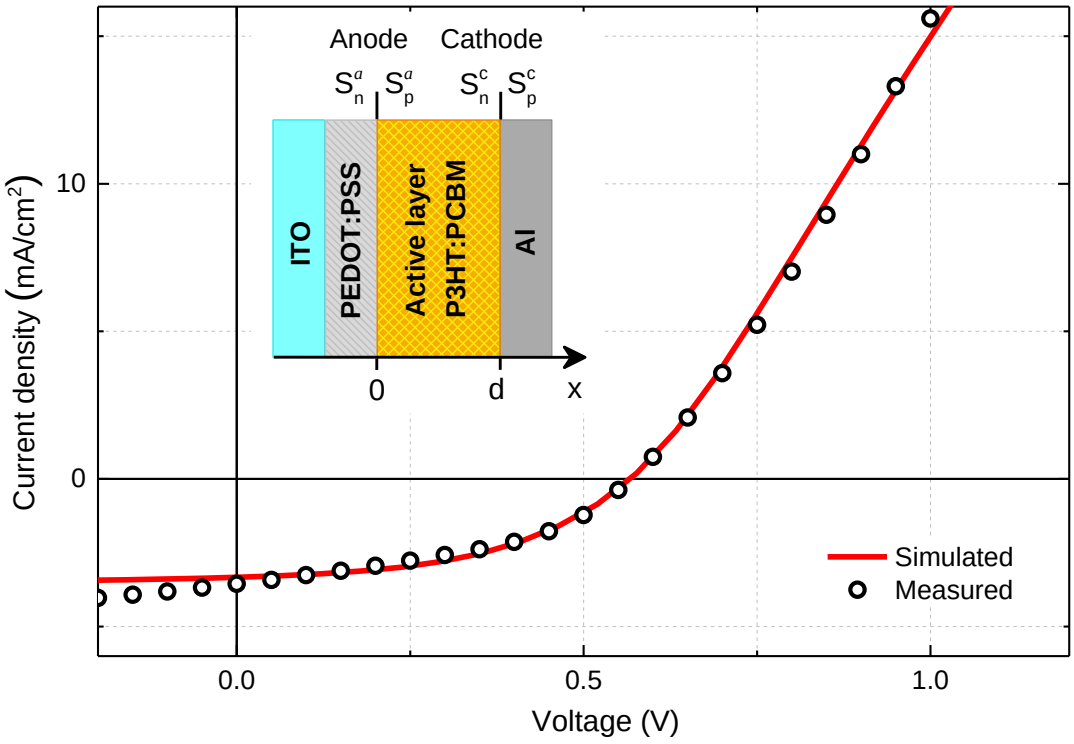

Fig. 4.4.1 *A comparison between the simulated and measured* J-V *characteristics of* ITO/PEDOT:PSS/P3HT:PCBM/Al OSCs *with* Φ_{Bn}=0.25eV *and* Φ_{Bp}=0.6eV, *and* $S_n^a=S_p^a=S_n^c=S_p^c=L$. *The device cross-sections is given in the inset.*

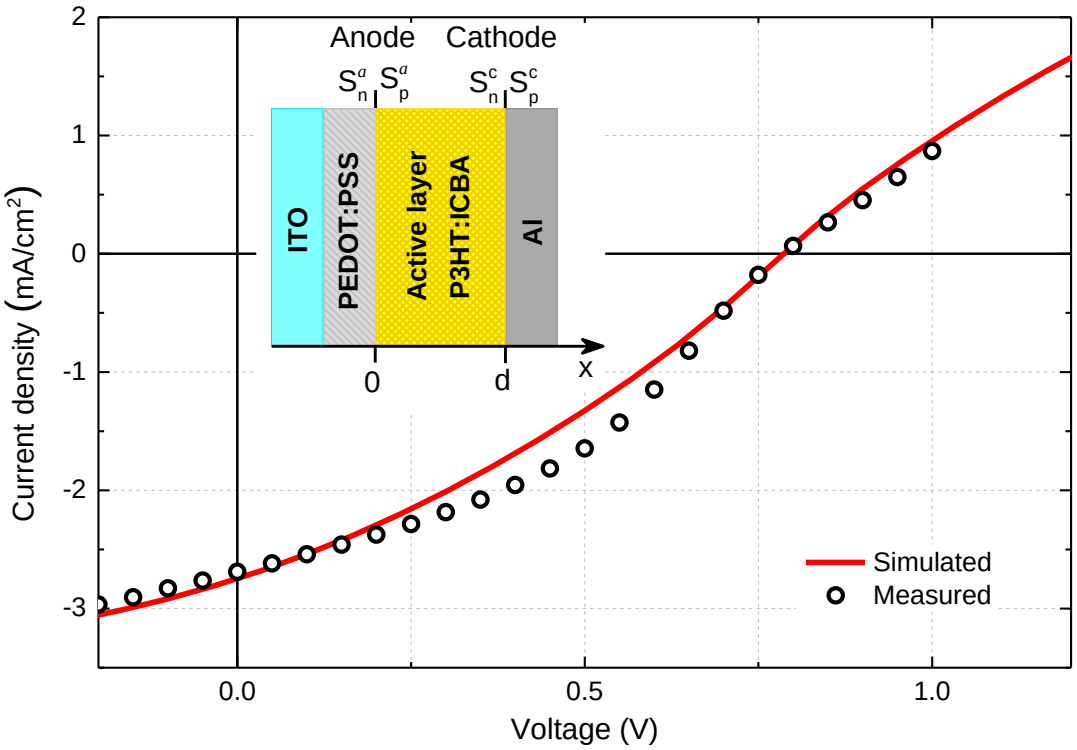

Fig. 4.4.2 *A comparison between the simulated and measured* J-V *characteristics of* ITO/PEDOT:PSS/P3HT:ICBA/Al OSCs *with* Φ_{Bn}=0.7eV *and* Φ_{Bp}=0.6eV. *and* $S_n^a=S_p^a=S_n^c=S_p^c=L$. *The device cross-sections is given in the inset.*

4.5 Selective contacts

Selective contacts are of great importance for the performance of OSCs [130]. Their primary role is to conduct the majority carriers and to block the minority carriers. In solar cells, the ideal contact selectivity is provided when only electrons are conducted by the cathode and only holes by the anode. The crucial question is how the selectivity of the contacts is realized in OSCs and how it can be modeled. The basic method to accomplish contact selectivity is to make a region with selective conductivity near the electrode [131]. In OSCs and perovskite solar cells, it is usually done by inserting a hole transporting layer near the anode and an electron transporting layer near the cathode [130], [132]. However, it was shown that extraction and injection barriers on electrode interfaces influence the contact selectivity in a certain way [113], [21], [114], [133]. It was even proposed (Reinhardt et al. [133]) that the selectivity of contacts can be quantified by the difference between the transport level for majority carriers and the electrode work function. The influence of transporting layers and energy barriers on contact selectivity requires more research. It can often be found in the literature [15], [39] that the contact selectivity is related to the surface recombination. It was also proposed that ideally selective contacts in OSCs can be realized by making SRVs for majority carriers to be infinitely large ($S_p^a \to \infty$ and $S_n^c \to \infty$) and SRVs for minority carriers to be zero ($S_n^a=0$ and $S_p^c=0$) at contacts.

In this thesis, the impact of the surface recombination and injection barrier heights for majority carriers on contact selectivity is considered. First, analyse the influence of the surface recombination. Starting from the condition of selective contacts given as $S_p^a \to \infty$, $S_n^c \to \infty$, $S_n^a=0$ and $S_p^c=0$. It can be confirmed that in this way, the cathode is made perfectly conductive for electrons and blocking for holes, and the anode perfectly conductive for holes and blocking for electrons. This is exactly what selective contacts should provide. However, it was shown in section 5.3 that for $S_p^a = S_n^c \to \infty$ and $S_n^a = S_p^c = 0$, the S-shaped J-V curve in OSCs is obtained (see Fig. 4.2.8, *SLLS*-combination). This means that although the selectivity condition is fulfilled the operation of the device is impaired. Obviously the existence of significant surface recombination, even for the minority carriers, is detrimental in OSCs. So the conclusion can be made that the surface recombination is not in any way associated with the selectivity of contacts. Then, the impact of injection barrier heights for majority carriers will be considered. During the operation of OSCs with good contact selectivity, the current flow of minority carriers should be suppressed. This means that the selective contact conduction can be expressed as:

$$J_n(0) = 0 \text{ and } J_p(d) = 0, \tag{4.8}$$

while,

$$J_p(0) \neq 0 \text{ and } J_n(d) \neq 0, \tag{4.9}$$

When the injection barrier heights for majority carriers are set to be zero ($\Phi_{Bn}=\Phi_{Bp}=0$) in the DDM calculations together with the $S_n^a=S_p^a=S_n^c=S_p^c=L$, the conditions 4.8 and 4.9 are reached. This is shown in Fig. 4.5.1 in which the current densities of majority and minority carriers at anode and cathode are plotted as functions of applied bias voltage.

As an overall conclusion, it is proved that the real selectivity is accomplished by providing zero injection barriers for majority carriers and as small presence of surface recombination at the contacts as possible.

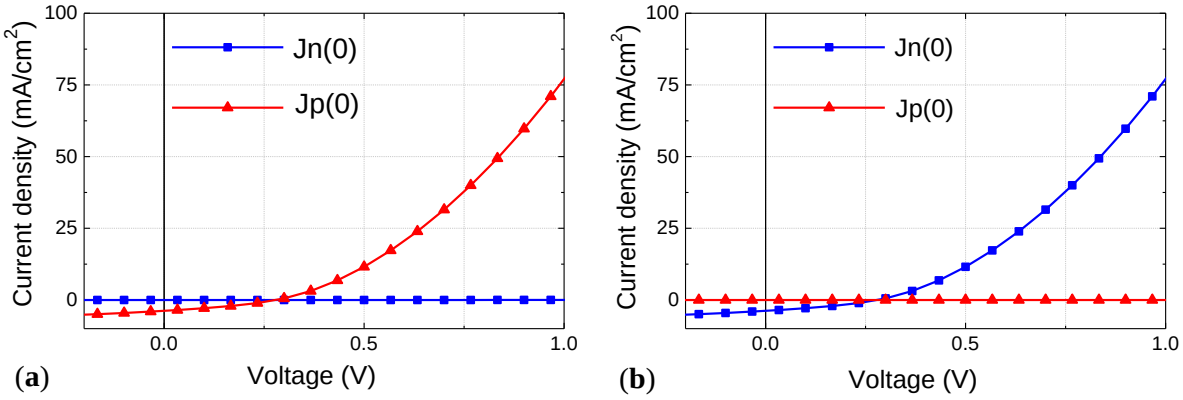

Fig. 4.5.1 *The calculated current densities of electrons and holes for* $\Phi_{Bn}=\Phi_{Bp}=0$ *and* $S_n^a=S_p^a=S_n^c=S_p^c=L$ *on* (**a**) *anode contact and* (**b**) *cathode contact. The* P3HT:ICBA *parameters are used in this calculation.*

Chapter 5

Conclusion

5 Conclusion

Most of the electricity world's needs are met by traditional energy sources using fossil fuels. These energy sources face many challenges such as rising costs and increasing risks of climate change associated with burning more fossil fuels as the global demand for electricity is growing. It means that the finite fossil resources have to be gradually replaced by renewable energy sources. Therefore, the development of alternative energy sources and new technologies for electricity generation is supported by governments and consumers.

Solar energy is one of the fastest-growing renewable energy technologies ready to play a major role in the future of electricity generation. Nowadays, solar cells generate only a very small fraction of the electricity because more than 95% of the solar cells currently used are made of costly crystalline silicon. Consequently, the researchers are investigating new solutions. Among others, solar cells based on OS materials attract attention due to their low-cost, lightweight, and mechanical flexibility. The low-cost potential of OSCs resides not only in the low price of the raw materials, but also in the printing techniques applied for their fabrication. The relatively low efficiency and poor stability are limiting the development and commercialization of organic solar cells. In the last three decades, great efforts have been devoted to material design and device structure improvement contributing to the increase in the PCE. Till today, the PCE of the OSCs has improved tremendously, the highest PCE is approaching 17.6% for single-junction [6] and exceeds 18.5% for tandem OSCs [7]. Despite advances, numerous challenges still remain to make OSCs a commercially viable.

Most progress in the development of OSCs' technology has been achieved by experimental investigation, particularly, by organic materials design in order to improve the properties of the active layers as well as by structure development through inserting the interfacial transporting and blocking layers. Physical models for OSCs are still not nearly as well developed as for inorganic solar cells (ISCs). Although there are many similarities between ISCs and OSCs, the physics of organic devices differs in a great extent from the physics of their counterparts. Therefore, a better understanding of the processes that are governing the device operation of OSCs is crucial to improve their performance.

The OSCs sometimes demonstrate S-shape deformation in their J-V characteristics. This deviation from the regular J–shape of the J-V relationship leads to a reduction of the fill factor and the PCE. Although, the S-shaped J-V curve is detrimental for OSCs' performance, it is pretty beneficial to the investigation of OSCs' physics, especially the influence of contacts. In the literature, the S-shape bending is attributed to the reduced value of SRVs for the majority carriers at the electrode contacts [15], [39]. The presence of injection and extraction barriers for majority carriers at contacts is also identified as the source of S-shape deviations in J-V characteristics [114], [134]. It is claimed that the imbalanced mobilities for holes and electrons can also produce the S-kink in the J-V curve [22]. In most cases, the existence of space charge and the inhomogeneous profile of the electric field (most often in the vicinity of electrodes) are claimed to be the direct source of S-kink in the J-V curve of OSCs.

In this thesis, the impact of surface processes, namely surface recombination, and thermal injection on the J-V characteristics of OSCs are studied. The regular J-shaped and deformed S-shaped J-V curves of OSCs were simulated and analysed by the standard DDM based on the steady-state of Poisson's equation, and continuity equations for electrons and holes. The generation rate is calculated using the transfer matrix theory assuming that the electron-hole pairs are generated instantaneously and directly by exciton dissociation. The electron and hole mobilities are assumed to be constant and the CT was considered through drift and diffusion. The Langevin bimolecular type of recombination is adopted. The boundary conditions include the surface processes on the electrodes, by taking into account the finite SRVs for electrons and holes on anode and cathode as well as the thermally activated charge carriers on the electrodes whose concentrations depend on the injection barrier heights. The SRVs and the injection barrier heights for majority carriers on the anode and cathode are varied separately in the model.

In order to analyse the impact of only SRVs on the J-V characteristics of the OSCs, the equilibrium thermionic concentrations at the electrodes are neglected. To perceive the complete influence of SRVs on the OSCs' J-V curve, the SRVs for minority and majority charge carriers on both contacts should be changed from zero to infinity. The number of J-V curves generated in this way would be enormous and unmanageable for the analyses. In this thesis, an SML-approach is developed which classifies contacts by comparing the SRV values with the charge carrier effective transport velocities (v_E) on them. For blocking contact the SRV is assigned to be small (*S*), which means at least one order of magnitude smaller than v_E, for conductive contact the SRV is assigned to be large (*L*), i.e. at least one order of magnitude larger than v_E, and when the contact is neither blocking nor conductive, the SRV has a medium-value (*M*), obviously comparable with v_E. By this approach, the number of simulated J-V curves is reduced to 81 graphs. But the J-V curve has a regular J-shape only in the case when all SRVs have L values, which means that reducing the value of any SRVs causes of S-bending in the J-V characteristic of the OSCs. It is also concluded that the SRVs for electrons have a more significant impact on the J-V characteristics of OSCs than the SRVs for holes. By increasing the hole mobility, the influence of hole SRVs becomes more pronounced.

The impact of injection barrier heights for majority carriers on the OSCs' J-V curve is analysed by taking all SRVs to be large (*L*). As a first step, the injection barrier height for holes (Φ_{Bp}) at the anode is varied in the range 0 –1.0eV, providing the injection barrier height for electrons (Φ_{Bn}) at the cathode is zero. The variation of the Φ_{Bp} doesn't cause an S-shape in the J-V characteristics. Also, it is noticed that increasing the Φ_{Bp} from 0eV to 0.7eV increases the V_{oc} of OSCs significantly, for Φ_{Bp} higher than 0.7eV the V_{oc} is not affected anymore. At the second step, the Φ_{Bn} at the cathode is changed in the same range 0 –1.0eV while Φ_{Bp} at the anode is taken to be zero. In this case, the S-shape bending appears in the J-V curve for the Φ_{Bn} larger than 0.2eV. The Φ_{Bn} has the same effect on V_{oc} as Φ_{Bp} only in the range 0 – 0.3eV.

It is important to emphasize that two different types of S-shaped J-V characteristics have been discerned in this study. The first type manifests the S-shape in the vicinity of the voltage axis, after which it grows almost exponentially and it is caused by SRV reduction. The second type also bends in the vicinity of the voltage axis, but it has only one saddle point and it proceeds to rise monotonically. This kind of S-shaped J-V curve is attributed to the existence of the Φ_{Bn} at the cathode higher than 0.2eV.

The model used in this thesis for simulation of OSCs' J-V characteristics is validated by comparison with the experimental J-V curve data obtained for ITO/PEDOT:PSS/P3HT:PCBM/Al and ITO/PEDOT:PSS/P3HT:ICBA/Al solar cells. For the P3HT:PCBM based solar cell a regular J–shaped J-V curve is measured while for P3HT:ICBA device malformed S-shaped J-V curve is recorded. The J-V characteristics for both types of solar cells are well reproduced by the model. It can be concluded that the S-shape kink in the ITO/PEDOT:PSS/P3HT:ICBA/Al J-V curve is the consequence of the electron injection barrier height larger than 0.2eV, rather than the reduction of SRV values at electrodes.

The selectivity of contacts in solar cells is the prerequisite for highly efficient device operation. It can often be found in the literature that the ideal selective electrodes are achieved when infinite SRVs for the majority and zero SRVs for the minority charge carriers are obtained. In this thesis, it is unambiguously shown that the reduction in any SRV value is leading to S-shape deviation in OSCs' J-V characteristics. Consequently, for well OSCs' operation, all SRVs should tend to infinity (be large). It is further shown that the condition of selectivity is accomplished when the injection barrier heights for majority charge carriers are zero or negative.

As a continuation of this study, the role of transport/blocking layers should be modelled and incorporated in DDM. Also, the stability of numerical calculations should be improved. A finite element method may be a good choice.

6 Appendix A (The Scharfetter–Gummel discretization)

The assumptions:

The domain is divided into *N* equal length elements as shown in Fig. A-1.

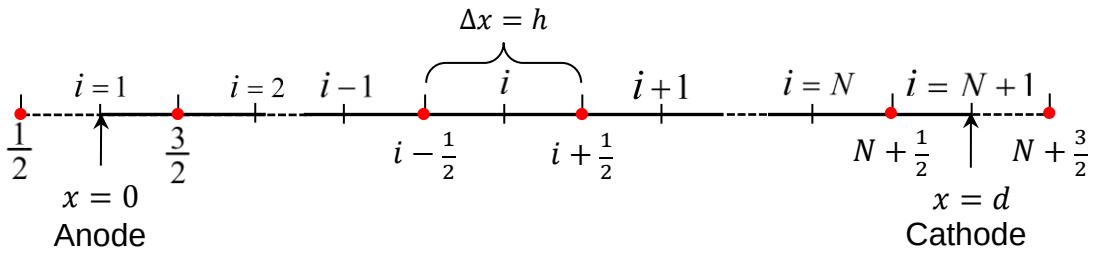

Fig. (A-1) *Domain discretization*

For the interval $\Delta x=h$, it is assumed that [100]:

- the electric field intensity E is constant,
- the electron current density J_n is constant,
- the hole current density J_p is constant.

Discretization of the system of equations 3.3.1–3.3.3:

- **For *i* >1 and *i* < N+1**:

The first equation 3.3.1 is discretized by using the central FDM for the potential φ at x_i :

$$\frac{\partial^2 \varphi}{\partial x^2} = \frac{\varphi_{i+1} - 2\varphi_i + \varphi_{i-1}}{h^2} = \frac{q}{\varepsilon}\left(n_i - p_i\right), \qquad \text{(A-1)}$$

The equations 3.3.2 and 3.3.3 are discretized by using the central FDM for φ and $J_{n(p)}$ at the midpoint $x_{i+\frac{1}{2}}$.

First, the equation 3.3.4 is written as:

$$J_{n,i+\frac{1}{2}} = -q\mu_n n(x)\left(\frac{\varphi_{i+1} - \varphi_i}{h_i}\right) + qD_n \frac{\partial n(x)}{\partial x}, \qquad \text{(A-2)}$$

and it is solved as a differential equation by $n(x)$ with $J_{n,i+\frac{1}{2}}$ taken to be the unknown constant, for $x \in [x_i, x_{i+1}]$ according to the S-G method. Using the solution of eq. A-2 $J_{n,p,i+\frac{1}{2}}$ is expressed as:

$$J_{n,i+\frac{1}{2}} = -q\mu_n \left(\frac{\varphi_{i+1} - \varphi_i}{h_i} \right) \left(\frac{n_{i+1}}{1 - \exp\left(\frac{\mu_n}{D_n} (\varphi_{i+1} - \varphi_i) \right)} + \frac{n_i}{1 - \exp\left(-\frac{\mu_n}{D_n} (\varphi_{i+1} - \varphi_i) \right)} \right), \qquad \text{(A-3)}$$

where, $h_i = x_{i+1} - x_i$, $n_i = n(x_i)$, and $n_{i+1} = n(x_{i+1})$.

The equation 3.3.2 is then written as:

$$G_i - R_{n_i} + \frac{1}{q} \left(\frac{J_{n,i+\frac{1}{2}} - J_{n,i-\frac{1}{2}}}{h} \right) = 0, \qquad \text{(A-4)}$$

when the expressions for $J_{n,i+\frac{1}{2}}$ and $J_{n,i-\frac{1}{2}}$ (obtained analogously to $J_{n,p,i+\frac{1}{2}}$) are included in the A-4, the final discretized form of the equation 3.3.2 is evaluated:

$$G_i - R_{n_i} - \mu_n \left(\frac{\varphi_{i+1} - \varphi_i}{h^2} \right) \left(\frac{n_{i+1}}{1 - \exp\left(\frac{\mu_n}{D_n} (\varphi_{i+1} - \varphi_i) \right)} + \frac{n_i}{1 - \exp\left(-\frac{\mu_n}{D_n} (\varphi_{i+1} - \varphi_i) \right)} \right) +$$
$$+ \mu_n \left(\frac{\varphi_i - \varphi_{i-1}}{h^2} \right) \left(\frac{n_i}{1 - \exp\left(\frac{\mu_n}{D_n} (\varphi_i - \varphi_{i-1}) \right)} + \frac{n_{i-1}}{1 - \exp\left(-\frac{\mu_n}{D_n} (\varphi_i - \varphi_{i-1}) \right)} \right) = 0, \qquad \text{(A-5)}$$

Similarly, the equation 3.3.5 turns into:

$$J_{p,i+\frac{1}{2}} = -q\mu_p p(x) \left(\frac{\varphi_{i+1} - \varphi_i}{h_i} \right) + qD_p \frac{\partial p(x)}{\partial x}, \qquad \text{(A-6)}$$

and $J_{p,i+\frac{1}{2}}$ becomes:

$$J_{p,i+\frac{1}{2}} = -q\mu_p \left(\frac{\varphi_{i+1} - \varphi_i}{h_i} \right) \left(\frac{p_{i+1}}{1 - \exp\left(-\frac{\mu_p}{D_p} (\varphi_{i+1} - \varphi_i) \right)} + \frac{p_i}{1 - \exp\left(\frac{\mu_p}{D_p} (\varphi_{i+1} - \varphi_i) \right)} \right), \qquad \text{(A-7)}$$

where, $p_i = p(x_i)$ and $p_{i+1} = p(x_{i+1})$.

The equation 3.3.3 becomes:

$$G_i - R_{p_i} - \frac{1}{q}\left(\frac{J_{p,i+\frac{1}{2}} - J_{p,i-\frac{1}{2}}}{h}\right) = 0\,, \tag{A-8}$$

Again by including the expressions for $J_{p,i+\frac{1}{2}}$ and $J_{p,i-\frac{1}{2}}$ in the A-8, the final discretized form of the equation 3.3.3 is:

$$G_i - R_{p_i} + \mu_p\left(\frac{\varphi_{i+1}-\varphi_i}{h^2}\right)\left(\frac{p_{i+1}}{1-\exp\left(-\frac{\mu_p}{D_p}(\varphi_{i+1}-\varphi_i)\right)} + \frac{p_i}{1-\exp\left(\frac{\mu_p}{D_p}(\varphi_{i+1}-\varphi_i)\right)}\right) -$$
$$-\mu_p\left(\frac{\varphi_i-\varphi_{i-1}}{h^2}\right)\left(\frac{p_i}{1-\exp\left(-\frac{\mu_p}{D_p}(\varphi_i-\varphi_{i-1})\right)} + \frac{p_{i-1}}{1-\exp\left(\frac{\mu_p}{D_p}(\varphi_i-\varphi_{i-1})\right)}\right) = 0, \tag{A-9}$$

- **At the anode: where $x = 0$ and $i = 1$:**

The value of J_{n_1} is approximated as $J_{n_1} = \frac{J_{n,\frac{3}{2}} + J_{n,\frac{1}{2}}}{2}$, and the BC 3.3.27b becomes:

$$q\left(n_1 - n_{th}^a\right)S_n^a = \frac{1}{2}\left(J_{n,\frac{3}{2}} + J_{n,\frac{1}{2}}\right). \tag{A-10}$$

Applying the S-G approximation to the equation 3.3.2 for $i = 1$, as:

$$G_1 - R_{n_1} + \frac{1}{q}\left(\frac{J_{n,\frac{3}{2}} - J_{n,\frac{1}{2}}}{h}\right) = 0\,. \tag{A-11}$$

From equations A-10 and A-11 $J_{n,\frac{3}{2}}$ can be determined as:

$$J_{n,\frac{3}{2}} = q\left(n_1 - n_{th}^a\right)S_n^a - \frac{1}{2}qh\left(G_1 - R_{n_1}\right). \tag{A-12}$$

On the other side, from the equation A-3, $J_{n,\frac{3}{2}}$ equals:

$$J_{n,\frac{3}{2}} = -q\mu_n\left(\frac{\varphi_2-\varphi_1}{h}\right)\left(\frac{n_2}{1-\exp\left(\frac{\mu_n}{D_n}(\varphi_{i+1}-\varphi_i)\right)} + \frac{n_1}{1-\exp\left(-\frac{\mu_n}{D_n}(\varphi_{i+1}-\varphi_i)\right)}\right). \tag{A-13}$$

By combining the equations A-12 and A-13, the final discretized equation for electrons at $i = 1$ is obtained:

$$G_1 - R_{n_1} - 2S_n^a / h\left(n_1 - n_{th}^a\right) - \\ -2\mu_n\left(\frac{\varphi_2 - \varphi_1}{h^2}\right)\left(\frac{n_2}{1-\exp\left(\frac{\mu_n}{D_n}(\varphi_2 - \varphi_1)\right)} + \frac{n_1}{1-\exp\left(-\frac{\mu_n}{D_n}(\varphi_2 - \varphi_1)\right)}\right) = 0. \quad \text{(A-14)}$$

Similarly, the final discretized equation for holes at i =1 is:

$$-G_1 + R_{p_1} - 2S_p^a / h\left(p_1 - p_{th}^a\right) - \\ -2\mu_p\left(\frac{\varphi_2 - \varphi_1}{h^2}\right)\left(\frac{p_2}{1-\exp\left(-\frac{\mu_p}{D_p}(\varphi_2 - \varphi_1)\right)} + \frac{p_1}{1-\exp\left(\frac{\mu_p}{D_p}(\varphi_2 - \varphi_1)\right)}\right) = 0. \quad \text{(A-15)}$$

- **At the cathode: where *x* =*d* and *i* =*N*+1:**

The value of $J_{n,N+1}$ is approximated as $J_{n,N+1} = \frac{J_{n,N+\frac{3}{2}} + J_{n,N+\frac{1}{2}}}{2}$, and the BC 3.3.28b becomes:

$$q\left(n_{N+1} - n_{th}^c\right)S_n^c = \frac{1}{2}\left(J_{n,N+\frac{3}{2}} + J_{n,N+\frac{1}{2}}\right), \quad \text{(A-16)}$$

Using the S-G approximation of the equation 3.3.2 at $i = N+1$ results:

$$G_{N+1} - R_{n_{N+1}} + \frac{1}{q}\left(\frac{J_{n,N+\frac{3}{2}} - J_{n,N+\frac{1}{2}}}{h}\right) = 0. \quad \text{(A-17)}$$

Eliminating $J_{n,N+\frac{3}{2}}$ from the A-16 and A-17, thus:

$$J_{n,N+\frac{1}{2}} = q\left(n_{N+1} - n_{th}^c\right)S_n^c + \frac{1}{2}qh\left(G_{N+1} - R_{n_{N+1}}\right), \quad \text{(A-18)}$$

From the equation A-3, $J_{n,N+\frac{1}{2}}$ can be written as:

$$J_{n,N+\frac{1}{2}} = -q\mu_n\left(\frac{\varphi_{N+1}-\varphi_N}{h}\right)\left(\frac{n_{N+1}}{1-\exp\left(\frac{\mu_n}{D_n}\left(\varphi_{N+1}-\varphi_N\right)\right)}+\frac{n_N}{1-\exp\left(-\frac{\mu_n}{D_n}\left(\varphi_{N+1}-\varphi_N\right)\right)}\right). \quad \text{(A-19)}$$

Finally, using A-18 and A-19, the discretized equation for electrons at $i = N+1$ is:

$$-G_{N+1}+R_{n_{N+1}}-2S_n^c/h\left(n_{N+1}-n_{th}^c\right)- \\ -2\mu_n\left(\frac{\varphi_{N+1}-\varphi_N}{h^2}\right)\left(\frac{n_{N+1}}{1-\exp\left(\frac{\mu_n}{D_n}\left(\varphi_{N+1}-\varphi_N\right)\right)}+\frac{n_N}{1-\exp\left(-\frac{\mu_n}{D_n}\left(\varphi_{N+1}-\varphi_N\right)\right)}\right)=0. \quad \text{(A-20)}$$

Similarly, the discretized equation for holes at $i = N+1$ is:

$$G_{N+1}-R_{p_{N+1}}-2S_p^c/h\left(p_{N+1}-p_{th}^c\right)- \\ -2\mu_p\left(\frac{\varphi_{N+1}-\varphi_N}{h^2}\right)\left(\frac{p_{N+1}}{1-\exp\left(-\frac{\mu_p}{D_p}\left(\varphi_{N+1}-\varphi_N\right)\right)}+\frac{p_N}{1-\exp\left(\frac{\mu_p}{D_p}\left(\varphi_{N+1}-\varphi_N\right)\right)}\right)=0. \quad \text{(A-21)}$$

The final form of discretized equations

- **For $i = 1$**

$$\varphi_1 = 0, \quad \text{(A-22)}$$

$$G_1-R_{n_1}-2S_n^a/h\left(n_1-n_{th}^a\right)- \\ -2\mu_n\left(\frac{\varphi_2-\varphi_1}{h^2}\right)\left(\frac{n_2}{1-\exp\left(\left(\varphi_2-\varphi_1\right)/V_T\right)}+\frac{n_1}{1-\exp\left(-\left(\varphi_2-\varphi_1\right)/V_T\right)}\right)=0, \quad \text{(A-23)}$$

$$-G_1+R_{p_1}-2S_p^a/h\left(p_1-p_{th}^a\right)- \\ -2\mu_p\left(\frac{\varphi_2-\varphi_1}{h^2}\right)\left(\frac{p_2}{1-\exp\left(-\left(\varphi_2-\varphi_1\right)/V_T\right)}+\frac{p_1}{1-\exp\left(\left(\varphi_2-\varphi_1\right)/V_T\right)}\right)=0, \quad \text{(A-24)}$$

where $V_T = D_{n(p)}/\mu_{n(p)}$.

- **For $i > 1$ & $i < N + 1$**

$$\left(\varphi_{i+1} - 2\varphi_i + \varphi_{i-1}\right)/h^2 - q/\varepsilon\left(n_i - p_i\right) = 0\,, \tag{A-25}$$

$$G_i - R_{n_i} - \mu_n\left(\frac{\varphi_{i+1}-\varphi_i}{h^2}\right)\left(\frac{n_{i+1}}{1-\exp\left(\left(\varphi_{i+1}-\varphi_i\right)/V_T\right)} + \frac{n_i}{1-\exp\left(-\left(\varphi_{i+1}-\varphi_i\right)/V_T\right)}\right) + \\ + \mu_n\left(\frac{\varphi_i-\varphi_{i-1}}{h^2}\right)\left(\frac{n_i}{1-\exp\left(\left(\varphi_i-\varphi_{i-1}\right)/V_T\right)} + \frac{n_{i-1}}{1-\exp\left(-\left(\varphi_i-\varphi_{i-1}\right)/V_T\right)}\right) = 0\,, \tag{A-26}$$

$$G_i - R_{p_i} + \mu_p\left(\frac{\varphi_{i+1}-\varphi_i}{h^2}\right)\left(\frac{p_{i+1}}{1-\exp\left(-\left(\varphi_{i+1}-\varphi_i\right)/V_T\right)} + \frac{p_i}{1-\exp\left(\left(\varphi_{i+1}-\varphi_i\right)/V_T\right)}\right) - \\ - \mu_p\left(\frac{\varphi_i-\varphi_{i-1}}{h^2}\right)\left(\frac{p_i}{1-\exp\left(-\left(\varphi_i-\varphi_{i-1}\right)/V_T\right)} + \frac{p_{i-1}}{1-\exp\left(\left(\varphi_i-\varphi_{i-1}\right)/V_T\right)}\right) = 0. \tag{A-27}$$

- **For $i = N + 1$**

$$\varphi_{N+1} = -V + V_{bi}\,, \tag{A-28}$$

$$-G_{N+1} + R_{n_{N+1}} - 2\,S_n^c/h\left(n_{N+1} - n_{th}^c\right) - \\ - 2\mu_n\left(\frac{\varphi_{N+1}-\varphi_N}{h^2}\right)\left(\frac{n_{N+1}}{1-\exp\left(\left(\varphi_{N+1}-\varphi_N\right)/V_T\right)} + \frac{n_N}{1-\exp\left(-\left(\varphi_{N+1}-\varphi_N\right)/V_T\right)}\right) = 0, \tag{A-29}$$

$$G_{N+1} - R_{p_{N+1}} - 2\,S_p^c/h\left(p_{N+1} - p_{th}^c\right) - \\ - 2\mu_p\left(\frac{\varphi_{N+1}-\varphi_N}{h^2}\right)\left(\frac{p_{N+1}}{1-\exp\left(-\left(\varphi_{N+1}-\varphi_N\right)/V_T\right)} + \frac{p_N}{1-\exp\left(\left(\varphi_{N+1}-\varphi_N\right)/V_T\right)}\right) = 0. \tag{A-30}$$

7 Appendix B (The MATLAB code)

Input parameters (In_Par.m)

General parameters

```
d=130;                          % thickness of the active-layer [nm].
q=1.602e-13;                    % elementary charge [A μs].
epson0=8.8542e-15;              % free space permittivity [A^2 μs^4/(kg nm^3)].
epsonR=3.4;                     % relative permittivity of active layer.
epson=epson0*epsonR;            % active layer permittivity [A^2 μs^4/(kg nm^3)].
kB=1.3806488e-17;               % Boltzmann constant [kg m^2/(K μs^2)].
T=273+20.9;                     % absolute temperature [K].
Vt=kB*T/q;                      % thermal voltage [V].
Vbi=0.78;                       % built-in-voltage [V].
```

Electron/hole parameters

```
Mn=4.92e4;                      % electron mobility [nm^2/(V μs)].
Mp0=3e8;                        % zero field hole mobility
Mp=Mp0*exp(-0.3*q/kB/T);        % hole mobility [nm^2/(V μs)].
Ms=Mn/2+Mp/2;
gamma=q/epson*Ms;               % Langevin recombination coefficient [nm^3/μs].
tn=0.62e2;                      % electron lifetime [μs].
tp=3e-1;                        % hole lifetime [μs].
Dn=Vt*Mn;                       % electron diffusion coefficient [nm^2/μs].
Dp=Vt*Mp;                       % hole diffusion coefficient [nm^2/μs].
Ln=sqrt(Dn*tn);                 % electron diffusion length [nm].
Lp=sqrt(Dp*tp);                 % hole diffusion length [nm].
Vn_diff=Ln/tn;                  % average diffusion velocity for electron [nm/ μs].
Vp_diff=Lp/tp;                  % average diffusion velocity for holes [nm/ μs].
```

Boundary conditions

```
Nc=1e-1;                        % Nc and Nv are the effective density of states [nm^-3].
Nv=1e-1;
Eg=1.4;                         % energy gap [eV].
ni=sqrt(Nc*Nv)*exp(-Eg/(2*kB*T)); % intrinsic carrier density of electrons and holes [nm^-3].
p0=1e-15;                       % hole concentration at anode [nm^-3].
nd=1e-15;                       % electron concentration at cathode [nm^-3].
```

Algorithm parameters

```
N=150;                          % the thickness d is divided into 150 equal elements.
M=31;                           % number of points in the measured data.
h=d/N;                          % the element length [nm].
x=0:h:d;                        % the domain discretization [nm].
epsilon=1e-12;                  % Computation accuracy.
izlaz=20;                       % Maximum number of iterations to exit.
%=========================================================================================%
```

All units are expressed in *nm* and *μs* because the numbers in SI-units exceed the MATLAB limit during the calculation.

```
%=========================================================================================%
```

Injection barrier height combinations (Inj_Barr.m)

```
IB_n=linspace(0,1,11);          vector of injection barrier heights for electrons ΦBn (1x11).
IB_p=linspace(0,1,11);          vector of injection barrier heights for holes ΦBp (1x11).
Loop=length(IB_n)*length(IB_p); (Loop=11x11=121) is the number of combinations.
InjB=zeros(2,Loop);             injection barrier height combinations (2x121).
i=0;
```

These for *loops are used to create the combination matrix of size* (2x121) *for* Φ_{Bn} *and* Φ_{Bp} *by changing their values in the range of* 0–1eV *with the step of* 0.1eV.

```
for ii1=1:length(IB_n)
    Fi_n=IB_n(ii1);
    for ii2=1:length(IB_p)
        Fi_p=IB_p(ii2);
        i=i+1;
        InjB(:,i)=[Fi_n; Fi_p];
    end
end
% IB=[0  0.05  0.1  0.15  0.2  0.25  0.3  0.35  0.4  0.6  0.8  1.0];
% Loop=length(IB);
```

The previous two commented lines are used when the values of injection barrier heights are changed separately. In the calculation it is used Φ_{Bn}=0 *and the value of* Φ_{Bp} *is changed and then vice versa* (Φ_{Bp}=0 and Φ_{Bn} *is changed*), *here* Loop=12.

```
%=========================================================================================%
```

SRVs combinations (SRVs_CG.m)

```
SML=500;                        scaling factor.
SS=1/SML;  MM=1;  LL=SML;       scaling factors for SS–small, MM–medium, and LL–large SRVs.
L_SRVs=4^3;                     number of SRVs combinations (L_SRVs=4^3=81) .
SRV=zeros(L_SRVs,4);            matrix of SRVs scaling factors (81X4).
XX=[SS; MM; LL];
```

These four for *loops are used to create the combinations for matrix of SRVs scaling factors* (81x4)

```
i=0;
for i1=1:3
   FSn1=XX(i1);
   for i2=1:3
      FSn2=XX(i2);
      for i3=1:3
         FSp1=XX(i3);
         for i4=1:3
            FSp2=XX(i4);
            i=i+1;
            SRV(i,:)=[FSn1  FSn2  FSp1  FSp2];
         end
      end
   end
end
%=========================================================================================%
```

Initial guess (Gen_initial_Guess)

The initial guess is the analytical solution of the system of equations 3.3.1–3.3.5 *under the assumptions of constant electric field, monomolecular recombination, and the generation rate based on Beer-Lambert absorption profile* [101]**.**

```
x=0:h:d;                    domain discretization, d is divided into N equal elements
U=linspace(0.5,-1.5,M);     bias voltage, (1xM),
```

The three auxiliary matrices (MxN+1):

```
V0=zeros(M,N+1);            electrical potential (v).
N0=zeros(M,N+1);            electrons concentration (n).
P0=zeros(M,N+1);            holes concentration (p).
```

The three matrices (MxN+1) *for the initial guesses*:

```
vit_IG=zeros(M,N+1);        initial guess for v
nit_IG=zeros(M,N+1);        initial guess for n
pit_IG=zeros(M,N+1);        initial guess for p
```

Calculation of generation rate profile based on Beer-Lambert absorption profile [90]*:*

```
a_sr=0.008023;              absorption coefficient
a=a_sr;

Gen0=6.821e–6;
Gen1=7.93e–7;
G=Gen0*exp(–a*x)+Gen1;      generation rate profile
```

The voltage loop, for each value of U*, the corresponding* n(x) *and* p(x) *are calculated and the results are saved in* V0*,* N0*, and* P0*.*

```
for o=1:M

    Vprim=U(o)+Vbi;         U(o) bias voltage, and Vbi-build-in voltage
    El_Polje=Vprim/d;       electric field

    phi_n=El_Polje/Vt;
    del_n=1/tn/Mn/Vt;
    sig_n=Gen0/Mn/Vt;

    phi_p=El_Polje/Vt;
    del_p=1/tp/Mp/Vt;
    sig_p=Gen0/Mp/Vt;

    eta_n=Gen1/Mn/Vt;
    eta_p=Gen1/Mp/Vt;

    Con_n=eta_n/del_n;
    Con_p=eta_p/del_p;

    r1=(+phi_n+sqrt(phi_n^2+4*del_n))/2;
    r2=(+phi_n-sqrt(phi_n^2+4*del_n))/2;
    s1=(-phi_p+sqrt(phi_p^2+4*del_p))/2;
    s2=(-phi_p-sqrt(phi_p^2+4*del_p))/2;

     Cn=-sig_n/(a^2+a*phi_n-del_n);
     Cp=-sig_p/(a^2-a*phi_p-del_p);
```

```
    n0=-(Vt*(Cn*a + (r2*(nd – Cn*(exp(-a*d) – exp(d*r1))+ Con_n*(exp(d*r1) – 1)))/
         (exp(d*r1) –  exp(d*r2)) – (r1*(nd – Cn*(exp(-a*d) – exp(d*r2)) +
          Con_n*(exp(d*r2) – 1)))/(exp(d*r1) – exp(d*r2))))/(El_Polje +  Vt*
         ((r1*exp(d*r2))/(exp(d*r1) – exp(d*r2)) – (r2*exp(d*r1))/(exp(d*r1) – exp(d*r2))));

    pd=(Vt*(Cp*a*exp(–a*d) + (s1*exp(d*s1)*(p0*exp(d*s2) + Cp*(exp(–a*d) –exp(d*s2)) –
         Con_p*(exp(d*s2) – 1)))/(exp(d*s1) – exp(d*s2)) – (s2*exp(d*s2)*(p0*exp(d*s1) +
         Cp*(exp(–a*d) – exp(d*s1)) – Con_p*(exp(d*s2) – 1)))/(exp(d*s1) –
         exp(d*s2))))/(El_Polje + Vt*((s1*exp(d*s1))/(exp(d*s1) – exp(d*s2)) –
         (s2*exp(d*s2))/(exp(d*s1) – exp(d*s2))));

    An=(nd–n0*exp(r2*d) – Cn*(exp(–a*d) –exp(r2*d)) –
         Con_n*(1–exp(r2*d)))/(exp(r1*d) –exp(r2*d));

    Bn=(nd–n0*exp(r1*d) – Cn*(exp(–a*d) –exp(r1*d)) –
         Con_n*(1–exp(r1*d)))/(exp(r2*d) –exp(r1*d));

    Ap=(pd–p0*exp(s2*d) – Cp*(exp(–a*d) –exp(s2*d)) –
         Con_p*(1–exp(s2*d)))/(exp(s1*d) –exp(s2*d));

   Bp=(pd–p0*exp(s1*d) – Cp*(exp(–a*d) –exp(s1*d)) –
         Con_p*(1–exp(s1*d)))/(exp(s2*d) –exp(s1*d));

    V0(o,:)=El_Polje*x;

    for i=1:N+1
       if ( i==1 )                    n and p at the anode contact where i=0.
          N0(o,i)= n0;
          P0(o,i)= p0;
       end

       if ( i>1 && i<(N+1) )          n and p at each point except the anode and cathode
          N0(o,i)= An*exp(r1*x(i)) + Bn*exp(r2*x(i)) + Cn*exp(-a*x(i)) + Con_n;
          P0(o,i)= Ap*exp(s1*x(i)) + Bp*exp(s2*x(i)) + Cp*exp(-a*x(i)) + Con_p;
       end

       if ( i==N+1 )                  n and p at the cathode contact where i=N+1.
          N0(o,i)= nd;
          P0(o,i)= pd;
       end
    end

    The resultant of the initial guesses for v, n, and p

    vit_IG(o,:)=V0(o,:);
    nit_IG(o,:)=N0(o,:);
    pit_IG(o,:)=P0(o,:);
end
%=========================================================================================%
```

The charge carrier generation rate profile in the active layer (TMO calculation)

(function [Qf]=Optical_Model_d_A(iks,de5))

Constants

```
hp = 0.6626e-21;            Planck constant [kg nm^2/µs]
c = 3e11;                   speed of light in free space [nm/µs]
```

Defining the wavelength vector (l) for the main calculation:

```
step = 10;
l = 370:step:800;           wavelength vector (1x44)
lnkmaj = 380:step:800;
lnkavgust = 400:step:800;
```

Defining the intensity of the incident light.

```
load('lambda_AM15.mat');                      wavelength vector for input AM 1.5 spectrum [nm].
load('AM15_m.mat');                                AM 1.5 spectrum [w/(m^2.nm)].
I=interp1(lambda_AM15,AM15_m,l)*0.5*10^(-18);      incident light intensity vector (1x44).
```

Defining an incident angle.

```
fi = 0;
```

Defining the number of layers in the photodetector (without air layers).

```
m = 5;
nte = zeros(m+2, length(l));          index of refraction for TE polarised light
ntm = zeros(m+2, length(l));          index of refraction for TM polarised light
kte = zeros(m+2, length(l));          extinction coefficient for TE polarised light
ktm = zeros(m+2, length(l));          extinction coefficient for TM polarised light
qte = zeros(m+2, length(l));          complex index of refraction for TE polarised light
ete = zeros(m+2, length(l));          wavenumber for TE polarised light
qtm = zeros(m+2, length(l));          complex index of refraction for TM polarised light
etm = zeros(m+2, length(l));          wavenumber for TE polarised light
ate = zeros(m+2, length(l));          absorption coefficient for TE polarised light
atm = zeros(m+2, length(l));          absorption coefficient for TM polarised light
```

Defining the thickness and refractive index for the air layer.

```
de(1) = 0;
nte(1,:)  = [1 1 1 1 1 1 1 1 1 1 1 1 1 1 1 1 1 1 1 1 1 1 1 1 1 1 1 1 1 1 1 1 1 1 1 1 1 1 1 1 1 1 1 1];
ntm(1,:) = [1 1 1 1 1 1 1 1 1 1 1 1 1 1 1 1 1 1 1 1 1 1 1 1 1 1 1 1 1 1 1 1 1 1 1 1 1 1 1 1 1 1 1 1];
```

Defining the thickness and refractive index for the glass substrate

```
de(2) = 0;

nte(2,:) = [1.48 1.48 1.47 1.47 1.47 1.47 1.47 1.47 1.47 1.47 1.47 1.47 1.47 1.46 1.46 1.46
            1.46 1.46 1.46 1.46 1.46 1.46 1.46 1.46 1.46 1.46 1.46 1.46 1.46 1.46 1.46 1.46
            1.45 1.45 1.45 1.45 1.45 1.45 1.45 1.45 1.45 1.45 1.45 1.45];
```

```
ntm(2,:) = [1.48 1.48 1.47 1.47 1.47 1.47 1.47 1.47 1.47 1.47 1.47 1.47 1.47 1.46 1.46 1.46
            1.46 1.46 1.46 1.46 1.46 1.46 1.46 1.46 1.46 1.46 1.46 1.46 1.46 1.46 1.46 1.46
            1.45 1.45 1.45 1.45 1.45 1.45 1.45 1.45 1.45 1.45 1.45 1.45];
```

Defining the thickness and refractive index n and extinction coefficient k for the ITO layer.

```
de(3) = 150;

nte(3,:) = [2.04 2.02 2 1.98 1.96 1.94 1.92 1.91 1.9 1.89 1.89 1.88 1.87 1.87 1.86 1.85 1.84
            1.84 1.83 1.82 1.81 1.8 1.8 1.79 1.78 1.77 1.76 1.75 1.74 1.73 1.72 1.71 1.7 1.7
            1.69 1.69 1.68 1.68 1.67 1.66 1.65 1.64 1.63 1.62];

kte(3,:) = [0.02 0.02 0.02 0.01 0.01 0.01 0.01 0.01 0 0 0 0 0 0 0 0 0 0 0 0 0 0 0 0 0 0 0 0 0.01
            0.01 0.01 0.01 0.01 0.01 0.01 0.02 0.02 0.02 0.02 0.02 0.02 0.02 0.02 0.03 0.03];

ntm(3,:) = [2.04 2.02 2 1.98 1.96 1.94 1.92 1.91 1.9 1.89 1.89 1.88 1.87 1.87 1.86 1.85 1.84
            1.84 1.83 1.82 1.81 1.8 1.8 1.79 1.78 1.77 1.76 1.75 1.74 1.73 1.72 1.71 1.7 1.7
            1.69 1.69 1.68 1.68 1.67 1.66 1.65 1.64 1.63 1.62];

kte(3,:) = [0.02 0.02 0.02 0.01 0.01 0.01 0.01 0.01 0 0 0 0 0 0 0 0 0 0 0 0 0 0 0 0 0 0 0 0 0.01
            0.01 0.01 0.01 0.01 0.01 0.01 0.02 0.02 0.02 0.02 0.02 0.02 0.02 0.02 0.03 0.03];
```

Defining thickness and refractive index and extinction coefficient for PEDOT layer.

```
de(4) = 40;
nte(4,:) = [1.55 1.54 1.54 1.54 1.53 1.53 1.53 1.52 1.52 1.52 1.52 1.51 1.51 1.51 1.51 1.5 1.5
            1.5 1.49 1.49 1.49 1.48 1.48 1.48 1.47 1.47 1.47 1.46 1.46 1.46 1.45 1.45 1.45 1.45
            1.44 1.44 1.44 1.44 1.44 1.43 1.43 1.43 1.43 1.43];
kte(4,:) = [0.01 0.02 0.02 0.02 0.02 0.02 0.02 0.03 0.03 0.03 0.03 0.03 0.03 0.03 0.04 0.04
            0.04 0.04 0.04 0.05 0.05 0.05 0.05 0.06 0.06 0.06 0.07 0.07 0.07 0.08 0.08 0.08
            0.09 0.09 0.09 0.1 0.1 0.1 0.11 0.11 0.12 0.12 0.12 0.13];
ntm(4,:) = [1.55 1.54 1.54 1.54 1.53 1.53 1.53 1.52 1.52 1.52 1.52 1.51 1.51 1.51 1.51 1.5 1.5
            1.5 1.49 1.49 1.49 1.48 1.48 1.48 1.47 1.47 1.47 1.46 1.46 1.46 1.45 1.45 1.45
            1.45 1.44 1.44 1.44 1.44 1.44 1.43 1.43 1.43 1.43 1.43];
ktm(4,:) = [0.01 0.02 0.02 0.02 0.02 0.02 0.02 0.03 0.03 0.03 0.03 0.03 0.03 0.03 0.04 0.04
            0.04 0.04 0.04 0.05 0.05 0.05 0.05 0.06 0.06 0.06 0.07 0.07 0.07 0.08 0.08 0.08
            0.09 0.09 0.09 0.1 0.1 0.1 0.11 0.11 0.12 0.12 0.12 0.13];
```

Defining thickness and refractive index and extinction coefficient for P3HT: ICBA *layer.*

```
load('n_i_k_lambda_maj.mat');      λ-vector for measured n and k [nm] (May 2017).
%load('n_i_k_lambda_avgust.mat');  λ-vector for measured n and k [nm], (55 cycles), (Aug.2017)

load('n_20C_maj.mat');             measured values for n (May 2017).
load('k_20C_maj.mat');             measured values for k (May 2017).
%load('n_22C_avgust.mat');         measured values for n, (55 cycles), (Aug.2017).
%load('k_22C_avgust.mat');         measured values for k, (55 cycles), (Aug.2017).

de(5) = de5;
```

Dimensional convergment

```
nte(5,1) = 1.51863;                                    (May 2017)
nte(5,2:44) = interp1(n_i_k_lambda_maj,n_20C_maj,lnkmaj);  (May 2017)
```

```
%nte(5,1:3) = [1.70995, 1.70995, 1.70995];                    (Aug. 2017)
%nte(5,4:44) = interp1(n_i_k_lambda_avgust,n_22C_avgust,lnkavgust);
kte(5,1) = 0.1595626;                                          (May 2017)
kte(5,2:44) = interp1(n_i_k_lambda_maj,k_20C_maj,lnkmaj);      (May 2017)
%kte(5,1:3) = [0.1602278, 0.1602278, 0.1602278];               (Aug. 2017)
%kte(5,4:44) = interp1(n_i_k_lambda_avgust,k_22C_avgust,lnkavgust);

ntm(5,:) = nte(5,:);
ktm(5,:) = kte(5,:);
```

Defining the thickness and refractive index and extinction coefficient for the Al layer.

```
de(6) = 100;
nte(6,:) = [0.41223 0.43744 0.46266 0.48787 0.51308 0.54105 0.57037 0.59969 0.63324
            0.66843 0.70362 0.73927 0.77592 0.81257 0.84921 0.88783 0.930287 0.972739
            1.015192 1.057644 1.10625 1.15827 1.2103 1.26232 1.31424 1.36645 1.43031
            1.49417 1.55803 1.62703 1.69751 1.768 1.83981 1.92139 2.00298 2.08456
            2.16738 2.26714 2.3669 2.4666 2.56642 2.65436 2.7301 2.76733];
kte(6,:) = [4.4622 4.5866  4.71111 4.8355 4.96 5.0843 5.2086 5.3328 5.4544 5.5748 5.6953
            5.8146 5.9313 6.0481 6.1648 6.2810 6.3965 6.5119 6.6273 6.7427 6.8548 6.965
            7.0753 7.1855 7.2957 7.4059 7.5081 7.6102 7.7124 7.8042 7.893  7.9819 8.0688
            8.142 8.2151 8.2883 8.3585 8.3881 8.4177 8.4443 8.4769 8.4646 8.4118 8.3543];
ntm(6,:) = [0.41223 0.43744 0.46266 0.48787 0.51308 0.54105 0.57037 0.59969 0.63324
            0.66843 0.70362 0.73927 0.77592 0.81257 0.84921 0.88783 0.930287 0.972739
            1.015192 1.057644 1.10625 1.15827 1.2103 1.26232 1.31424 1.36645 1.43031
            1.49417 1.55803 1.62703 1.69751 1.768 1.83981 1.92139 2.00298 2.08456
            2.16738 2.26714 2.3669 2.4666 2.56642 2.65436 2.7301 2.76733];
ktm(6,:) = [4.4622 4.5866  4.71111 4.8355 4.96 5.0843 5.2086 5.3328 5.4544 5.5748 5.6953
            5.8146 5.9313 6.0481 6.1648 6.2810 6.3965 6.5119 6.6273 6.7427 6.8548 6.965
            7.0753 7.1855 7.2957 7.4059 7.5081 7.6102 7.7124 7.8042 7.893  7.9819 8.0688
            8.142 8.2151 8.2883 8.3585 8.3881 8.4177 8.4443 8.4769 8.4646 8.4118 8.3543];
```

Defining the thickness and refractive index for the air layer.

```
de(7) = 0;
nte(7,:) = [1 1 1 1 1 1 1 1 1 1 1 1 1 1 1 1 1 1 1 1 1 1 1 1 1 1 1 1 1 1 1 1 1 1 1 1 1 1 1 1 1 1 1 1];
ntm(7,:) = [1 1 1 1 1 1 1 1 1 1 1 1 1 1 1 1 1 1 1 1 1 1 1 1 1 1 1 1 1 1 1 1 1 1 1 1 1 1 1 1 1 1 1 1];
```

Calculation of the propagation matrices and absorption coefficients for each layer (see section 3.3.2*):*

```
Lte = zeros((m + 2) * 2, 2, length(l));
Ltm = zeros((m + 2) * 2, 2, length(l));

for i = 1:(m+2)
   qte(i,:) = nte(i,:) + sqrt(-1) * kte(i,:);
   ete(i,:) = 2 * 3.1415 * qte(i,:) ./ l;
   qtm(i,:) = ntm(i,:) + sqrt(-1) * ktm(i,:);
   etm(i,:) = 2 * 3.1415 * qtm(i,:) ./ l;
```

```
   Lte((2 * i -1),1, :) = [exp(-sqrt(-1) * ete(i,:) .* de(i))];
   Lte(2 * i, 2, :) = [exp(sqrt(-1) * ete(i,:) .* de(i))];
   Ltm((2 * i -1),1, :) = [exp(-sqrt(-1) * etm(i,:) .* de(i))];
   Ltm(2 * i, 2, :) = [exp(sqrt(-1) * etm(i,:) .* de(i))];
   ate(i, :) = 4 * 3.14 * kte(i,:)./l;
   atm(i, :) = 4 * 3.14 * ktm(i,:)./l;
end
```

Calculation of the interface matrices (see section 3.3.2).

```
Ite = zeros((m + 1) * 2, 2, length(l));
Itm = zeros((m + 1) * 2, 2, length(l));
rte = zeros(m+1, length(l));          amplitude reflection coefficient for TE polarised light.
rtm = zeros(m+1, length(l));          amplitude reflection coefficient for TM polarised light.
tte = zeros(m+1, length(l));          amplitude refraction coefficient for TE polarised light.
ttm = zeros(m+1, length(l));          amplitude refraction coefficient for TM polarised light.

for i = 1:(m+1)
  rte(i, :) = (qte(i,:) - qte(i+1,:))./(qte(i,:) + qte(i+1,:));
  tte(i, :) = (2 * qte(i,:))./(qte(i,:) + qte(i+1,:));
  rtm(i, :) = (qtm(i+1,:) .* (qtm(i,:)).^2 - qtm(i,:) .* (qtm(i+1,:)).^2)./(qtm(i,:).*(qtm(i+1,:)).^2 +
              qtm(i+1,:).*(qtm(i,:)).^2);
  ttm(i, :) = (2 * qtm(i,:) .* qtm(i,:) .* qtm(i+1,:))./(qtm(i,:) .* (qtm(i+1,:)).^2 +
              qtm(i+1,:).*(qtm(i,:)).^2);
   Ite((2 * i - 1), 1, :) = [1./tte(i, :)];
   Ite((2 * i - 1), 2, :) = [rte(i, :)./tte(i, :)];
   Ite(2 * i, 1, :) = [rte(i, :)./tte(i, :)];
   Ite(2 * i, 2, :) = [1./tte(i, :)];
   Itm((2 * i - 1), 1, :) = [1./ttm(i, :)];
   Itm((2 * i - 1), 2, :) = [rtm(i, :)./ttm(i, :)];
   Itm(2 * i, 1, :) = [rtm(i, :)./ttm(i, :)];
   Itm(2 * i, 2, :) = [1./ttm(i, :)];
end
```

Descretization of x-axis starting from air-glass interface till Al-air interface.

```
dx = 1;
xn = sum(de) / dx;
E2_te = zeros (xn + 1, length(l));          optical electric field for TE light
Qte = zeros (xn + 1, length(l));
```

Calculation of the photon absorption rate for TE polarised light Qte per λ and per x

```
for p = 1:(xn + 1)
    % x = sum(de) * double(p)/ double(xn);
    x = p - 1;
```

Identifying the layer:

```
if  ( x < de(2) )
      i = 2;
      x0 = 0;
elseif ( x < (de(2) + de(3)) )
      i = 3;
      x0 = de(2);
elseif ( x < (de(2) + de(3) + de(4)) )
      i = 4;
      x0 = de(3) + de(2);
elseif ( x < (de(2) + de(3) + de(4) + de(5)) )
      i = 5;
      x0 = de(3) + de(2) + de(4);
else
      i = 6;
      x0 = de(3) + de(2) + de(4) + de(5);
end
```

Calculation of the transfer matrices (see section 3.3.2):

```
for il = 1: length(l)
    s1(1:2,:,il) = Lte(1:2,:,il);

    if  ( i > 2 )
        for j=1:(i-2)
            s1(1:2,:,il) = s1(1:2,:,il) * Ite((2 * j - 1):(2 * j), :, il) *
                           Lte((2 * (j + 1) - 1) : (2 * (j + 1)), :, il);
        end
    end
    s1(1:2,:,il) = s1(1:2,:, il) * Ite((2 * (i - 1) - 1): (2 * (i - 1)), :, il);
    s2(1:2,:,il) = Lte((2 * (m+2) - 1) : 2 * (m + 2), :, il);

    if  ( i < (m+1))
         for j=i:(m+1)
             s2(1:2,:,il) = s2(1:2,:,il) * Ite((2 * j - 1):(2 * j), :, il) * Lte((2 *
                            (j + 1)  - 1) : (2 * (j + 1)), :, il);
         end
    end
    s2(1:2,:,il) = s2(1:2,:,il) * Ite(( 2 * (m + 1)  - 1): (2 * (m + 1)), :, il);
    s111(il) = s1(1, 1, il);
    s112(il) = s1(1, 2, il);
    s121(il) = s1(2, 1, il);
    s122(il) = s1(2, 2, il);
    s211(il) = s2(1, 1, il);
    s212(il) = s2(1, 2, il);
    s221(il) = s2(2, 1, il);
    s222(il) = s2(2, 2, il);
end
```

```
    r1 = s121./s111;
    t1 = 1./s111;
    r2 = s221./s211;
    t2 = 1./s211;
    r = - s112./s111;
    t = t1./(1 - r .* r2 .* exp(2 * sqrt(-1) * ete(i, :) .* de(i)));
    t2 = t .*r2 .* exp(2 * sqrt(-1) * ete(i) .* de(i));
    ro = abs(r2);
    delta = angle(r2);
    T = nte(i, :)./nte(1, :) .* (abs(t)).^2;

    Qte(p, :) = 1/ (1.5 * hp * c) * l .* ate(i, :).* T.*I .* (exp(-ate(i, :) * (x - x0)) +
                ro.^2 .* (exp(-ate(i, :) .* (2 * de(i) – (x - x0)))) + 2 .* ro .* exp(-ate(i, :) *
                de(i)) .* cos(4 * 3.1415 * nte(i,:) ./ l .* (de(i) - (x - x0)) + delta));

    E2_te(p, :) = T.*I .* (exp(-ate(i, :) * (x - x0)) + ro.^2 .* (exp(-ate(i, :) .* (2 * de(i) –
                  (x - x0)))) + 2 .* ro .* exp(-ate(i, :) * de(i)) .* cos(4 * 3.1415 *
                  nte(i,:) ./ l .* (de(i) - (x - x0)) + delta))./(0.5 * c * eps0 * nte(i,:));

    Qteint(p) = trapz(l, Qte(p, :));          photon absorption rate profile integrated over λ for TE light.
end
```

Drawing of the Qteint *function*

```
% figure(1);
x = 0:dx:sum(de);
% plot(x, Qteint), xlabel('x(nm)'), ylabel('Qte'), xlim([de(2) + de(3) + de(4) de(2) + de(3) + de(4) +
de(5)-1]);
% plot(x, E2_te(:,22)), xlabel('x(nm)'), ylabel('E2_te');
```

Calculation of the photon absorption rate for TM polarised light Qtm per λ and per x.

```
E2_tm = zeros (xn + 1, length(l));          optical electric field for TM light.
Qtm = zeros (xn + 1, length(l));

for p = 1:(xn + 1)
    x =  p - 1;
```

Identifying the layer.

```
    if ( x < de(2) )
        i = 2;
        x0 = 0;
    elseif ( x < (de(2) + de(3)) )
        i = 3;
        x0 = de(2);
    elseif ( x < (de(2) + de(3) + de(4)) )
        i = 4;
        x0 = de(3) + de(2);
    elseif ( x < (de(2) + de(3) + de(4) + de(5)) )
```

```
    i = 5;
    x0 = de(3) + de(2) + de(4);
else
    i = 6;
    x0 = de(3) + de(2) + de(4) + de(5);
end
```

Calculation of the g transfer matrices.

```
for il = 1: length(l)
    s1(1:2,:,il) = Ltm(1:2,:,il);
    if ( i > 2 )
        for j=1:(i-2)
        s1(1:2,:,il) = s1(1:2,:,il) * Itm((2* j - 1):(2 * j), :, il) * Ltm((2*
                        (j +1) - 1) : (2* (j + 1)), :, il);
        end
    end

    s1(1:2,:,il) = s1(1:2,:, il) * Itm((2 * (i - 1) - 1): (2 * (i - 1)), :, il);
    s2(1:2,:,il) = Ltm((2 * (m+2) - 1) : 2 * (m + 2), :, il);

    if ( i < (m+1) )
        for j=i:(m+1)
            s2(1:2,:,il) = s2(1:2,:,il) * Itm((2 * j - 1):(2 * j), :, il) * Ltm((2*
                            (j + 1) -1) : (2* (j+1)), :, il);
        end
    end

    s2(1:2,:,il) = s2(1:2,:,il) * Itm(( 2 * (m + 1)  - 1): (2 * (m + 1)), :, il);
    s111(il) = s1(1, 1, il);
    s112(il) = s1(1, 2, il);
    s121(il) = s1(2, 1, il);
    s122(il) = s1(2, 2, il);
    s211(il) = s2(1, 1, il);
    s212(il) = s2(1, 2, il);
    s221(il) = s2(2, 1, il);
    s222(il) = s2(2, 2, il);
end
r1 = s121./s111;
t1 = 1./s111;
r2 = s221./s211;
t2 = 1./s211;
r = - s112./s111;
t = t1./(1 - r .* r2 .* exp(2 * sqrt(-1) * etm(i, :) .* de(i)));
t2 = t .*r2 .* exp(2 * sqrt(-1) * etm(i) .* de(i));
ro = abs(r2);
delta = angle(r2);
T = ntm(i, :)./ntm(1, :) .* (abs(t)).^2;
```

```
    Qtm(p, :) = 1/ (1.5 * hp * c) * l .* ate(i, :).* T.* I .* (exp(-atm(i, :) * (x - x0)) +
                ro.^2 .* (exp(-atm(i, :) .* (2 * de(i) - (x - x0)))) + 2 .* ro .* exp(-atm(i, :) *
                de(i)) .* cos(4 * 3.1415 * ntm(i,:) ./ l .* (de(i) - (x - x0)) + delta));
    E2_tm(p, :) = T.* I .* (exp(-atm(i, :) * (x - x0)) + ro.^2 .* (exp(-atm(i, :) .* (2 * de(i) –
                  (x - x0)))) + 2 .* ro .* exp(-atm(i, :) * de(i)) .* cos(4 * 3.1415 *
                  ntm(i,:) ./ l .* (de(i) - (x - x0)) + delta))./(0.5 * c * eps0 * ntm(i,:));
    Qtmint(p) = trapz(l, Qtm(p, :));          photon absorption rate profile integrated over λ for TM light.
end
```

Drawing of the Qtmint *function*

```
% figure(2);
x = 0:dx:sum(de);

% plot(x, Qtmint), xlabel('x(nm)'), ylabel('Qtm'), xlim([de(2) + de(3) + de(4) de(2) + de(3) + de(4) +
de(5)-1]);
% plot(x, E2_tm(:,22)), xlabel('x(nm)'), ylabel('E2_tm');
dn = de(2) + de(3) + de(4)+1;
gr = de(2) + de(3) + de(4) + de(5);
Qint = Qteint + Qtmint;
```

Generatio rate profile in the active layer:

```
Q = Qteint(dn:gr)+Qtmint(dn:gr);
x5 = linspace(0,de(5),de(5)+1);
Qf = interp1(x5,[Q,Q(de(5))],iks);
% figure(3)
% plot(x, Qint), xlabel('x(nm)'), ylabel('Qint'), xlim([dn gr]);
%=========================================================================================%
```

The DDM (Newton_SG_OGen_Full_BCs)

The main Code

```
close all;  clear all;  clc;
format long
```

```
In_Par                          input parameters.
Inj_Barr                        injection barrier height combinations.
SRVs_CG                         SRVs combinations.
Git= Optical_Model_d_A(x,d);    generation rate profile.
Gen_initial_Guess               initial guess.

load('JPH_m.mat')               measured J-V data of P3HT:ICBA.
ICBA_m=JPH_m(2,:);              the second row is corresponding to temperature of 20 deg.
load('Jlight_T_i_d')            measured J-V data for P3HT:PCBM.
PCBM_m=Jlight_T_i_d(2,63:93);   the second row corresponding to temperature of 20 deg and the
                                column from 63 to 93 corresponding to the film thickness of 130nm .

If=zeros(L_SRVs,M);             calculated J-V values for different SRVs combinations (81x31).
If_SRV_Scaled=zeros(L_SRVs,M);  scaled J-V values to fit the best to experimental data.
If=zeros(Loop,M);               calculated J-V values for different Φ_Bp and Φ_Bn combinations
                                (121x31).
If_IB_Scaled=zeros(Loop,M);     scaled J-V values to fit the best to experimental data..
E_Field=zeros(M,N+1);           electric field.
```

This for-*loop is used to change the combination values of the injection barrier heights for electrons and holes, where* Loop *is the total number of combinations.*

```
for tt=1:Loop
   % Vn=0;          Vp= IB(tt)*q;     Vn= Φ_Bn =0 and Vp=Φ_Bp is changed
   % Vn= IB(tt)*q;  Vp= 0;           Vn=Φ_Bn is changed and Vp=Φ_Bp =0 and
    Vn=InjB(1,tt)*q;                 Loop=11x11=121, when InjB is used and Loop=12 when IB is used,
    Vp=InjB(2,tt)*q;                 where, IB, and InjB are specified in (Inj_Barr.m)
```

The thermal concentrations for electrons (nth) and holes (pth) at anode (a) and cathode (c).

```
   nth_a=Nc*exp(-(Eg-Vp)/(kB*T));
   pth_a=Nv*exp(-Vp/(kB*T));
   nth_c=Nc*exp(-Vn/(kB*T));
   pth_c=Nv*exp(-(Eg-Vn)/(kB*T));
```

This for-loop is used to change the combination values of the SRVs *for electrons and holes, on the anode and the cathode.*

```
      for kk=1:L_SRVs
        Sn1=SRV(kk,1)*Vn_diff;     Sn1=Sna=SRV of electrons at anode.
        Sn2=–SRV(kk,2)*Vn_diff;    Sn2=Snc=SRV of electrons at cathode.
        Sp1=–SRV(kk,3)*Vp_diff;    Sp2=Spa=SRV of holes at anode.
        Sp2=SRV(kk,4)*Vp_diff;     Sp2=Spc=SRV of holes at cathode.
```

Vn_diff *and* Vp-diff *are the average diffusion velocity of electrons and holes, respectively.*

```
jj=1;
```
the initial guess combination created by the **Gen_initial_Guess** (*any value from* 1–M).

```
vit=vit_IG(jj,:);
nit=nit_IG(jj,:);
pit=pit_IG(jj,:);
```

The initial guess is chosen from IG-matrices by free choice and so on, it is used only in the first iteration. Then the solutions obtained for v, n, *and* p *are used as the initial guess for the second iteration. Using the IG-matrices as initial guess gives more stability in the numerical calculation.*

The matrices for the final results of v, n, and p (M x N+1)

```
vF=zeros(M,N+1);
nF=zeros(M,N+1);
pF=zeros(M,N+1);
```

In this for *loop, the voltage* v, *the electron concentration* n, *and the hole concentration* p *are determined for each value of U* vector.

```
for o=1:M
    Vprim=U(o)+Vbi;
    raz=1;
    counts=0;
```

The while loop is used to repeat the iterations until one of two following conditions is satisfied.
The first condition; the absolute value of raz=$\Delta \mathbf{x}$ (see Sec. 3.3.6) *is compared with a pre-specified tolerance epsilon=*δ (see Sec 3.3.6) *which defines the accuracy level of the calculation. Quantity epsilon is input parameter.*
The second condition; the number of iterations is equal to a particular number izlaz. Quantity izlaz is input parameter.

```
    while(raz>epsilon && counts<izlaz)
        Xit=[vit nit pit];
```

Discretized equation, vectors (1xN+1)

```
        V_vector=zeros(1,N+1);
```
discretized Poison's equation

```
        N_vector=zeros(1,N+1);
```
discretized continuity equation for electrons

```
        P_vector=zeros(1,N+1);
```
discretized continuity equation for holes

The elements of Jacobian matrix, whose are the partial derivatives of the system equations V, N *and* P-vector, *with respect to* v, n, *and* p, *each matrix of size* (151X151).

```
        Jav=zeros(N+1,N+1);
```
matrix of the partial derivations of V_vector equation with respect to v

```
        Jan=zeros(N+1,N+1);
```
= = = = = = = = = n

```
        Jap=zeros(N+1,N+1);
```
= = = = = = = = = p

```
        Jbv=zeros(N+1,N+1);
```
matrix of the partial derivations of N_vector equation with respect to v

```
        Jbn=zeros(N+1,N+1);
```
= = = = = = = = = n

```
        Jbp=zeros(N+1,N+1);
```
= = = = = = = = = p

```
        Jcv=zeros(N+1,N+1);
```
matrix of the partial derivations of P_vector equation with respect to v

```
        Jcn=zeros(N+1,N+1);
```
= = = = = = = = = n

```
        Jcp=zeros(N+1,N+1);
```
= = = = = = = = = p

This for loop calculates the discretized equations V_vector, N_vector and P_vector and their partial derivatives Jacobian matrixes.

```
for i=1:N+1
```

At the anode contact where i=1.

```
 if (i == 1)
    V_vector(i) = vit(i);
    N_vector(i) = Git(i) – gamma*(nit(i)*pit(i)–ni^2) – 2*Sn1/h*(nit(i)–nth_a) – (vit(i+1)–
                  vit(i))*2*Mn/h^2*(nit(i+1)/(1–exp((vit(i+1)–vit(i))/Vt)) +
                  nit(i)/(1–exp(–(vit(i+1)–vit(i))/Vt)));
    P_vector(i) = –Git(i) + gamma*(nit(i)*pit(i)–ni^2) – 2*Sp1/h*(pit(i)–pth_a) – (vit(i+1)–
                  vit(i))*2*Mp/h^2*(pit(i+1)/(1–exp(–(vit(i+1)–vit(i))/Vt)) +
                  pit(i)/(1–exp((vit(i+1)–vit(i))/Vt)));
    Jav(i,i)=1;
    Jbv(i,i)= (Mn*(2*vit(i) – 2*vit(i+1))*((nit(i)*exp((vit(i) – vit(i+1))/Vt))/(Vt*(exp((vit(i) –
              vit(i+1))/Vt) – 1)^2) –  (nit(i+1)*exp(-(vit(i) – vit(i+1))/Vt))/(Vt*(exp(–(vit(i) –
              vit(i+1))/Vt) – 1)^2)))/h^2 – (2*Mn*(nit(i)/(exp((vit(i) – vit(i+1))/Vt) – 1) +
              nit(i+1)/(exp(–(vit(i) – vit(i+1))/Vt)– 1)))/h^2;
    Jbv(i,i+1)= (2*Mn*(nit(i)/(exp((vit(i) – vit(i+1))/Vt) –1) + nit(i+1)/(exp(-(vit(i) –
                vit(i+1))/Vt) – 1)))/h^2 – (Mn*(2*vit(i) – 2*vit(i+1))*((nit(i)*exp((vit(i) –
                vit(i+1))/Vt))/(Vt*(exp((vit(i)–vit(i+1))/Vt)–1)^2) – (nit(i+1)*exp(–(vit(i) –
                vit(i+1))/Vt))/(Vt*(exp(–(vit(i) – vit(i+1))/Vt) –1)^2)))/h^2;
   Jbn(i,i)= – (2*Sn1)/h–gamma*pit(i)–(Mn*(2*vit(i)–2*vit(i+1)))/(h^2*(exp((vit(i) –
              vit(i+1))/Vt)–1));
    Jbn(i,i+1)= – (Mn*(2*vit(i)–2*vit(i+1)))/(h^2*(exp(–(vit(i)–vit(i+1))/Vt)–1));
    Jbp(i,i)= – gamma*nit(i);
    Jcv(i,i)= – (2*Mp*(pit(i)/(exp(–(vit(i)–vit(i+1))/Vt) –1) + pit(i+1)/(exp((vit(i)–
              vit(i+1))/Vt) –1)))/h^2 – (Mp*(2*vit(i) –2*vit(i+1))*((pit(i)*exp(–(vit(i)–
              vit(i+1))/Vt))/(Vt*(exp(–(vit(i)–vit(i+1))/Vt) –1)^2) – (pit(i+1)*exp((vit(i)–
              vit(i+1))/Vt))/(Vt*(exp((vit(i)–vit(i+1))/Vt)–1)^2)))/h^2;
    Jcv(i,i+1)= (2*Mp*(pit(i)/(exp(–(vit(i)–vit(i+1))/Vt)–1)+ pit(i+1)/(exp((vit(i)–
                vit(i+1))/Vt)–1)))/h^2 + (Mp*(2*vit(i)–2*vit(i+1))*((pit(i)*exp(–(vit(i)–
                vit(i+1))/Vt))/(Vt*(exp(–(vit(i)–vit(i+1))/Vt)–1)^2) – (pit(i+1)*exp((vit(i)–
                vit(i+1))/Vt))/(Vt*(exp((vit(i)–vit(i+1))/Vt)–1)^2)))/h^2;
    Jcn(i,i)= gamma*pit(i);
    Jcp(i,i)= gamma*nit(i) – (2*Sp1)/h – (Mp*(2*vit(i) – 2*vit(i+1)))/(h^2*(exp(–(vit(i) –
              vit(i+1))/Vt) – 1));
    Jcp(i,i+1)= – (Mp*(2*vit(i) – 2*vit(i+1)))/(h^2*(exp((vit(i) – vit(i+1))/Vt) – 1));
 end
```

```
At all points except the anode and cathode contacts where i=2,.....,N.
 if (i > 1 && i < N+1)

    V_vector(i)= (vit(i+1)–2*vit(i)+vit(i–1))/h^2 – q/epson*nit(i)+ q/epson*pit(i);

    N_vector(i)= Git(i) – gamma*(nit(i)*pit(i)-ni^2) – (vit(i+1)–vit(i))*Mn/h^2 *
                 (nit(i+1)/(1–exp((vit(i+1)–vit(i))/Vt)) + nit(i)/(1–exp(–(vit(i+1)–vit(i))/Vt))) +
                 (vit(i) – vit(i–1))*Mn/h^2*(nit(i)/(1–exp((vit(i) – vit(i–1))/Vt)) +
                 nit(i–1)/(1–exp(–(vit(i)–vit(i–1))/Vt)));

    P_vector(i)= Git(i) – gamma*(nit(i)*pit(i) – ni^2) +  (vit(i+1) – vit(i))*Mp/h^2 *
                 (pit(i+1)/(1–exp(–(vit(i+1)-vit(i))/Vt)) + pit(i)/(1–exp((vit(i+1)–vit(i))/Vt))) –
                 (vit(i) – vit(i–1))*Mp/h^2*(pit(i)/(1–exp(–(vit(i)–vit(i–1))/Vt)) +
                  pit(i–1)/(1–exp((vit(i)–vit(i–1))/Vt)));


    Jav(i,i-1)= 1/h^2;

    Jav(i,i) = –2/h^2;

    Jav(i,i+1) = 1/h^2;

    Jan(i,i) = –q/epson;

    Jap(i,i) = q/epson;

    Jbv(i,i-1) = (Mn*(nit(i)/(exp((vit(i) – vit(i–1))/Vt) – 1) + nit(i–1)/(exp(–(vit(i) –
                 vit(i–1))/Vt)–1)))/h^2– (Mn*((nit(i)*exp((vit(i)–vit(i–1))/Vt))/(Vt*(exp((vit(i)–
                 vit(i–1))/Vt)–1)^2) – (nit(i–1)*exp(–(vit(i) – vit(i–1))/Vt))/(Vt*(exp(–(vit(i) –
                 vit(i–1))/Vt) –1)^2))*(vit(i) – vit(i–1)))/h^2;

    Jbv(i,i) = (Mn*((nit(i)*exp((vit(i) – vit(i–1))/Vt))/(Vt*(exp((vit(i) – vit(i–1))/Vt) – 1)^2) –
               (nit(i–1)*exp(–(vit(i)– vit(i–1))/Vt))/(Vt*(exp(-(vit(i)–vit(i–1))/Vt)–1)^2))*(vit(i) –
                vit(i–1)))/h^2 – (Mn*(nit(i)/(exp((vit(i) – vit(i+1))/Vt) – 1)+ nit(i+1)/
                (exp(–(vit(i)–vit(i+1))/Vt) – 1)))/h^2 – (Mn*(nit(i)/(exp((vit(i)– vit(i–1))/Vt)–1) +
               nit(i–1)/(exp(– (vit(i) - vit(i-1))/Vt) –1)))/h^2 +  (Mn*((nit(i)*exp((vit(i) –
               vit(i+1))/Vt))/(Vt*(exp((vit(i) – vit(i+1))/Vt) –1)^2) –(nit(i+1)*exp(– (vit(i)–
               vit(i+1))/Vt))/(Vt*(exp(-(vit(i) – vit(i+1))/Vt) –1)^2))*(vit(i) – vit(i+1)))/h^2;

    Jbv(i,i+1) = (Mn*(nit(i)/(exp((vit(i) – vit(i+1))/Vt) – 1) + nit(i+1)/(exp(-(vit(i) –
                  vit(i+1))/Vt) – 1)))/h^2 – (Mn*((nit(i)*exp((vit(i) – vit(i+1))/Vt))/(Vt*
                 (exp((vit(i) – vit(i+1))/Vt) – 1)^2) – (nit(i+1)*exp(–(vit(i) – vit(i+1))/Vt))/(Vt*
                 (exp(–(vit(i)– vit(i+1))/Vt)  – 1)^2))*(vit(i) – vit(i+1)))/h^2;

    Jbn(i,i-1) = – (Mn*(vit(i) – vit(i–1)))/(h^2*(exp(–(vit(i) – vit(i–1))/Vt) – 1));

    Jbn(i,i) = – gamma*pit(i) – (Mn*(vit(i) – vit(i–1)))/(h^2*(exp((vit(i)– vit(i–1))/Vt) – 1)) –
                (Mn*(vit(i) – vit(i+1)))/(h^2*(exp((vit(i)– vit(i+1))/Vt) – 1));

    Jbn(i,i+1) =  – (Mn*(vit(i) – vit(i+1)))/(h^2*(exp(–(vit(i) – vit(i+1))/Vt) – 1));

    Jbp(i,i) = – gamma*nit(i);

    Jcv(i,i-1) =  – (Mp*(pit(i)/(exp(–(vit(i) – vit(i-1))/Vt)–1) + pit(i–1)/(exp((vit(i) –
                   vit(i–1))/Vt) – 1)))/h^2 – (Mp*((pit(i)*exp(–(vit(i) – vit(i–1))/Vt))/(Vt*
                  (exp(–(vit(i)– vit(i–1))/Vt) – 1)^2) – (pit(i–1)*exp((vit(i)– vit(i–1))/Vt))/(Vt*
                  (exp((vit(i)– vit(i–1))/Vt)– 1)^2))*(vit(i) – vit(i–1)))/h^2;
```

```
Jcv(i,i) = (Mp*(pit(i)/(exp(–(vit(i) – vit(i–1))/Vt) – 1) + pit(i–1)/(exp((vit(i) –
           vit(i–1))/Vt) – 1)))/h^2 + (Mp*(pit(i)/(exp(-(vit(i) – vit(i+1))/Vt) – 1) +
           pit(i+1)/(exp((vit(i) – vit(i+1))/Vt) – 1)))/h^2 + (Mp*((pit(i)*exp(-(vit(i) –
           vit(i–1))/Vt))/(Vt*(exp(–(vit(i) – vit(i–1))/Vt) – 1)^2) – (pit(i–1)*exp((vit(i) –
           vit(i–1))/Vt))/(Vt*(exp((vit(i) – vit(i–1))/Vt) – 1)^2))*(vit(i)– vit(i–1)))/h^2 +
          (Mp*((pit(i)*exp(–(vit(i) – vit(i+1))/Vt))/(Vt*(exp(–(vit(i) – vit(i+1))/Vt) – 1)^2) –
          (pit(i+1)*exp((vit(i) – vit(i+1))/Vt))/(Vt*(exp((vit(i) – vit(i+1))/Vt)–1)^2))*(vit(i) –
           vit(i+1)))/h^2;

Jcv(i,i+1) = – (Mp*(pit(i)/(exp(-(vit(i) – vit(i+1))/Vt) – 1) + pit(i+1)/(exp((vit(i) –
               vit(i+1))/Vt) – 1)))/h^2 – (Mp*((pit(i)*exp(–(vit(i)– vit(i+1))/Vt))/(Vt*
               (exp(-(vit(i) – vit(i+1))/Vt) – 1)^2)– (pit(i+1)*exp((vit(i) vit(i+1))/Vt))/(Vt*
               (exp((vit(i)– vit(i+1))/Vt) – 1)^2))*(vit(i) – vit(i+1)))/h^2;

Jcn(i,i)= – gamma*pit(i);

Jcp(i,i-1) = (Mp*(vit(i) – vit(i–1)))/(h^2*(exp((vit(i) – vit(i-1))/Vt) – 1));

Jcp(i,i) = (Mp*(vit(i) – vit(i–1)))/(h^2*(exp(–(vit(i) – vit(i-1))/Vt) – 1))- gamma*nit(i) +
           (Mp*(vit(i) – vit(i+1)))/(h^2*(exp(–(vit(i) – vit(i+1))/Vt) – 1));

Jcp(i,i+1) = (Mp*(vit(i) – vit(i+1)))/(h^2*(exp((vit(i) – vit(i+1))/Vt) – 1));

End
```

At the cathode contact where i=N+1.

```
if ( i == N+1 )

V_vector(I) = vit(i)-Vprim;

N_vector(i) = –Git(i) + gamma*(nit(i)*pit(i)-ni^2) – 2*Sn2/h*(nit(i)–nth_c) –
              (vit(i)–vit(i–1))*2*Mn/h^2*( nit(i)/(1– exp((vit(i)–vit(i–1))/Vt))+
              nit(i–1)/(1–exp(–(vit(i)–vit(i–1))/Vt)));

P_vector(i) =  Git(i) – gamma*(nit(i)*pit(i)–ni^2) – 2*Sp2/h*(pit(i)–pth_c) –
              (vit(i)–vit(i–1))*2*Mp/h^2*( pit(i)/(1– exp(–(vit(i)–vit(i–1))/Vt))+
              pit(i–1)/(1–exp((vit(i)–vit(i–1))/Vt)));

Jav(i,i)= 1;

Jbv(i,i-1) = (Mn*(2*vit(i) – 2*vit(i–1))*((nit(i)*exp((vit(i) – vit(i–1))/Vt))/(Vt*(exp((vit(i) –
             vit(i–1))/Vt) – 1)^2) – (nit(i–1)*exp(–(vit(i) – vit(i–1))/Vt))/(Vt*(exp(–(vit(i) –
             vit(i–1))/Vt) – 1)^2)))/h^2 – (2*Mn*(nit(i)/(exp((vit(i) – vit(i–1))/Vt) – 1) +
             nit(i–1)/(exp(–(vit(i) – vit(i–1))/Vt) –1)))/h^2;

Jbv(i,i) = (2*Mn*(nit(i)/(exp((vit(i) – vit(i–1))/Vt) – 1) + nit(i–1)/(exp(–(vit(i) –
           vit(i–1))/Vt) – 1)))/h^2 – (Mn*(2*vit(i) –2*vit(i–1))*((nit(i)*exp((vit(i) –
           vit(i–1))/Vt))/(Vt*(exp((vit(i) – vit(i–1))/Vt) – 1)^2) – (nit(i–1)*exp(–(vit(i) –
           vit(i–1))/Vt))/(Vt*(exp(–(vit(i) – vit(i–1))/Vt) – 1)^2)))/h^2;

Jbn(i,i-1 )= (Mn*(2*vit(i) – 2*vit(i–1)))/(h^2*(exp(–(vit(i) – vit(i–1))/Vt) – 1));

Jbn(i,i) = gamma*pit(i) – (2*Sn2)/h + (Mn*(2*vit(i) – 2*vit(i–1)))/(h^2*(exp((vit(i) –
           vit(i–1))/Vt) – 1));
```

```
Jbp(i,i) = gamma*nit(i);

Jcv(i,i-1) = – (2*Mp*(pit(i)/(exp(–(vit(i) – vit(i–1))/Vt) – 1) + pit(i–1)/(exp((vit(i) –
             vit(i–1))/Vt) – 1)))/h^2 – (Mp*(2*vit(i) – 2*vit(i–1))*((pit(i)*exp(–(vit(i) –
             vit(i–1))/Vt))/(Vt*(exp(–(vit(i) – vit(i–1))/Vt) – 1)^2) – (pit(i–1)*exp((vit(i) –
             vit(i–1))/Vt))/(Vt*(exp((vit(i) – vit(i–1))/Vt) – 1)^2)))/h^2;

Jcv(i,i) = (2*Mp*(pit(i)/(exp(–(vit(i) – vit(i–1))/Vt) – 1) + pit(i–1)/(exp((vit(i) –
           vit(i–1))/Vt) – 1)))/h^2 + (Mp*(2*vit(i) –2*vit(i–1))*((pit(i)*exp(–(vit(i) –
           vit(i–1))/Vt))/(Vt*(exp(–(vit(i) – vit(i–1))/Vt) – 1)^2) – (pit(i-1)*exp((vit(i) –
           vit(i–1))/Vt))/(Vt*(exp((vit(i) – vit(i–1))/Vt) – 1)^2)))/h^2;

Jcn(i,i) = -gamma*pit(i);

Jcp(i,i-1) = (Mp*(2*vit(i) – 2*vit(i-1)))/(h^2*(exp((vit(i) – vit(i–1))/Vt) – 1));

Jcp(i,i) = (Mp*(2*vit(i) – 2*vit(i-1)))/(h^2*(exp(–(vit(i) – vit(i–1))/Vt) – 1)) –
           (2*Sp2)/h – gamma*nit(i);
 end
end
```

VECTOR=[**V_vector N_vector P_vector**]; *equation system vector* $\mathbf{F(x)}$

The sub-matrices of Jacobian matrix (N+1) X [3X(N+1)]

Ja=[**Jav Jan Jap**];

Jb=[**Jbv Jbn Jbp**];

Jc=[**Jcv Jcn Jcp**];

The Jacobian square matrix [3X(N+1)] X[3X(N+1)]

Jacobian=[**Ja**;**Jb**;**Jc**];

Invers=inv(**Jacobian**);

delta=zeros(1,3*(N+1));

```
for i=1:3*(N+1)
   temp=0;
   for j=1:3*(N+1)
      temp=temp+VECTOR(j)*Invers(i,j);      eq. 3.3.35
   end
   delta(i)=temp;
end
```

Xnext=Xit–delta; *calculating the value of* $\mathbf{X}_{k+1}$ (eq. 3.3.36) *where* k *is the number of the current iteration.*

raz=max(abs(delta)) *the absolute value of* $\Delta\mathbf{X}$.

```
v_next=zeros(1,N+1);
n_next=zeros(1,N+1);
p_next=zeros(1,N+1);
```

```
        for i=1:N+1
            v_next(i)=Xnext(i);
            n_next(i)=Xnext(i+(N+1));
            p_next(i)=Xnext(i+2*(N+1));
        end
        if ( raz > epsilon )                    the formation of a new initial guess
            vit=v_next;
            nit=n_next;
            pit=p_next;
        end
        counts= counts+1;                       counts the number of iterations in the while loop.
    end
```

The resultant values of v, n, *and* p *are considered to be the final solutions for the current* o-*point* (selected bias voltage value) *if the while conditions are satisfied. The complete calculation is repeated for the next o-point using these final solutions as an initial guess for the next* o-*point.*

```
        for i=1:N+1
            vF(o,i)=vit(i);
            nF(o,i)=nit(i);
            pF(o,i)=pit(i);
        end
    end
```

Calculating the total current density for each o *point for different values of SRVs.*

```
    for i=1:M

        If(kk,i)=Curr_SRV_IB(vF(i,:),nF(i,:),pF(i,:),Sn1,Sn2,Sp1,Sp2,nth_a,nth_c,pth_a,pth_c);

    end
```

The **Curr_SRV_IB** *function is given below the main calculation.*

Scaling the graph using the scaling factor SF [90]

```
    SF=1.5;
    for k=1:M
        If_SRV_Scaled(kk,k)=If(kk,k)/SF;
    end
```

Calculating the total current density for each o *point for different injection barrier heights.*

```
%    for i=1:M
%        If(tt,i)=Curr_SRV_IB(vF(i,:),nF(i,:),pF(i,:),Sn1,Sn2,Sp1,Sp2,nth_a,nth_c,pth_a,pth_c);
%    end
%% Scaling the graph
%    for k=1:M
%        If_IB_Scaled(tt,k)=If(kk,k)/SF;
%    end
  end
```

```
Varying the  SRVs values and determination of the least square fit to the measured data .
  XX=ICBA_m;
  YY=If_SRV_Scaled(kk,:);
  Euclidean_D(kk,1)=pdist2(XX,YY);
  Min_ED=min(nonzeros(Euclidean_D));
  if (Min_ED < MIN)
     MIN=Min_ED;
     Result=If_SRV_Scaled(kk,:);
     Index=kk;
  end
end
Plotting the calculated and measured J-V characteristics.
plot(-U,Result,'b', Voltage,ICBA_m,'--r','LineWidth',2);  grid on; hold on
title('J-V Characteristics ','FontSize',14);
xlabel('Voltage [V]');
ylabel('Current Density [mA/cm^2]');
%=========================================================================================%
```

The current function

(function[I]= Curr_SRV_IB(V, n, p, Sn1, Sn2, Sp1, Sp2, nth_a, nth_c, pth_a, pth_c)**)**

This function calculates the current density for each bias voltage value.

```
Jn=zeros(1,N+1);          electron current density vector (1xN+1).
Jp=zeros(1,N+1);          hole current density vector (1xN+1).

for i=1:N+1
```

Calculating the J_n and J_p on the anode

```
    if(i==1)
      Jn(i) = +q*Sn1*(n(i)-nth_a);

      Jp(i) = +q*Sp1*(p(i)-pth_a);
    end
```

Calculating the J_n and J_p at all domain points except on the anode and cathode.

```
    if ( i>1 && i<N+1 )
      Jn(i) = –q*Mn/h/2*((V(i+1) – V(i)) * (n(i+1)/(1– exp((V(i+1) – V(i))/Vt)) +
                n(i)/(1–exp(–(V(i+1)–V(i))/Vt))) + (V(i)–V(i–1))*(n(i)/(1–exp((V(i)-V(i–1))/Vt)) +
                n(i–1)/(1–exp(–(V(i)–V(i–1))/Vt))));

      Jp(i) = –q*Mp/h/2*((V(i+1) – V(i)) * (p(i+1)/(1– exp(–(V(i+1) – V(i))/Vt)) +
               p(i)/(1–exp((V(i+1)–V(i))/Vt))) + (V(i)–V(i–1))*(p(i)/(1–exp(–(V(i)–V(i–1))/Vt)) +
               p(i–1)/(1–exp((V(i)–V(i–1))/Vt))));
    end
```

Calculating the J_n and J_p on the cathode.

```
    if ( i==N+1 )
      Jn(i) = +q*Sn2*(n(i)-nth_c);

      Jp(i) = +q*Sp2*(p(i)-pth_c);
    end
  end
```

Calculating the total current density.

```
  J=Jn+Jp;
  current=0;
  for i=1:N+1
      current= current+J(i)*h;
  end
  I=current/d*1000*1e14;          total current dencity in [mA/cm^2]
end
%=========================================================================================%
```

8 Bibliography

[1] S. Arora, S. Swami and S. Bhan, Natural Resource Management for Climate Smart Sustainable Agriculture, New Delhi: Soil Conservation Society of India, 2017.

[2] J. Tsao, N. Lewis and G. Crabtree, "https://www.sandia.gov/~jytsao/Solar%20FAQs.pdf," 2006. [Online].

[3] J. A. Luceño-Sánchez, A. M. Díez-Pascual and R. P. Capilla, "Materials for Photovoltaics: State of Art and Recent Developments," *Int. J. Mol. Sci. 20,* pp. 976-1–976-42, 2019.

[4] Solar Power Europe, "Global market outlook for solar power 2018-2022," Solar Power Europe, 2018.

[5] Lazard's Levelized , "Lazard's Levelized Cost of Energy," 2017.

[6] Y. Cui, H. Yao, J. Zhang, K. Xian, T. Zhang, L. Hong, Y. Wang, Y. Xu, K. Ma, C. An, C. He, Z. Wei, F. Gao and J. Hou, "Single-Junction Organic Photovoltaic Cells with Approaching 18% Efficiency," *Adv. Mater.,* pp. 1908205-1–1908205-7, Feb. 2020.

[7] M. B. Salima, R. Nekoveib and . R. Jeyakumar, "Organic tandem solar cells with 18.6% efciency," *Solar Energy 198 ,* p. 160–166, 2020.

[8] Y. Zhang, I. D. W. Samuel , T. Wang and D. G. Lidzey, "Current Status of Outdoor Lifetime Testing of Organic Photovoltaics," *Adv. Sci.,* pp. 1800434-1–1800434-17, 2018.

[9] Z. Xiao, X. Jia and L. Ding, "Ternary organic solar cells offer 14% power conversion efficiency," *Sci. Bull.,* no. 62, pp. 1562-1564, Dec. 2017.

[10] L. Meng, Y. Zhang, X. Wan, C. Li, X. Zhang, Y. Wang, X. Ke, Z. Xiao, L. Ding, R. Xia, H.-L. Yip, Y. Cao and Y. Chen, "Organic and solution-processed tandem solar cells with 17.3% efficiency," *Science 361,* p. 1094–1098, Sep. 2018.

[11] J. Yuan, Y. Zhang, L. Zhou, G. Zhang, H.-L. Yip, T.-K. Lau, X. Lu, C. Zhu, H. Peng, P. A. Johnson, M. Leclerc, Y. Cao, J. Ulanski, Y. Li and Y. Zou, "Single-Junction Organic Solar Cell with over 15% Efficiency Using Fused-Ring Acceptor with Electron-Deficient Core," *Joule 3,* p. 1140–1151, Apr. 2019.

[12] Z. Yin, J. Wei and Q. Zheng, "Interfacial Materials for Organic Solar Cells Recent Advances and Perspectives," *Adv. Sci.,* vol. 3 , Feb. 2016.

[13] A. Köhler and H. Bässler, Electronic Processes in Organic Semiconductors: An Introduction, Weinheim, Germany: Wiley-VCH Verlag GmbH & Co. KGaA, Boschstr, 2015.

[14] A. Gusain, R. M. Faria and P. B. Miranda, "Polymer Solar Cells—Interfacial Processes Related to Performance Issues," *Front. Chem., 7,* pp. 1-25, Feb. 2019.

[15] O. J. Sandberg, M. Nyman and R. Österbacka, "Effect of contacts in organic bulk heterojunction solar cells," *Phys. Rev. Appl., 1,* pp. 024003-1–024003-15, Mar. 2014.

[16] V. D. Mihailetchi, P. W. M. Blom, J. C. Hummelen and M. T. Rispens, "Cathode dependence of the open-circuit voltage of polymer: fullerene bulk heterojunction solar cells.," *J. Appl. Phys.,* pp. 6849-6854, Nov. 2003.

[17] A. Petersen, T. Kirchartz and T. A. Wagner, "Charge extraction and photocurrent in organic bulk heterojunction solar cells," *Phys. Rev. B.,* pp. 045208-1–045208-11, Jan. 2012.

[18] O. J. Sandberg, S. Sandén, A. Sundqvist, J. H. Smått and R. Österbacka, "Determination of surface recombination velocities at contacts in organic semiconductor devices using injected carrier reservoirs," *Phys. Rev. Lett.,* pp. 076601-1–076601-5, Feb. 2017.

[19] M. Glatthaar, M. Riede, N. Keegan, K. Sylvester-Hvida, B. Zimmermann, M. Niggemann, A. Hinsch and A. Gombert, "Efficiency limiting factors of organic bulk heterojunction solar cells identified by electrical impedance spectroscopy," *Sol. Energy Mat. Sol. Cells.,* pp. 390-393, Dec. 2006.

[20] S. Schafer, A. Petersen, T. A. Wagner, R. Kniprath and D. Lingenfelser, "Influence of the indium tin oxide/organic interface on open-circuit voltage, recombination, and cell degradation in organic small-molecule solar cells," . *Phys. Rev. B.,* pp. 165311-1–165311-13, Apr. 2011.

[21] W. Tress, S. Corvers, K. Leo and M. Riede, "Investigation of driving forces for charge extraction in organic solar cells: Transient photocurrent measurements on solar cells showing S-shaped current–voltage characteristics," *Adv. Energy Mater.,* p. 873–880, July 2013.

[22] A. Wagenpfahl, C. Deibel and V. Dyakonov, "Organic solar cell efficiencies under the aspect of reduced surface recombination velocities," *IEEE J. Sel. Top Quant. Electron.,* p. 1759–1763, Dec. 2010.

[23] S. M. Sze and K. K. Ng, Physics of Semiconductor Devices, vol. Third Edition, New Jersey: A JOHN WILEY & SONS, JNC., PUBLICATION, 2007.

[24] S. S. Li, "Ch-10 Metal–Semiconductor Contacts," in *Semiconductor Physical Electronics,* 2006, p. 284—333.

[25] J. P. Gojanovi, "Organic Semiconductors in Optical Communications," in *27th Telecommunications forum TELFOR 2019*, Serbia, Belgrade, November 26-27, 2019.

[26] W. Brutting, Physics of Organic Semiconductors, Weinheim: Wiley-VCH Verlag, 2005.

[27] V. Coropceanu, J. Cornil, D. A. d. S. Filho, Y. Olivier, R. Silbey and J.-L. Bredas, "Charge transport in organic semiconductors," *Chem. Rev. 107,* p. 926–952, 2007.

[28] F. Laquai, D. Andrienko, R. Mauer and P. W. M. Blom, "Charge Carrier Transport and Photogeneration in P3HT:PCBM Photovoltaic Blends," *Macromo. Rapid Commun.,* p. 1001–1025, 2015.

[29] Q. Bao, "Doctoral thesis: Interface Phenomena in Organic Electronics," Linköping University, Linköping, 2015.

[30] J. Widmer, “Dissertation of PhD: Charge transport and energy levels in organic semiconductors,” Technische Universität, Dresden, 2013.

[31] A. J. Wagenpfahl, *Ph.D. Dissertation "Numerical simulations on limitations and optimization strategies of organic solar cells"*, Wurzburg , 2013.

[32] M. G. Helander, Z. B. Wang, J. Qiu and Z. H. Lub, “Band alignment at metal/organic and metal/oxide/organic interfaces,” *Appl. Phys. Lett.,* pp. 193310-1–193310-3, Nov 2008.

[33] W. Tress, Organic Solar Cells, Theory, Experiment, and Device Simulation, 2014.

[34] M. Knupfer and H. Peisert, “Electronic properties of interfaces between model organic semiconductors and metals,” *phys. stat. sol. (a), 201,* pp. 1055–1074,, 2004.

[35] E. F. SCHUBERT, LIGHT-EMITTING DIODES, vol. SECOND EDITION, Cambridge University Press, 2006.

[36] F. R. Pierret, Advanced Semiconductor Fundamentals, vol. Second Edition, Prentice Hall, 2002.

[37] M. S. Noor, “Trap-assisted recombination in semiconductors: application to group III gallium nitride material and junctions,” *Philosophical Magazine Part B,* Aug. 2006.

[38] M. M. Mandoc, F. B. Kooistra, J. C. Hummelen, B. de Boer and B. W. M. Blom, “Effect of traps on the performance of bulk heterojunction organic solar cells,” *Appl. Phys. Lett.,* Nov. 2007.

[39] A. Wagenpfahl, D. Rauh, M. Binder, C. Deibel and V. Dyakonov, “S-shaped current-voltage characteristics of organic solar devices,” *Phys. Rev. B, 82,* pp. 115306-1–115306-8, Sep. 2010.

[40] A. E. Becquerel, “The electrical effects produced under the influence of solar rays,” 1839.

[41] W. G. Adams, F. R. S. and M. R. DAY, “The action of light on Selenium,” 1876.

[42] D. M. Chapin, C. S. Fuller and G. L. Pearson, “A New Silicon p-n Junction Photocell for Converting Solar Radiation into Electrical Power,” American Institute of Physics, New Jersey, 1954.

[43] K. Yoshikawa, W. Yoshida, T. Irie, H. Kawasaki, K. Konishi, H. Ishibashi, T. Asatani, D. Adachi, M. Kanematsu, H. Uzu and K. Yamamoto, “Exceeding conversion efficiency of 26% by heterojunction interdigitated back contact solar cell with thin film Si technology,” *SOL ENERG MAT SOL C.,* p. 1–6, June 2017.

[44] A. Pochettino, “The photoconductivity of anthracene,” Acad. Lincei Rend., 1906.

[45] M. Volmer, “photoconductivity in organics,” in *Ann. Physik, 40,* 1913.

[46] X.-F. Wang and O. Kitao, “Natural Chlorophyll-Related Porphyrins and Chlorins for Dye-Sensitized Solar Cells,” *Molecules,* p. 4484–4497, 2012.

[47] N. S. Sariciftci, L. Smilowitz, A. J. Heeger and F. Wudi, “Photoinduced Electron Transfer from a Conducting Polymer to Buckminsterfullerene,” *SCIENCE,* p. 1474–1476, Nov. 1992.

[48] N. S. Sariciftci, D. Braun, C. and Zhang, V. I. Srdanov, A. J. Heeger, G. Stucky and F. Wudl, "Semiconducting polymer-buckminsterfullerene heterojunctions: Diodes, photodiodes, and photovoltaic cells," *Appt. Phys. Lett.*, p. 585–587, December 1992.

[49] A. K. Ghosh and T. Feng, "Rectification, space-charge-limited current, photovoltaic and photoconductive properties of AI/tetracene/Au sandwich cell," *J. Appl. Phys.*, p. 2781–2788, June 1973.

[50] C. W. Tang, "MULTILAYER ORGANIC PHOTOVOLTAC". USA Patent 4,164,431, 1979.

[51] G. Yu, J. Gao, J. C. Hummelen, F. Wudi and A. J. Heeger, "Polymer Photovoltaic Cells: Enhanced Efficiencies via a Network of Internal Donor-Acceptor Heterojunctions," *SCIENCE*, p. 1789–1791, Dec. 1995.

[52] M. Mirsafaei, A. Fallahpour, P. Lugli, H.-G. Rubahn, J. Adam and M. Madsen, "The influence of electrical effects on device performance of organic solar cells with nano-structured electrodes," 13 July 2017. [Online]. Available: www.nature.com/scientificreports. [Accessed 31 Oct. 2016].

[53] G. A. CHAMBERLAIN, "ORGANIC SOLAR CELLS: A REVIEW," *Solar Cells*, p. 47–83, 1983.

[54] T. A. Abdalla, W. Mammo and B. Workalemahu, "Electronic and photovoltaic properties of a single layer poly[3-(2",5"-diheptyloxyphenyl)-2,2'-bithiophene] devices," *Elsevier, Synthetic Metals*, p. 213–219, May 2004.

[55] C. W. Tang, "Two-layer organic photovoltaic cell," *Appl. Phys. Lett.*, p. 183–185, Jan 1986.

[56] J. J. M. Halls, C. A. Walsh, N. G. Greenham, E. A. Marseglia, R. H. Friend, S. C. Moratti and A. B. Holmes, "Efficient photodiodes from iterpenetrating polymer networks," *Nature*, p. 498–500, Aug. 1995.

[57] J.-M. Nunzi, "Organic photovoltaic materials and devices," *C. R. Physique*, p. 523–542, 2002.

[58] G. Li, L. Liu, F. Wei, S. Xia and X. Qian, "Recent Progress in Modeling, Simulation, and Optimization of Polymer Solar Cells," *IEEE J PHOTOVOLT Journal*, p. 320–340, 2012.

[59] B. Qi and J. Wang, "Open-circuit voltage in organic solar cells," *Journal of Materials Chemistry*, Sep. 2012.

[60] W. J. POTSCAVAGE, JR., A. SHARMA and BERNA, "Critical Interfaces in Organic Solar Cells and Their Influence on the Open-Circuit Voltage," *ACCOUNTS OF CHEMICAL RESEARCH*, p. 1758–1767, Nov. 2009.

[61] N. K. Elumalai and A. Uddin, "Open circuit voltage of organic solar cells: an in-depth review," *Energy Environ. Sci.*, p. 391–410, 2016.

[62] P. W. M. Blom, V. D. Mihailetchi, L. J. A. Koster and D. E. Markov, "Device Physics of Polymer:Fullerene Bulk Heterojunction Solar Cells," *Adv. Mater.*, p. 1551–1566, 2007.

[63] M. S. Cengiz and M. S. Mamis, "Price-Efficiency Relationship for Photovoltaic Systems on a Global Basis," *International Journal of Photoenergy*, 2015.

[64] International Renewable Energy Agency, “RENEWABLE ENERGY TECHNOLOGIES: COST ANALYSIS SERIES: Solar Photovoltaics,” 2012.

[65] P. Peumans and S. R. Forrest, “Very-high-efficiency double-heterostructure copper phthalocyanine/C60 photovoltaic cells,” *Appl. Phys. Lett.,* p. 126–128, July 2001.

[66] S. E. Shaheen, C. J. Brabec, N. S. Sariciftci, F. Padinger, T. Fromherz and J. C. Hummelen, “2.5% efficient organic plastic solar cells,” *Appl. Phys. Lett.,* p. 841–843, Feb. 2001.

[67] G. Li, V. Shrotriya, J. Huang, Y. Yao, T. Moriarty, K. Emery and Y. Yang, “High-efficiency solution processable polymer photovoltaic cells by self-organization of polymer blends,” *nature materials,* p. 864–868, Nov. 2005.

[68] W. Ma, C. Yang, X. Gong, K. Lee and A. J. Heeger, “Thermally Stable, Effeicent Polymer Solar Cell with Nanoscale Control of the Interpenetrating Network Morphology,” *Adv. Funct. Mater.,* p. 1617–1622, 2005.

[69] H. Yu, Y. Li, Y. Dong and X. Huang, “Fabrication and Optimization of Polymer Solar Cells Based on P3HT:PCBM System,” *International Journal of Photoenergy,* Sep. 2016.

[70] Y. Liang, Y. Wu, D. Feng, S.-T. Tsai, H.-J. Son, G. Li and L. Yu, “Development of New Semiconducting Polymers for High Performance Solar cells,” *J. AM. CHEM. SOC.,* p. 56–57, 2009.

[71] Y. Liang, D. Feng, Y. Wu, S.-T. Tsai, G. Li, C. Ray and L. Yu, “Highly Efficient Solar Cell Polymers Developed via Fine-Tuning of Structural and Electronic Properties,” *J. AM. CHEM. SOC.,* p. 7792–7799, 2009.

[72] Y. Liang, Z. Xu, J. Xia, S.-T. Tsai, Y. Wu, G. Li, C. Ray and L. Yu, “For the Bright Future—Bulk Heterojunction Polymer Solar Cells with Power Conversion Efficiency of 7.4%,” *Adv. Mater.,* p. E135–E138, 2010.

[73] G. Zhao, Y. He and Y. Li, “6.5% Efficiency of Polymer Solar Cells Based on poly(3-hexylthiophene) and Indene-C60 Bisadduct by Device Optimization,” *Adv. Mater.,* p. 4355–4358, 2010.

[74] S.-H. Liao, H.-J. Jhuo, Y.-S. Cheng and S.-A. Chen, “Fullerene Derivative-Doped Zinc Oxide Nanofilm as the Cathode of Inverted Polymer Solar Cells with Low-Bandgap Polymer (PTB7-Th) for High Performance,” *Adv. Mater.,* p. 4766–4771, 2013.

[75] S.-H. Liao, H.-J. Lhuo, P.-N. Yeh, Y.-S. Cheng, Y.-L. Li, Y.-H. Lee and S. Sharma, “Single Junction Inverted Polymer Solar Cell Reaching Power Conversion Efficiency 10.31% by Employing Dual-Doped Zinc Oxide Nano-Film as Cathode Interlayer,” 2014.

[76] J. Zhao, Y. Li, G. Yang, K. Jiang, H. Lin, H. Ade, W. Ma and H. Yan, “Efficient organic solar cells processed from hydrocarbon solvents,” *NATURE ENERGY,* p. 1–7, Feb. 2016.

[77] Y. Lin, J. Wang, Z.-G. Zhang, H. Bai, Y. Li, D. Zhu and X. Zhan, “An Electron Acceptor Challenging Fullerenes for Efficient Polymer Solar Cells,” *Adv. Mater.,* p. 1170–1174, 2015.

[78] Y. Lin, F. Zhao, Q. He, L. Huo, Y. Wu, T. C. Parker, W. Ma, Y. Sun, C. Wang, D. Zhu, A. J. Heeger, S. R. Marder and X. Zhan, "A High-Performance Electron Acceptor with Thienyl Side Chains for Organic Photovoltaics," *J. Am. Chem. Soc.*, March 2016.

[79] W. Zhao, D. Qian, S. Zhang, S. Li, O. Inganäs, F. Gao and J. Hou, "Fullerene-Free Polymer Solar Cells with over 11% Efficiency and Excellent Thermal Stability," *Adv. Mater.*, p. 4734–4739, 2016.

[80] W. Zhao, S. Li, H. Yao, S. Zhang, Y. Zhang, B. Yang and J. Hou, "Molecular Optimization Enables over 13% Efficiency in Organic Solar Cells," *J. Am. Chem. Soc.*, p. 7148−7151, May 2017.

[81] S. Zhang, Y. Qin, J. Zhu and J. Hou, "Over 14% Efficiency in Polymer Solar Cells Enabled by a Chlorinated Polymer Donor," *Adv. Mater. 2018,*, pp. 1800868-1–1800868-7, 2018.

[82] Z. Fei, F. D. Eisner, X. Jiao, M. Azzouzi, J. A. Röhr, Y. Han, M. Shahid, A. S. R. Chesman, C. D. Easton, C. R. McNeill, T. D. Anthopoulos, J. Nelson and M. Heeney, "An Alkylated Indacenodithieno[3,2-b]thiophene-Based Nonfullerene Acceptor with High Crystallinity Exhibiting Single Junction Solar Cell Efficiencies Greater than 13% with Low Voltage Losses," *Adv. Mater.*, pp. 1705209-1–1705209-7, 2018.

[83] Z. Zheng, Q. Hu, S. Zhang, D. Zhang, J. Wang, S. Xie, R. Wang, Y. Qin, W. Li, L. Hong, N. Liang, F. Liu, Y. Zhang, Z. Wei, Z. Tang, T. P. Russell, J. Hou and H. Zhou, "A Highly Efficient Non-Fullerene Organic Solar Cell with a Fill Factor over 0.80 Enabled by a Fine-Tuned Hole-Transporting Layer," *Adv. Mater.*, pp. 1801801-1–1801801-9, 2018.

[84] G. Liu, J. Jia, K. Zhang, X. Jia, Q. Yin, W. Zhong, L. Li, F. Huang and Y. Cao, "15% Efficiency Tandem Organic Solar Cell Based on a Novel Highly Efficient Wide-Bandgap Nonfullerene Acceptor with Low Energy Loss," *Adv. Energy Mater.*, pp. 1803657-1–1803657-9, 2019.

[85] Y. Cui, H. Yao, L. Hong, T. Zhang, Y. Tang, B. Lin, K. Xian, B. Gao, C. An, P. Bi, W. Ma and J. Hou, "17% efficiency organic photovoltaic cell with superior processability," *MATERIALS SCIENCE,* 2019.

[86] Y. Y. Cui, H. Yao, J. Zhang, T. Zhang, Y. Wang, L. Hong, K. Xian, B. Xu, S. Zhang, J. Peng, Z. Wei, F. Gao and J. Hou, "Over 16% efficiency organic photovoltaic cells enabled by a chlorinated acceptor with increased open-circuit voltages," *NATURE COMMUNICATIONS*, 2019.

[87] C. Jacoboni, Theory of Electron Transport in Semiconductors, Berlin: Springer-Verlag Berlin Heidelberg, 2010.

[88] L. J. A. Koster, E. C. E. Smits, V. D. Mihailetchi and P. W. M. Blom, "Device model for the operation of polymer/fullerene bulk heterojunction solar cells," *Phys. Rev. B,* pp. 085205-1–085205-9, 2005.

[89] M. Shofiqul Islam, "Analytical modeling of organic solar cells including monomolecular recombination and carrier generation calculated by optical transfer matrix method," *Organic Electronics,* p. 1–14, 2016.

[90] Ž. Jelić, J. Petrović, P. Matavulj, J. Melancon, A. Sharma, C. Zellhofer and S. Živanović, "Modeling of the polymer solar cell with P3HT:PCBM active layer," *Physica Scripta, T162,* Sep. 2014.

[91] L. A. A. Pettersson, L. S. Roman and O. Inganäs, “Modeling photocurrent action spectra of photovoltaic devices based on organic thin films,” *J. Appl. Phys.*, p. 487–496, July 1999.

[92] C. L. Braun, “Electric field assisted dissociation of charge transfer states as a mechanism of photocarrier production,” *J. Chem. Phys.*, p. 4157–4161, May 1984.

[93] M. Giuliani, E. R. Waclawik, J. M. Bell and N. Motta, “Temperature and electric field dependent mobility in poly(3-hexylthiophene) diodes,” *J. Appl. Phys*, Aug. 2010.

[94] I. A. Howard, R. Mauer, M. Meister and F. Laquai, “Effect of Morphology on Ultrafast Free Carrier Generation in Polythiophene: Fullerene Organic Solar Cells,” *J. AM. CHEM. SOC.*, p. 14866–14876, 2010.

[95] G. Juška, K. Genevičius, N. Nekrašas, G. Sliaužys and R. Österbacka, “Two dimensional Langevin recombination in regioregular poly(3-hexylthiophene),” *Appl. Phys. Lett. 95,* pp. 013303-1–013303-3, July 2009.

[96] E. Knapp, R. Häusermann, H. U. Schwarzenbach and B. Ruhstaller, “Numerical simulation of charge transport in disordered organic semiconductor devices,” *J. Appl. Phys. 108,* pp. 054504-1–054504-8, Sep. 2010.

[97] S. O. Kasap, B. Fogal, M. Z. Kabir, R. E. Johanson and S. K. O’Leary, “Recombination of drifting holes with trapped electrons in stabilized a-Se photoconductors: Langevin recombination,” *Appl. Phys. Lett. 105,* p. 1991–1993, March 2014.

[98] S. Siegfried, Analysis and Simulation of Semiconductor Devices, New York: Springer-Verlag Wien, 1984.

[99] J. Kiusalaas, Numerical Methods in Engineering with Matlab, Cambridge: cambridge university press, 2005.

[100] D. L. SCHARFETTER and H. K. GUMMEL, “Large-Signal Analysis of a Silicon Read Diode Oscillator,” *IEEE Transactions on Electron Devices,* p. 64–77, Jun. 1969.

[101] Ž. Jelic, *MSc thesis, "MODELOVANJE SOLARNE ĆELIJE SA AKTIVNIM SLOJEM NA BAZI KONJUGOVANOG POLIMERA",* Belgrade, 2013.

[102] M. Glatthaar, M. Riede, N. Keegan, K. Sylvester-Hvid, B. Zimmermann, M. Niggemann, A. Hinsch and A. Gombert, “Efficiency limiting factors of organic bulk heterojunction solar cells identified by electrical impedance spectroscopy,” *Sol. Energ. Mat. Sol. C., 91,* p. 390–393, 2007.

[103] A. Geiser, B. Fan, H. Benmansour, F. Castro, J. Heier, B. Keller, k. E. Mayerhofer, F. Nuesch and R. Hany, “Poly(3-hexylthiophene)/C60 heterojunction solar cells: Implication of morphology on performance and ambipolar charge collection,” *Sol. Energ. Mat. Sol. C. 92,* p. 464–473, 2008.

[104] D. Gupta, M. Bag and K. S. Narayan, “Correlating reduced fill factor in polymer solar cells to contact effects,” *Appl. Phys. Lett. 92,* pp. 093301-1–093301-3, March 2008.

[105] D. D. Gupta, S. Mukhopadhyay and K. S. Narayan, “Fill factor in organic solar cells,” *Sol. Energ. Mat. Sol. C. 94,* p. 1309–1313, July 2010.

[106] C. Uhrich, D. Wynands, S. Olthof, M. K. Riede, K. Leo, S. Sonntag, B. Maennig and M. Pfeiffer, "Origin of open-circuit voltage in planar and bulk heterojunction organic thin-film photovoltaics depending on doped transport layers," *J. Appl. Phys. 104,* pp. 043107-1–043107-6, Aug. 2008.

[107] A. Kumar, S. Sista and Y. Yang, "Dipole induced anomalous S-shape I - V curves in polymer solar cells," *J. Appl. Phys. 105,* pp. 094512-1–094512-6, May 2009.

[108] H. Jin, M. Tuomikoski, J. Hiltunen, P. Kopola, A. Maaninen and F. Pino, "Polymer-Electrode Interfacial Effect on Photovoltaic Performances in Poly(3-hexylthiophene):Phenyl-C61-butyric Acid Methyl Ester Based Solar Cells," *J. Phys. Chem. C., 113,* p. 16807–16810, Aug. 2009.

[109] B. T. de Villers, C. J. Tassone, S. H. Tolbert and B. J. Schwartz, "Improving the Reproducibility of P3HT:PCBM Solar Cells by Controlling the PCBM/Cathode Interface," *J. Phys. Chem. C., 113,* p. 18978–18982, Sep. 2009.

[110] M. R. Lilliedal, A. J. Medford, M. V. Madsen, K. Norrman and F. Krebs, "The effect of post-processing treatments on inflection points in current-voltage curves of roll-to-roll processed polymer photovoltaics," *Sol. Energ. Mat. Sol. C. 94,* p. 2018–2031, 2010.

[111] W. Tress, A. Petrich, M. Hummert, M. Hein, K. Leo and M. Riede, "Imbalanced mobilities causing S-shaped IV curves in planar heterojunction organic solar cells," *Appl. Phys. Lett. 98,* pp. 063301-1–063301-3, Feb. 2011.

[112] J. C. Wang, X. C. Ren, S. Q. Shi, C. W. Leung and P. K. L. Chan, "Charge accumulation induced S-shape J–V curves in bilayer heterojunction organic solar cells," *Organic Electronics, 12,* p. 880–885, March 2011.

[113] W. Tress, K. Leo and M. Riede, "Influence of Hole-Transport Layers and Donor Materials on Open-Circuit Voltage and Shape of I– V Curves of Organic Solar Cells," *Adv. Funct. Mater., 21,* p. 2140–2149, 2011.

[114] W. Tress and O. Inganäs, "Simple experimental test to distinguish extraction and injection barriers at the electrodes of (organic) solar cells with S-shaped current-voltage characteristics," *Sol. Energy Mater Sol. C., 117,* p. 599–603, 2013.

[115] B. Y. Finck and B. J. Schwartz, "Understanding the origin of the S-curve in conjugated polymer/fullerene photovoltaics from drift-diffusion simulations," *Appl. Phys. Lett., 103,* pp. 053306-1–053306-4, Aug. 2013.

[116] R. Saive, C. Mueller, J. Schinke, R. Lovrincic and W. Kowalsky, "Understanding S-shaped current-voltage characteristics of organic solar cells: Direct measurement of potential distributions by scanning Kelvin probe," *Appl. Phys. Lett., 103,* pp. 243303-1–243303-3, Dec. 2013.

[117] L. Sims, U. Hörmann, R. Hanfland, R. C. I. MacKenzie, F. R. Kogler, R. Steim, W. Brütting and P. Schilinsky, "Investigation of the s-shape caused by the hole selective layer in bulk heterojunction solar cells," *Organic Electronics 15,* p. 2862–2867, Aug. 2014.

[118] J. A. Love, S.-H. Chou, Y. Huang, G. C. Bazan and T.-Q. Nguyen, "Effects of solvent additive on "s-shaped" curves in solution-processed small molecule solar cells," *Beilstein J. Org. Chem., 12,* p. 2543–2555, Nov. 2016.

[119] A. Pockett, H. K. H. Lee, B. L. Coles, W. C. Tsoi and M. J. Carnie, "A combined transient photovoltage and impedance spectroscopy approach for a comprehensive study of interlayer degradation in non-fullerene acceptor organic solar cells," *Nanoscale, 11,* p. 10872–10883, 2019.

[120] E. Sesa, D. Darwis, X. Zhou, W. J. Belcher and P. C. Dastoor, "Experimental determination of the relationship between the elements of a back-to-back diode model for organic photovoltaic cells' S-shaped I-V characteristics and cell structure," *AIP Advances 9,* pp. 025014-1–025014-8, Feb. 2019.

[121] A. Petrović, J. Gojanović, P. Matavulj, M. Islam and S. Živanović, "Temperature dependence of P3HT:ICBA polymer solar cells," in *17th International Conference on Numerical Simulation of Optoelectronic Devices (NUSOD)*, Copenhagen, Denmark, 2017.

[122] J. Bisquert and G.-B. Germà , "On Voltage, Photovoltage, and Photocurrent in Bulk Heterojunction Organic Solar Cells," *J. Phys. Chem. Lett.2,* p. 1950–1964, July 2011.

[123] N. I. Craciun, "Electrical characterization polymeric charge transport layers," in *Universal Arrhenius temperature activated charge transport in diodes from disordered organic semiconductors.*, University of Groningen, 2011, pp. Sec. 4.2, Ch. 4, 47-54.

[124] C. Liu, Z. Li, Z. Zhang, X. Zhang, L. Shen, W. Guo, L. Y. Long and S. Ruan, "Improving charge carrier transport of organic solar by incorporating deep energy level molecule," *Phys. Chem. Chem. Phys.*, 2013.

[125] T. Ameri, T. Heumüller, J. Min, N. Li, G. Matt, U. Scherf and C. J. Brabec, "IR sensitization of indene C60 bisadduct (ICBA) in the ternary organic solar cells," *Energy Environ. Sci. 6,* pp. 1796-1–1796-20, 2010.

[126] K. Li, Y. Shen, N. Majumdar, C. Hu, M. C. Gupta and J. C. Campbell, "Determination of free polaron lifetime in organic bulk heterojunction solar cells by transient time analysis," *J. Appl. Phys. 108,* pp. 084511-1–084511-5, 2010.

[127] A. Khalf, J. Gojanović, N. Ćirović, S. Živanovic and P. Matavulj, "The Impact of Surface Processes on the J–V Characteristics of Organic Solar Cells," *IEEE J. PHOTOVOLT., 10,* p. 514–521, 27 Jan. 2020.

[128] A. Khalf, J. Gojanović, N. Ćirović, M. Islam, S. Živanović and P. Matavulj , "Analysis of the Surface Recombination Influence on Organic Solar Cell J-V curve," in *OSA Advanced Photonics Congress (AP) 2019 (IPR, Networks, NOMA, SPPCom, PVLED)*, Burlingame, California, United States, 2019.

[129] A. Khalf, J. Gojanović, N. Ćirović and S. Živanović, "Two diferent types of S-shaped J-V characteristics in organic solar cells," *Optical and Quantum Electronics,* pp. 121-1–121-10, 10 Feb. 2020.

[130] E. L. Ratcliff, B. Zacher and N. R. Armstrong, "Selective Interlayers and Contacts in Organic Photovoltaic Cells," *J. Phys. Chem. Lett., 2,* p. 1337–1350, 2011.

[131] P. Wudfel and U. Wurfel, “Basic structure of solar cells, ch. 6, sec.6.8,” in *Physics of solar cells; from basic principles to advanced concepts*, Wiley-VCH, 2016, pp. 154-159.

[132] E. J. Juarez-Perez, M. Wuβler, F. Fabregat-Santiago, K. Lakus-Wollny, E. Mankel , T. Mayer , W. Jaegermann and I. Mora-Sero, “The role of the selective contacts in the performance of lead halide perovskite solar cells,” *J Phys Chem Lett., 5,* p. 680–685, Jan. 2014.

[133] J. Reinhardt, M. Grein, C. Bühler, M. Schubert and U. Würfel, “Identifying the impact of surface recombination at electrodes in organic solar cells by means of electroluminescence and modeling,” *Adv. Energy Mater., 4,* pp. 1400081-1–1400081-9, Feb . 2014.

[134] A. Sundqvist, O. J. Sandberg, M. Nyman, S. Jan-Henrik and R. Österbacka, “Origin of the S-shaped JV curve and the light-soaking issue in inverted organic solar cells,” *Adv. Funct. Mater. 6,* pp. 1502265-1–1502265-7, 2016.

[135] V. Coropceanu, J. Corni, D. A. d. S. Filho, Y. Olivier, R. Silbey and J.-L. Bre´das, “Charge Transport in Organic Semiconductors,” *Chem. Rev. 107,* p. 926−952, 2007.

Biography

Ali Ramadan Ahmed Khalf was born on March 26, 1966, in Tripoli–Libya. He finished elementary and high school in 1984 in Tripoli. And in 1985, he enrolled the Faculty of Science at the University of Tripoli in Libya, where he received a Bachelor's degree in physics in 1990. Then he enrolled the Master studies in 1995, in the department of optoelectronics at the School of Electrical Engineering, University of Belgrade, he graduated with an overall average score of 8.4, where he defended his Master's thesis on October 15, 1997, entitled "Design and development of optical gathering system" under the mentorship of Prof. Dr. Miodrag V. Popović. Later Mr. Khalf enrolled in doctoral studies at the Department of Microelectronics and Technical Physics School of Electrical Engineering, Belgrade University, in 2014-2015, he passed all the required exams with a grade point average of 9.5.

He worked at "Research and Development center" (R&D center) in Tripoli–Libya as an engineer from 1991 to 1995, then in the period from 1997 to 2011 at the same R&D center as a research assistant for the development of an optical system controlling the beam divergence of diode laser as a unit of free space laser communication link system. Also, he was teaching as a part-time assistant lecturer at the University of Tripoli and at the high institute of computer science in Tripoli–Libya from 2007 to 2011. Since 2011–present he has been a lecturer in the physics department, University of Tripoli, Libya.

List of publications

- A. Khalf, J. Gojanović, N. Ćirović and S. Živanović, "Two different types of S-Shaped J-V characteristics in organic solar cells", The Seventh International School and Conference on Photonics, 26–30 August 2019, Belgrade, Serbia, PHOTONICA2019, p 143, ISBN 978-86-7306-153-5.
- A. Khalf, J. Gojanović, N. Ćirović, M. Islam, S. Živanović, and. P. Matavulj, "Analysis of the Surface Recombination Influence on Organic Solar Cell J-V curve", paper JT4A. 26, Advanced Photonics Congress (IPR, Networks, NOMA, PVLED, SPPCom), OSA, 29 July–1 August 2019, ISBN: 978-1-943580-64-4.
- A. Khalf, J. Gojanović, N. Ćirović, S. Živanovic and P. Matavulj, "The Impact of Surface Processes on the J-V Characteristics of Organic Solar Cells," IEEE J. PHOTOVOLT., 10, no. 2, p. 514–521, March 2020, DOI: 10.1109/JPHOTOV.2020.2965401.
- A. Khalf, J. Gojanović, N. Ćirović and S. Živanović, "Two diferent types of S-shaped J-V characteristics in organic solar cells," Optical and Quantum Electronics, pp. 121-1–121-10, 10 Feb. 2020, DOI: 10.1007/s11082-020-2236-7.

Изјава о ауторству

Име и презиме аутора Али Калф (Ali Ramadan Ahmed Khalf)

Број индекса 2014/5053

Изјављујем

да је докторска дисертација под насловом

Утицај површинских процеса на струјно-напонску карактеристику органских соларних ћелија

- резултат сопственог истраживачког рада;
- да дисертација у целини ни у деловима није била предложена за стицање друге дипломе према студијским програмима других високошколских установа;
- да су резултати коректно наведени и
- да нисам кршио/ла ауторска права и користио/ла интелектуалну својину других лица.

Потпис аутора

У Београду, 02.02.2021

Изјава о истоветности штампане и електронске верзије докторског рада

Име и презиме аутора Али Калф (Ali Ramadan Ahmed Khalf)

Број индекса 2014/5053

Студијски програм Докторске академске студије

Наслов рада Утицај површинских процеса на струјно-напонску карактеристику органских соларних ћелија

Ментор др Јована Гојановић

Предложени ментор:

др Јована Гојановић, доцент

Изјављујем да је штампана верзија мог докторског рада истоветна електронској верзији коју сам предао/ла ради похрањивања у **Дигиталном репозиторијуму Универзитета у Београду.**

Дозвољавам да се објаве моји лични подаци везани за добијање академског назива доктора наука, као што су име и презиме, година и место рођења и датум одбране рада.

Ови лични подаци могу се објавити на мрежним страницама дигиталне библиотеке, у електронском каталогу и у публикацијама Универзитета у Београду.

Потпис аутора

У Београду, 02.02.2021

Изјава о коришћењу

Овлашћујем Универзитетску библиотеку „Светозар Марковић“ да у Дигитални репозиторијум Универзитета у Београду унесе моју докторску дисертацију под насловом:

“Утицај површинских процеса на струјно-напонску карактеристику органских соларних ћелија”

која је моје ауторско дело.

Дисертацију са свим прилозима предао/ла сам у електронском формату погодном за трајно архивирање.

Моју докторску дисертацију похрањену у Дигиталном репозиторијуму Универзитета у Београду и доступну у отвореном приступу могу да користе сви који поштују одредбе садржане у одабраном типу лиценце Креативне заједнице (Creative Commons) за коју сам се одлучио/ла.

1. Ауторство (CC BY)
2. Ауторство – некомерцијално (CC BY-NC)
3. Ауторство – некомерцијално – без прерада (CC BY-NC-ND)
4. Ауторство – некомерцијално – делити под истим условима (CC BY-NC-SA)
5. Ауторство – без прерада (CC BY-ND)
6. Ауторство – делити под истим условима (CC BY-SA)

(Молимо да заокружите само једну од шест понуђених лиценци.
Кратак опис лиценци је саставни део ове изјаве).

Потпис аутора

У Београду, 02.02.2021